

LOW TEMPERATURE EPITAXY OF SILICON BY ELECTRON-BEAM EVAPORATION FOR POLYCRYSTALLINE SILICON THIN FILM SOLAR CELLS

vorgelegt von
Master of Science
Pınar Doğan
aus İzmir

Von der Fakultät IV- Elektrotechnik und Informatik
der Technischen Universität Berlin
zur Erlangung des akademischen Grades
Doktor der Naturwissenschaften
Dr. rer. nat.
genehmigte Dissertation

Promotionsausschuss:

Vorsitzender: Herr. Prof. Dr. Stephan Völker
Berichter: Herr. Prof. Dr. Bernd Rech
Berichter: Herr. Prof. Dr. Jörg Müller (TU Hamburg-Harburg)
Berichter: Herr. Prof. Dr. Norbert Nickel

Tag der wissenschaftlichen Aussprache: 07.12.2011

Berlin 2011
D83

ACKNOWLEDGEMENTS

I would like to take this opportunity to thank to my advisors, colleagues and friends who played a role in my life during the preparation of this thesis.

Prof. Bernd Rech for supervising my thesis, for his ideas about the experiments and for his full support to finish my thesis successfully.

Prof. Jörg Müller for showing interest in this work and for agreeing to be the second Professor for the thesis defense jury.

Prof. Norbert Nickel for sharing his expertise about Raman measurements, for agreeing to be in the thesis defense jury and for the final proof reading of the thesis.

Dr. Stefan Gall for giving me the opportunity to work in this project, for his great support, for his guidance during my PhD thesis, for proof reading my thesis, and for celebrating new solar cell records.

Dr. Frank Fenske for leading the project with Von Ardenne Anlagentechnik GmbH and giving me the opportunity to work in this project, for helping me with the electron-beam evaporation tool, for scientific discussions and for proof reading my thesis.

Prof. Dr. Mehmet Günes, my master of science thesis advisor, for introducing me to the topic solar energy and for supporting me during my academic career.

Von Ardenne Anlagentechnik GmbH for the joint project with HZB concerning the investigation of deposition parameters of e-beam evaporation. These experiments constitute the most important parts of my thesis. Therefore, I greatly acknowledge the support and scientific interest of Von Ardenne Anlagentechnik GmbH.

Dr. Ute Schubert / Dr. Jens Schneider (CSG Solar) for the joint experiments about solid phase crystallized poly-Si films prepared by e-beam evaporation. This was actually a breakthrough for my thesis as well as for the Si-Photovoltaics department.

Dr. Ivan Gordon /Dries Van Gestel (IMEC) for the joint experiments concerning the influence of intra-grain defects in poly-Si thin-films. Special thanks goes to Ivan who assisted me during my stay at IMEC (Athlet mobility program) and gave me ideas how to simplify our photolithography process.

Guobin Jia (University of Cottbus) for the EBIC measurement he performed on our wafer-based and glass-based solar cells.

Thomas Lußky for helping us with the maintenance of the e-beam evaporation tool.

Erhard Conrad for the deposition of many amorphous Si emitter layers.

Stefan Common for everything. I called him my dad in Germany not only because he has his birthday on the same day as my father but also for his help in many ways. First of all for his help with the e-beam evaporation tool, for sharing the office with him and benefiting from coffee breaks and for his help with the German translations.

Kerstin Jacob / Anja Scheu for their assistance in the clean room and being always ready to help with the chemicals. Of course many thanks for the preparation of many solar cells. Special thanks to Kerstin for playing the radio in the clean room which sometimes played even Turkish songs which made me feel at home.

Dr. Björn Rau / Dr. Christiane Becker and Dr. Florian Ruske, the Post-docs of Si thin-film group, for always being ready for discussions and for their sweet friendships.

Benjamin Gorka for the hydrogen passivation experiments and for introducing me to the e-beam evaporation tool. He is the warmest German guy that I have ever met and I have enjoyed a lot to join his invitations to the football plays at the weekends and of course to Latin dancing.

Martin Muske for the perfect seed layers ☺, for scientific discussions of the results, for his friendship, for sharing the beautiful pictures that he took during his holidays which I have used for decorating my computers desktop.

Kyuyoul Lee also for the perfect seed layers, and for the delicious Korean tee.

Tobias Hänel for the EQE measurements he performed, for his friendly behaviour and for trying to use some Turkish words he learned.

Lars P. Scheller for his guidance and help with the Hall-effect measurements.

Dr. Moshe Weizman for the scientific discussions, for sharing the office, for the tasty fruit breaks, for his positive-energy and for taking me to Yoga with him.

Carola Klimm for many SEM and EBSD images.

Marion Krusche for everything. She is my mother in Germany. I am very grateful for her great support which made me go through the difficult periods during my thesis.

Asli Ugur Katmis / Ferhat Katmis, my friends, with whom I have shared many Turkish nights in Berlin. Thanks for the beautiful time we have spend together.

Family Karhan for their help and support, and for funny celebrations.

My Parents: Family Özdag and Family Dogan for their love and telephone supports. Special thanks goes to my grandparents who grow me up and gave me their full love.

Melih Dogan, my husband, for his love and for his full support in every part of my life. Thanks for bringing the joy and happiness in my life.

ABSTRACT

The structural and electrical properties of Si thin-films epitaxially grown by electron-beam evaporation on Si wafers with different crystallographic orientations and on poly-Si seed layer coated glass substrates were investigated. In particular, the influence of deposition parameters like substrate temperature, deposition rate, base pressure and substrate bias on the properties of Si films and solar cells were studied. In addition, the influence of the underlying crystallographic orientation was checked. (100) epitaxial layers revealed a lower defect density and a higher solar cell efficiency compared to (111) epitaxial layers. The substrate temperature was investigated in the range of $T_s = 450-700$ °C for wafer-based structures. It was found that $T_s \geq 600$ °C is necessary for a lower extended defect density and a higher solar cell efficiency. Base pressure investigations revealed that a base pressure of up to 1×10^{-6} mbar does not influence the solar cell efficiency when a deposition rate of about 100-140 nm/min was used.

Poly-Si thin-films on glass were studied in detail. It was found that crystalline quality of the epitaxially grown poly-Si films strongly depends on the crystallographic orientation of the underlying grains. Grains near-(100) orientation revealed considerably less number of defects compared to non-(100) orientations. In addition, the intra-grain defects were caused by the defects present in the AIC seed layers and / or at the epitaxially growing film / seed layer interface. Hydrogen-passivation experiments showed that solar cell efficiency improves after passivation of the grain boundary defects. So far the best solar cell efficiency for poly-Si thin-film solar cells on glass was obtained by solid phase crystallization of amorphous Si deposited by e-beam evaporation.

Wafer-based solar cell results revealed that e-beam evaporation is a favourable method to prepare high quality Si films under non-UHV environment and with high deposition rates. However for glass-based structures, defects caused by the imperfections of the seed layer and out-diffusion of impurities from glass substrate inside the growing films remain as some of the important issues to be solved in order to obtain high efficiency poly-Si thin-film solar cells on glass.

ZUSAMMENFASSUNG

In der vorgelegten Arbeit werden die strukturellen und elektrischen Eigenschaften von dünnen epitaktischen Si-Schichten untersucht. Hierzu wurde das Wachstum mittels Elektronenstrahlverdampfern auf Si-Wafern verschiedener kristallographischer Orientierungen sowie auf polykristallinen Si-Saatschichten auf Glas, ausgeführt. Insbesondere wird auf den Einfluss der Wachstumsparameter wie Substrattemperatur, Abscheiderate, Basisdruck sowie der Vorspannung der verwendeten Substrate eingegangen.

Die Ergebnisse zeigen eine Abhängigkeit der Schichtqualität von der Orientierung der Oberfläche des Substrats: (100) orientierte Schichten weisen eine geringere Defektdichte als (111) orientierte Schichten, und haben bei Verwendung in Solarzellen eine höhere Effizienz. Die Substrattemperatur als Wachstumsparameter wurde im Bereich von $T_s = 450-700 \text{ }^\circ\text{C}$ variiert. Es zeigt sich, dass eine Substrattemperatur von $T_s \geq 600 \text{ }^\circ\text{C}$ zur Reduktion der Defektdichte notwendig ist. Ein Einfluss des Basisdrucks auf die Schichtqualität bei Abscheideraten von 100-140 nm/min konnte bis zu einem Druck von 1×10^{-6} mbar nicht nachgewiesen werden.

Die Studie des Wachstums auf polykristallinem Si-Saatschichten auf Glas erweist eine starke Abhängigkeit der Qualität der epi-Schichten von der Orientierung des jeweils darunter liegenden Kristallkorns. Körner mit einer annähernd (100)-Orientierung enthalten erheblich weniger Defekte als die jeder anderen Orientierung. Des Weiteren wird gezeigt, dass Defekte innerhalb eines Kristallkorns auf Defekte in der AIC Schicht und/oder Defekte an der Grenzfläche von epi-Schicht und Substrat zurückgeführt werden können. Experimente zur Wasserstoff-Passivierung zeigen, dass die Effizienz der Solarzellen durch Passivierung der Defekte an Korngrenzen angehoben werden kann. Die derzeit effizientesten Dünnschicht poly-Si-Solarzellen auf Glas wurden durch Festphasen-Epitaxie mittels Elektronenstrahlverdampfung hergestellt. Diese Ergebnisse für wafer basierte Solarzellen belegen, dass Elektronenstrahlverdampfung eine vorteilhafte Methode zur Herstellung von Si Schichten sehr guter Qualität unter nicht UHV Bedingungen und hohen Abscheideraten ist. Für auf Glas basierende Strukturen ist eine Reduzierung der Defekte, verursacht durch Unreinheiten in der Keimschicht und Diffusion von Unreinheiten aus dem Glas-Substrat in die Schicht während des Wachstums, nach wie vor ausstehend.

TABLE OF CONTENTS

CHAPTER 1 Introduction.....	11
1.1 Thesis Objective.....	17
CHAPTER 2 Status of Low Temperature Si Epitaxy by E-beam Evaporation.....	19
2.1 Introduction.....	19
2.2 Evaporation of Si by E-Beam.....	20
2.3 Influence of the Crystallographic Orientation on Si Epitaxy.....	21
2.4 Influence of the Substrate Temperature on Si Epitaxy.....	22
2.5 Influence of the Si Deposition Rate on Si Epitaxy.....	23
2.6 Influence of Si Post-Ionization Stage on Si Epitaxy.....	24
CHAPTER 3 Experimental Methods.....	25
3.1 Substrate Materials.....	25
3.1.1 Mono-Si Wafer Substrates.....	25
3.1.2 Poly-Si Seed Layers on Glass.....	25
3.2 Substrate Cleaning.....	28
3.3 E-Beam Evaporation.....	28
3.3.1 Si Deposition Rate.....	31
3.3.2 Substrate Heating.....	32
3.3.3 Doping.....	33
3.3.4 Deposition Process.....	34
3.4 Post Deposition Treatment: Hydrogen Plasma Passivation.....	36
3.5 Solar Cell Structures.....	37
3.6 Characterization Methods.....	39
3.6.1 Scanning Electron Microscopy (SEM).....	39
3.6.2 Electron Back Scattering Diffraction (EBSD).....	39
3.6.3 Electron Beam Induced Current (EBIC).....	40
3.6.4 Cross-Sectional Transmission Electron Microscopy (TEM).....	40
3.6.5 Raman Spectroscopy.....	41

3.6.6	Hall Effect Measurements.....	41
3.6.7	Capacitance-Voltage (C-V) Measurements.....	42
3.6.8	Secondary Ion Mass Spectroscopy (SIMS).....	42
3.6.9	Current-Voltage (I-V) Measurements.....	42
3.6.10	Spectral Response Measurements.....	44
CHAPTER 4 Epitaxial Growth on Mono-Si Wafers.....		46
4.1	Introduction.....	46
4.2	Influence of Underlying Crystal Orientation.....	46
4.2.1	Doping Efficiency of Epitaxially Grown Si Films.....	50
4.3	Influence of Substrate Temperature.....	52
4.4	Influence of Si Deposition Rate.....	61
4.5	Influence of Base Pressure.....	64
4.6	Influence of Substrate Bias.....	67
4.7	Summary and Conclusions.....	70
CHAPTER 5 Epitaxial Growth on Poly-Si Seed Layers on Glass.....		73
5.1	Introduction.....	73
5.2	Properties of Poly-Si Seed Layers on Glass Prepared by AIC of a-Si	74
5.3	Epitaxial Growth on Poly-Si Seed Layers.....	75
5.3.1	Influence of the Substrate Temperature.....	76
5.3.2	Influence of the Underlying Grain Orientation.....	78
5.3.3	Intra-Grain Defects in Epitaxial Poly-Si Films.....	80
5.3.4	SIMS results.....	88
5.4	Epitaxial Growth on Poly-Si Seed Layers on Glass Prepared by Laser Crystallization (LC) of a-Si	91
5.5	Poly-Si Growth on Glass.....	95
5.6	Summary and Conclusions.....	98
CHAPTER 6 Solar Cells.....		100
6.1	Introduction.....	100

6.2	Wafer-Based Solar Cells.....	100
6.2.1	Influence of Substrate Temperature.....	101
6.2.2	Influence of Si Deposition Rate.....	104
6.2.3	Influence of Base Pressure.....	106
6.2.4	Influence of Substrate Bias	108
6.3	Glass-Based Solar Cells.....	109
6.3.1	Glass-Based Solar Cells (with a seed layer).....	109
6.3.1.1	Influence of Substrate Temperature.....	110
6.3.1.2	Glass-Based Solar Cells on AIC and LC Seed Layers...112	
6.3.2	Glass-Based Solar Cells (without a seed layer).....	114
6.4	Evolution of Wafer-Based and Glass-Based Solar Cells (with a seed layer).....	118
6.5	Summary and Conclusions.....	122
CHAPTER 7 Discussion.....		125
CHAPTER 8 Conclusions and Outlook.....		130
Annex I Role of Contamination for E-Beam Evaporation.....		131
List of Abbreviations.....		137
References.....		139
List of Author Publications.....		150
List of Author Presentations.....		153
List of Author Patents.....		154
Selbständigkeitserklärung.....		155

CHAPTER 1

Introduction

Renewable energy sources are becoming more important to fulfill the future energy demands. Today, 19 % of the global energy consumption is derived from renewable energies counting traditional biomass, large hydropower and “new” renewables (small hydro, modern bio-mass, wind, solar, geothermal and biofuels) [1]. Considering the expanding pollution and global warming issues, the demand for developing clean and cheap sustainable energy sectors has increased over the past decade and is expected to be more pronounced in the future.

Among all other renewable energy sources, photovoltaics is a promising energy source. It converts sun’s energy directly into electricity. Sunlight is free of charge and renewable. The contribution of the solar electricity production by photovoltaics has been increasing significantly during the last years. Especially, the grid-connected photovoltaic electricity was the fastest growing energy technology in the world, with 60 % annual increase in cumulative installed capacity between 2004 and 2009 [1]. The technology and market developments in photovoltaics are encouraging, nevertheless further cost reductions are essential in order to make PV a feasible energy source for the future.

Photovoltaics based on silicon (Si) solar cells are the most established route for realizing efficient conversion of sunlight into electricity. Si is an abundant material of the earth’s crust, stable, and non-toxic which makes it appealing for photovoltaic applications. The major fraction of the photovoltaic market today consists of monocrystalline (mono) and multicrystalline (multi) Si wafer-based solar cells. Mono-Si wafers have the potential to produce high efficiency solar cells due to their almost perfect crystalline structure without grain boundaries. The single crystal Si ingots are produced by Czochralski (CZ) or Floatzone (FZ) methods and afterwards sliced into 200-300 μm thick Si wafers that are used to produce the solar cells. The highest efficiency of 25.0 % has been achieved by using a mono-Si single junction solar cell (FZ wafer, PERL concept of UNSW, 4 cm^2) [2]. Additionally, cell efficiencies of 24.2 % by using rear contacted n-type mono-Si wafer (CZ wafer, Sunpower, 155.1 cm^2) and 23.0 % by using n-type mono-Si wafer (CZ wafer, HIT concept of Sanyo, 100.4 cm^2)

have been recorded [2]. Despite high efficiencies reached with mono-Si solar cells, expensive production steps and the material costs caused by thick mono-Si wafers make it hard to achieve substantial cost reduction. In comparison, multi-Si wafer-based solar cells are less expensive to produce but are less efficient than mono-Si wafer-based solar cells. Multi-Si wafers are made from cast square ingots that are produced from large blocks of molten Si carefully cooled and solidified. Due to the production steps the material has many grains with different size and crystallographic orientation. The highest efficiency reached so far by using multi-Si wafers yields 20.4 % (FhG-ISE, 1.002 cm²) [2]. In addition, other remarkable solar cell efficiencies achieved by multi-Si are 19.5 % (Q-Cells, laser fired contacts, 242.7 cm²) and 17.8 % (Q-Cells, 60 serial cells, 14920 cm²) [2]. Despite the improvements in technology and reduced production costs of Si wafer-based solar cells achieved so far, a substantial further cost reduction seems to be difficult due to the Si raw material costs.

Actually, c-Si solar cells of about 10 μm thickness with effective light trapping can reach the same short circuit current as conventional 300 μm thick Si wafer cells without light trapping [3]. This fact encouraged researchers to seek for ways of preparing thin Si wafers. First attempts to reduce wafer thickness have focused on thinning of a thick Si wafer by for example chemical etching. Using wafer thinning an efficiency of 21.5 % could be reached on a mono-Si wafer with a thickness of 47 μm [4]. However, difficulty in handling and fragility of thin Si-wafers are critical points of this method. Another approach focuses on epitaxial deposition of Si on low-cost Si substrates, followed by a removal of substrate (thin-film transfer) [5,6,7]. In this method re-use of the Si wafer substrate reduces the Si materials costs. Using the thin-film transfer method, an efficiency of 16.6 % has been published for a 45 μm c-Si film thickness (University of Stuttgart, 4.017 cm²) [8]. Recently, even a higher efficiency of 19.1 % was announced by ISFH (3.983 cm²) for a 43 μm thick c-Si solar cell from layer transfer using porous silicon [2]. However, reproducibility and up-scaling problems of this method should be considered for an industrial application. There are also innovative thin-film approaches based on Si-wafers like the so-called Sliver Cells, which allows use of less Si per unit area and greater area covered by unit mass of Si. In this method, Si wafers are sliced into stripes of 50 μm and transferred to a supporting substrate which results in an efficiency of 18-20 % [9]. However, all Si-wafer based thin-film approaches seem to have the difficulty of up-scaling to large areas and high throughput.

Low-cost and efficient thin-film solar cells require deposition of Si directly on a foreign substrate, development of low-temperature processes adapted to the substrate, passivation of grain boundaries and surfaces and light trapping. First attempts of preparing such thin-film solar cells have been realized by depositing amorphous Si (a-Si) or microcrystalline Si ($\mu\text{c-Si}$) on glass substrates. Discovered in 1970s, hydrogenated amorphous Si (a-Si:H) has gained attraction due to its low materials and manufacturing costs. The high absorption coefficient of a-Si:H results from its lack of crystalline order. However, the same disorder limits cell efficiencies due to tail states and mid-gap defects and results in a degradation known as the Staebler-Wronski effect or light induced degradation [10]. Though there has been significant investment in both identifying the origins of this problem and solving it, this technical limitation still exists. Thin-films of a-Si:H are usually deposited by Plasma Enhanced Chemical Vapor Deposition (PE-CVD) at low substrate temperatures of about 200 °C or lower by using silane and hydrogen gases on ordinary glass as well as on flexible substrates. The basic structure of a solar cell is a p-i-n structure, with an undoped (intrinsic) a-Si:H layer between two very thin doped layers. For a single junction a-Si:H solar cell initial efficiency of 12.7 % has been achieved by Sanyo (1 cm²) [11]. Stable efficiencies of a-Si:H solar cells reach 10.1 % (Oerlikon Solar Lab, 1.036 cm²) [2].

By adjusting the deposition conditions of a-Si:H (e.g. increasing substrate temperatures to about 350°C or by increasing the H dilution during PE-CVD), the material develops crystalline regions within the amorphous structure. This new structure is called hydrogenated $\mu\text{c-Si}$ ($\mu\text{c-Si:H}$). One important advantage of $\mu\text{c-Si:H}$ compared to a-Si:H is its stability against light induced degradation [12]. In addition, $\mu\text{c-Si:H}$ having a bandgap of 1.12 eV absorbs better in the near infra-red region of the spectrum compared to a-Si:H with 1.7 eV. The crystalline fraction of the growing material could be adjusted by the deposition parameters. The transformation region from the amorphous to the microcrystalline phase provided the most suitable absorber for PV applications [13]. The use of such longer-range order films were deemed to provide the path towards more stable and higher performances. A micromorph tandem cell concept was formed by a-Si:H/ $\mu\text{c-Si:H}$ stack to minimize the influence of degradation caused by the a-Si:H layer, and to benefit more from the solar spectrum. The micromorph tandem structure was further improved by the introduction of a transparent conductive oxide (TCO) as an intermediate reflector between top and bottom cell, which caused to an increase of the current in the a-Si:H cell [14,15]. Nowadays, the micromorph concept

reached to commercial reality with e.g. Kaneka which has reported stable sub-module efficiency of 11.7 % (14.23 cm²) [2]. Recently, even higher efficiencies of 11.9 % using a-Si/nanocrystalline Si (nc-Si) tandem cells (Oerlikon Solar Lab, 1.227 cm²) and 12.4 % using a-Si/nc-Si/nc-Si tandem cells (United Solar, 1.050 cm²) have been recorded [2]. Despite the developments obtained in a-Si:H and μ c-Si:H thin-film solar cells on glass, inherent properties of these materials may limit the cost reduction potential of this technology on the longer term.

An emerging thin-film technology area is polycrystalline-Si (poly-Si, grain size > 1 μ m) thin-films on foreign substrates as they have the potential to combine high material quality of c-Si (high efficiency) together with the advantages of thin-film approach like materials saving (low cost). Current research seeks ways of preparing high efficiency poly-Si thin-film solar cells on foreign substrates by a high throughput deposition method. Suitable approaches that are followed for producing poly-Si thin-film solar cells on foreign substrates can be classified as with and without a seed layer. Without seed layers, an a-Si precursor film of about 2 μ m (n⁺/p⁻/p⁺) is directly deposited on a textured glass substrate by PE-CVD and subsequently solid phase crystallized (SPC) at about 600 °C. The resulting poly-Si films feature a grain size of one to several micrometers. This method is called as crystalline silicon on glass and it has been commercialized by CSG Solar. A sub-module (94 cm²) efficiency of 10.5 % has been reached by applying post deposition treatments like rapid thermal annealing (RTA), hydrogen plasma passivation and using a sophisticated contacting scheme [16]. This result is really encouraging to show the potential of poly-Si thin-film solar cells on foreign substrates combining the proven strengths of c-Si material quality, while posing potential improvements over current thin-film manufacturing approaches.

Approaches based on a seed layer aim to achieve a larger grain size and as a result a better electrical quality of the poly-Si films. In this “seed layer approach” first a large grained (5-100 μ m) poly-Si seed layer is formed on the foreign substrate by different methods such as aluminum-induced-crystallization (AIC) [17] or laser crystallization of a-Si [18,19,20]. Generally, the resulting seed layers are highly doped thus they can not be used as an absorber layer. Therefore, these poly-Si seed layers are used as a template for the subsequent homo-epitaxial growth of thin poly-Si absorber layers. The resulting epitaxially grown poly-Si absorber layers also feature a large grain size (grain size > thickness of the epitaxial film) determined by the poly-Si seed layer properties. The doping level of the epitaxially grown poly-Si absorber layers can be

adjusted independent from the seed layer properties during the epitaxial growth. It is well known that epitaxial growth can supply high quality layers provided that the substrate properties and the growth conditions are adjusted accordingly.

Depending on the foreign substrate used, epitaxial growth processes on poly-Si seed layers can be divided into high temperature substrate (e.g. ceramic) and low temperature substrate (e.g. glass) processes. High temperature substrates such as ceramic can withstand temperatures in excess of 1000 °C. Poly-Si seed layers prepared by AIC of a-Si on ceramic substrates have been epitaxially thickened at temperatures of about 1100 °C using Chemical Vapour Deposition (CVD) [21]. Epitaxial growth could be obtained on the complete surface of the poly-Si seed layer including different grain orientations. Intra-grain defect density of the epitaxially grown poly-Si layers and the electrical activity of the defects have been studied [22]. The device open circuit voltages have been improved by applying hydrogen passivation [23]. Recently a solar cell efficiency of 8.5 % has been achieved by using high temperature epitaxy on poly-Si seed layers on alumina substrates [24].

Glass as a low temperature substrate, is well-suited for epitaxial growth of poly-Si thin films as it is a transparent, insulating and low-cost substrate. The development of borofloat glass which is more temperature stable than the commercial soda-lime glass encouraged the research in this field. Additionally, a thermal expansion coefficient similar to Si solved the problem of thermal mismatch for temperatures below about 600 °C [25]. However, glass still presents an enormous challenge for technology as well as basic research, since process temperatures are limited to about 600 °C for most commercial float glasses. Epitaxial growth at such low substrate temperatures becomes highly challenging. Therefore development of low temperature processing sequences adapted to the glass substrate is of great importance. Epitaxial thickening of poly-Si seed layers at such low temperatures were demonstrated by Electron-Cyclotron-Resonance CVD (ECR-CVD) [26], Hot-wire CVD (HW-CVD) [27], Layered Laser Crystallization (LLC) [28] and Ion Assisted Deposition (IAD) [29]. Using ECR-CVD, epitaxy could be obtained on Si(100) surfaces, whereas other substrate orientations caused non-epitaxial growth. At low substrate temperatures, crystallographic orientation of the substrate plays a crucial role for the subsequent epitaxy. Therefore epitaxial growth of the poly-Si seed layers prepared by AIC resulted in about 83 % of the seed layer surface to be epitaxially thickened [30]. In a recent work, epitaxial growth on almost 100 % of the poly-Si seed layer surface could be demonstrated [31]. The highest

solar cell efficiency achieved so far by using epitaxial poly-Si layers grown by ECR-CVD is about 1 %. Using HW-CVD the growth of 0.5 μm of epitaxy at about 670 $^{\circ}\text{C}$ could be demonstrated on poly-Si seed layers prepared by AIC [27]. In general, CVD methods suffer from a very low deposition rate of Si at such low temperatures. In LLC method a laser melting process is integrated during the epitaxial growth. Thin layers of a-Si are deposited and subsequently crystallized using an excimer laser. An efficiency of 4.8 % has been recorded for a 5 μm film thickness obtained by LLC [32]. Despite being an interesting technology with potential, its industrial applicability by deposition on large areas has to be demonstrated. IAD is a modified Molecular Beam Epitaxy (MBE) method, combining electron-beam (e-beam) evaporation of Si with a small fraction of ionized Si atoms generated by a so called Si post-ionization stage and accelerated towards the substrate. The use of accelerated Si ions is believed to promote low temperature epitaxy. The highest efficiency achieved so far using poly-Si seed layers by AIC and subsequent epitaxy by IAD is 2.2 % with an open circuit voltage of 420 mV [33]. A more detailed overview of the results achieved by IAD will be given in chapter 2 as it is closely related to this work.

The highest efficiency of a poly-Si thin-film solar cell on glass so far has been achieved by using PE-CVD for the deposition of Si based on the crystalline silicon on glass technology [16]. However, some of the main drawbacks of this deposition method include low deposition rates at low substrate temperatures and the use of toxic and explosive gases. Therefore, deposition costs of silicon by using PE-CVD determines the total production costs of the solar-modules. Consequently, the limitations of the PE-CVD method leads to a strong interest in finding alternative deposition techniques for the further cost reduction of thin-film Si solar cell production. E-beam evaporation of Si (the focus of this work) could be such an alternative as it provides several advantages over the conventional PE-CVD method. It allows for high deposition rates up to 1 $\mu\text{m}/\text{min}$ or even higher, that would reduce the deposition time for thin film absorbers dramatically. This high deposition rate also tolerates the non-ultra high vacuum conditions of the deposition system, which is an additional cost reduction for the industrial applications. The large area deposition of thin-films is possible by this method. The method includes no toxic gases and requires no plasma assistance. For all these reasons, utilization of high rate e-beam evaporation method instead of PE-CVD has the potential for substantial cost reduction in industrial production of thin-film Si photovoltaics.

1.1 Thesis Objective

The focus of this work is to investigate low temperature epitaxial growth of Si on mono-Si wafers as “ideal seed layers” with different crystallographic orientations as well as on poly-Si seed layers on glass substrates by non-ultra high vacuum, high-rate e-beam evaporation. In particular, the influence of underlying crystallographic orientation and the deposition parameters such as substrate temperature, deposition rate, base pressure and substrate bias on the structural and electrical properties of epitaxially grown Si absorber layers are investigated intensively. Epitaxial growth of Si on Si wafer substrates constitute a reference system for assessing the optimum growth conditions of Si. Later, these findings are transferred to optimize the epitaxial growth of Si on poly-Si seed layer coated glass substrates. The thesis is divided into following chapters:

Chapter 2: Status of Low Temperature Si Epitaxy by E-Beam Evaporation explains the working principle of e-beam evaporation, gives an overview about the state of the art and links this thesis to them.

Chapter 3: Experimental Methods explains the sample preparation steps that are used in this work. The e-beam evaporation system used for the low temperature epitaxial growth of the Si absorber layers is described in detail. Hydrogen plasma passivation and solar cell structures are explained. The characterization methods used for the investigation of structural and electrical properties of epitaxial Si films are described.

Chapter 4: Epitaxial Growth on Mono-Si Wafers explains the influence of crystallographic orientation and different deposition parameters like substrate temperature, Si deposition rate, base pressure and substrate bias on the structural and electrical properties of epitaxial layers that are prepared on mono-Si wafers.

Chapter 5: Epitaxial Growth on Poly-Si Seed Layers on Glass describes the structural and electrical properties of the epitaxial layers that are prepared on poly-Si seed layers on glass. Special emphasis is given to explain the origin of the defects in the poly-Si films. Epitaxial growth of Si on poly-Si seed layers prepared by AIC and laser crystallization (LC) have been compared. Finally, out-diffusion of impurities from the glass substrate and seed layer to the epitaxially growing absorber layer is discussed.

Chapter 6: Solar Cells explains the solar cell results of epitaxial layers grown on mono-Si wafers with different crystallographic orientations and on large

grained poly-Si seed layers on glass. Hydrogen plasma passivation of the Si absorber layer is investigated. Finally, the best solar cells achieved in this study (on mono-Si wafer and poly-Si seed layer on glass) are presented.

Chapter 7: Discussion gives the summary of different results of this thesis and compares them.

Chapter 8: Conclusions and Outlook summarizes the main results, and gives an overview about the important points concerning the low temperature Si epitaxy by e-beam evaporation with an outlook for the improvement of poly-Si thin-film solar cells.

CHAPTER 2

Status of Low Temperature Si Epitaxy by E-beam Evaporation

2.1 Introduction

E-beam evaporation of Si is a method for obtaining an uncontaminated and constant intensity Si beam for MBE. The homo-epitaxial growth of Si on Si wafer substrates has been intensively studied by MBE in the past [34-38]. The success achieved for the preparation of III-V semiconductors with sharp doping profiles by MBE has encouraged the use of this method for the deposition of other semiconductors such as Si [39]. Using MBE under the proper conditions of vacuum, Si source, substrate temperature, deposition rate, atomically clean surface of the substrate and lattice match between the over layer and the substrate, a uniform epitaxial layer with a low defect density is achievable. Despite the potential of achieving precise structures by MBE, during Si MBE different problems have been faced. One of the main problems include poor incorporation and segregation of dopant species during Si epitaxy at high substrate temperatures used [36,38]. Investigations to solve this doping problem have focused on using lower substrate temperatures [40] and low energy ion-implantation during growth [41-43]. However, lower substrate temperatures introduced a new challenge of limited epitaxial thickness of Si on different crystal orientations [38]. Typical MBE systems are operated under ultra-high vacuum conditions with low Si deposition rates of about 1 $\mu\text{m/h}$ in order to achieve the high quality epitaxial growth. Despite the fact that low deposition rates ensures the preparation of precise structures, this creates an obstacle of a high throughput that is necessary for the commercial application of Si MBE.

E-beam evaporation of Si is a promising method to supply a high-rate (up to 1 $\mu\text{m/min}$ or even higher) and uncontaminated Si beam for the epitaxial growth of Si. The high-rate deposition also enables the use of less stringent vacuum conditions. Therefore utilization of e-beam evaporation of Si for preparing high-quality Si epitaxial layers at low temperatures has the potential of achieving high-efficiency thin-film Si solar cells. In this chapter, the basic working principle of e-beam evaporation is

explained. An overview of the previous studies focusing on the influence of the crystallographic orientation, substrate temperature, deposition rate and Si post-ionization on the quality of Si epitaxial growth is discussed. Finally, the main focus of this work is introduced.

2.2 Evaporation of Si by E-Beam

In Si epitaxy, many different ways for producing an uncontaminated and constant intensity Si beam were tried for preparing high quality epitaxial films. Among them, sublimation of Si by crucible heating or by resistive heating of Si, and sputtering of Si were the most common ones [34]. The use of e-beam evaporation instead of above mentioned methods has several advantages. In this way, the interactions between the evaporant and the source walls may be greatly reduced. The heating energy transported by electrons can be concentrated on just the evaporating surface so that other portions of the evaporant and the source walls can be maintained at a lower temperature, causing the chemical interactions between the evaporant and the walls to be negligible. Unvala was the first who applied evaporation of Si by electron-bombardments for generating a clean Si vapor with high intensity for Si MBE [44,45]. Figure 2.1 illustrates the schematic drawing of a typical Si e-beam evaporation system.

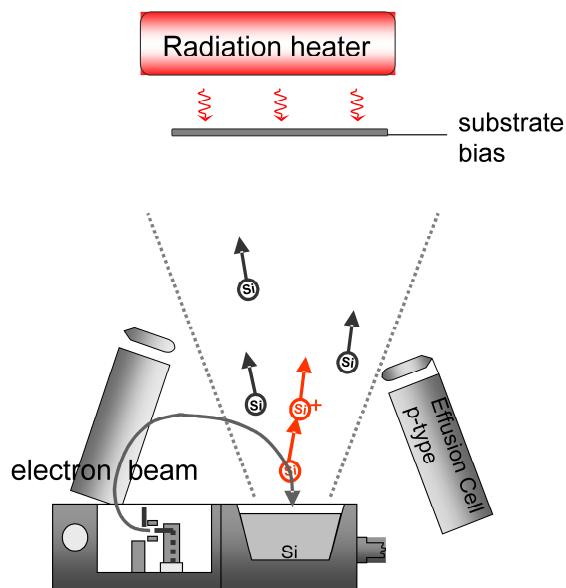


Figure 2.1 Schematic illustration of Si e-beam evaporation system

The basic working principle of the Si e-beam evaporation system is as follows: The high quality (e.g. FZ) Si source is placed in a deep crucible unit equipped with an electron-gun (e-gun) having a 270° electron-beam deflection. The deflected beam of electrons is accelerated through a field of several kV and focused on the Si evaporant surface. Upon impingement, most of the kinetic energy of the electrons is converted into heat, and temperatures exceeding 3000°C may be obtained. By this way, Si material is melted and evaporated. Evaporated Si can be in-situ doped by the co-evaporation of dopant atoms using effusion cells (e.g. with boron for p-type or phosphorous for n-type Si layers). The evaporated and doped Si is grown on the substrate which is placed below a substrate heater for controlling the substrate temperature.

Additionally, an optional Si post-ionization stage can be used for producing Si ions. The Si post-ionization stage has been first used by Oelting et al. [46,47] to investigate low temperature Si epitaxy for preparing thin-film solar cells. It is composed of a tungsten wire which is used to emit electrons under a certain applied current. These emitted electrons can collide with the Si atoms of the evaporated Si beam and ionize them. Using such a post-ionization stage a fraction of about 1 % of the evaporated Si can be ionized. These Si ions are then accelerated towards the substrate by applying acceleration voltages of several negative 10 V. It is assumed that these ions should provide additional energy to the silicon atoms on the surface which improves the low temperature epitaxial growth. The researchers that have used e-beam evaporation together with Si post-ionization stage named the method as ion assisted deposition (IAD).

The influence of the crystallographic orientation of the substrate and the growth conditions such as substrate temperature, Si deposition rate, and Si post-ionization stage on the structural and the electrical properties of the epitaxially grown Si layers deposited by e-beam evaporation have been partly investigated in the past. The summary of these previous investigations is given in the following sections.

2.3 Influence of the Crystallographic Orientation on Si Epitaxy

It is known from Si MBE that the underlying crystallographic orientation has a strong influence on the low temperature Si epitaxial growth [34,35,38]. In general, (111) epitaxial layers are found to be more susceptible to stacking fault formation than

(100) epitaxial layers. It was shown by measuring stacking fault density as a function of thermal cleaning time that generation of stacking faults is much more sensitive to surface cleanliness on (111) surfaces than on (100) surfaces [48]. The possible origins of these stacking faults were undesorbed siliconoxides or carbon contaminants.

For epitaxial growth of Si by IAD, mainly mono-Si wafers with (100), (111), (110) and (113) crystallographic orientations have been investigated as substrates. It was demonstrated that low temperature epitaxial growth of Si by e-beam evaporation is possible on different substrate orientations. However, the defect density and the minority carrier diffusion length strongly depend on the substrate orientation. It was shown that the number of extended defects in (100) oriented films is significantly lower than in non-(100) oriented films [49,50]. Layers grown on (110) and (111) oriented substrates grow also epitaxially, however with a considerably higher density of defects [51,52,53]. Due to the different density of defects, the epitaxial layer thickness (h_{epi}) is strongly related to the substrate orientation. It was found that $h_{\text{epi}}(100) \gg h_{\text{epi}}(113) > h_{\text{epi}}(110) = h_{\text{epi}}(111)$ [54]. The electrical quality of different oriented grains of the epitaxial layers grown on multi-Si wafers investigated by Laser Beam Induced Current (LBIC) measurements also demonstrate the difference in the collection efficiency of different oriented grains [52]. Open-circuit voltage measurements performed on solar cells prepared on (100) oriented substrates revealed higher values compared to the ones on (111) [50]. Crystallographic results obtained with epitaxial layers grown on poly-Si seed layers on glass exhibit regions with a microcrystalline growth and also regions with a lower defect density. Again the density of defects generated for the epitaxial layer strongly depends on the underlying crystalline orientation [55,56]. Finally, investigations on different crystallographic orientations revealed that epitaxy on (100) surfaces result in a higher quality compared to non-(100) surfaces.

2.4 Influence of the Substrate Temperature on Si Epitaxy

The influence of the substrate temperature (T_s) on the epitaxially grown Si layers has been shown for different crystallographic orientations. For (100) epitaxial layers, an enhanced defect density was found around $1 \times 10^3 \text{ cm}^{-2}$ which was independent of deposition temperature and growth rate [52]. However, the extended defect density on (110) and (111) epitaxial layers could be decreased by applying higher T_s [53,57].

The electrical measurements performed on (100) epitaxial films also reveal the influence of T_s . The minority carrier diffusion length measured in (100) epitaxial films increases with higher T_s [52]. The majority carrier mobility measured in the (100) epitaxial layers was found to be fairly insensitive to the variations of T_s and Si deposition rate for $T_s \geq 540$ °C [54]. Below 540 °C, mobility decreases with deposition temperature probably due to the increased number of defects which are generated at lower temperatures [58].

The open-circuit voltage (V_{oc}) of solar cells prepared by epitaxial growth on Si(100) wafers only weakly depends on T_s for 525-650 °C, and decreases for a growth temperature of 500 °C [59]. In comparison, V_{oc} and the diffusion length of solar cells prepared by epitaxial growth on multi-Si wafers increases towards higher T_s [60]. Influence of the initial substrate temperature and the final temperature on the V_{oc} of epitaxial layers on Si(100) and for epitaxial layers on poly-Si seed layers on glass have been also investigated [61,62]. However V_{oc} of poly-Si thin-film solar cells on glass decreased at elevated temperatures of 630-640 °C mainly due to the thermal stress between the film and the substrate [63].

In summary, the investigations of low temperature Si epitaxy by IAD revealed that T_s can control the extended defect density of especially non-(100) epitaxial layers. Although the electrical quality of (100) epitaxial films was found to be also strongly influenced by T_s .

2.5 Influence of the Si Deposition Rate on Si Epitaxy

An analysis of the extended defect density of the epitaxial layers grown on (100) substrates demonstrated that the defect density decreases by increasing the deposition rate for different substrate temperatures [58]. The corresponding V_{oc} of the solar cells shows a maximum at a growth rate of 200 nm/min for the films deposited at T_s between 550 °C and 650 °C [59]. For $T_s = 460-550$ °C, the minority carrier diffusion length increases with deposition rate and saturates at 200-300 nm/min. In general with increasing deposition rate, the concentration of contaminants in the epitaxial layer decreases and the minority carrier diffusion length peaks at 10.2 μm before decreasing again due to enhanced generation of structural defects. For a deposition temperature of

650 °C, a minority carrier diffusion length of 40 μm in a 21 μm thick epitaxial Si film deposited at a rate of 800 nm/min was demonstrated [64].

2.6 Influence of Si Post-Ionization Stage on Si Epitaxy

Two research groups investigated the influence of the Si ions on the epitaxially grown films. The results were discussed controversially. It was reported by Wagner that the use of Si ions during the deposition resulted in an increase of the density of trap levels [52]. The minority carrier diffusion length in the layers grown with a Si post-ionization stage increased with an increased acceleration voltage for deposition temperatures of 460 °C and 650 °C. At higher temperatures, however, the use of Si ions did not result in any further improvement of device. On the other hand, another study by Gorke showed that, the use of a Si post-ionization stage resulted in a higher density of extended defects in (111) epitaxial layers. This was mainly attributed to an outgassing of the system components due to the additional heating caused by the tungsten filament used for the electron emission [57]. In this work, a post-ionization stage has not been used. However, the e-beam itself also generates ionized Si atoms by the collision of the electrons from incoming beam and the evaporated Si atoms. These ionized Si atoms can be accelerated towards the substrate by applying a substrate bias. In this work, the influence of the applied substrate bias on the epitaxial film properties has been investigated. For all other investigations the substrate was held at ground potential.

CHAPTER 3

Experimental Methods

This chapter explains the sample preparation steps and experimental methods that have been used in the course of this work. E-beam evaporation is explained in detail as it has been used for the preparation of the epitaxial Si absorber layers. Finally, characterization methods that have been used for the investigation of structural and electrical properties of the Si films are described.

3.1 Substrate Materials

As substrates mono-Si wafers (“ideal seed layers”) with different crystallographic orientations and poly-Si seed layer coated glass substrates (Borofloat® 33, 0.7 mm) have been used.

3.1.1 Mono-Si Wafer Substrates

If not stated otherwise, boron doped mono-Si wafers; Si(100), Si(111) and Si(110) with a resistance of 2-10 mΩ-cm ($1-4 \times 10^{19} \text{ cm}^{-3}$) and with a thickness of about 375 μm have been used as substrates for the epitaxial growth of Si films. Three main crystallographic orientations of the wafers have been studied due to the reason that poly-Si seed layers contain different crystallographic orientation of the grains. In this study, mono-Si wafers serve only as “ideal seed layers”. This means they only provide the crystallographic information for the growing Si film. Low resistivity of the wafer substrate ensures that the substrate has almost no contribution for the light induced carrier collection.

3.1.2 Poly-Si Seed Layers on Glass

Poly-Si seed layers on glass have been prepared by aluminum-induced-crystallization (AIC) of a-Si. A typical process sequence for the formation of poly-Si seed layers used in this thesis is as follows:

- a) **Cleaning of the glass substrates:** The glass substrates (Borofloat® 33, 0.7 mm) have been cleaned using a normal glass cleaning solution (Mucosol) at about 80-90 °C for 20 minutes and rinsed in DI water. Finally the glass substrates have been dried by blowing nitrogen.
- b) **Deposition of Al layer:** About 300 nm thick Al layer has been deposited by DC magnetron sputtering on the cleaned glass substrates. The Al layer has been deposited at room temperature and with an Ar pressure of 6.5×10^{-3} mbar.
- c) **Oxidation:** To control the diffusion of Al and Si during the AIC process, a thin permeable membrane between the Al and a-Si layer is necessary. The membrane consists of a thin aluminum oxide layer formed by exposure to air of the Al-coated glass substrate for 2 hours. The membrane formation time and ambience have a distinct influence on the nucleation kinetics of the AIC process [65].
- d) **Deposition of a-Si layer:** A typically 375 nm thick a-Si layer was deposited onto the Al-coated glass in the same deposition chamber as the Al at room temperature. The thickness ratio between Al and a-Si determines the film properties in the following way; if the initial a-Si layer is too thin then the amount of Si is not sufficient to fill the volume of the former Al layer with crystalline Si. Hence the resulting poly-Si layers are not continuous. On the other hand, if the initial a-Si layer is too thick then the surplus amount of Si forms crystalline islands on top of the final poly-Si film.
- e) **Annealing of glass/Al/Aluminum oxide/a-Si stack:** Annealing of the initial glass/Al/Aluminium oxide/a-Si stacks at temperatures below the eutectic temperature of the Al/Si system ($T_{eu} = 577$ °C) leads to a layer exchange and a concurrent crystallization of Si. The stacks have been annealed in a tube furnace at an annealing temperature of 425 or 450 °C for several hours (8-15h) in N₂ ambient. After annealing, initial a-Si and Al layers exchange their position and a glass/poly-Si/Al(+Si) stack is formed (Figure 3.1). Due to the excess Si used, Si islands form on top of the final Al layer. More details concerning the nucleation and the subsequent grain growth during the AIC process can be found in [66,67,68]. During the AIC process, the membrane stays in place. Thus, the thickness of the resulting poly-Si film is determined by the thickness of the initial Al film (300 nm).

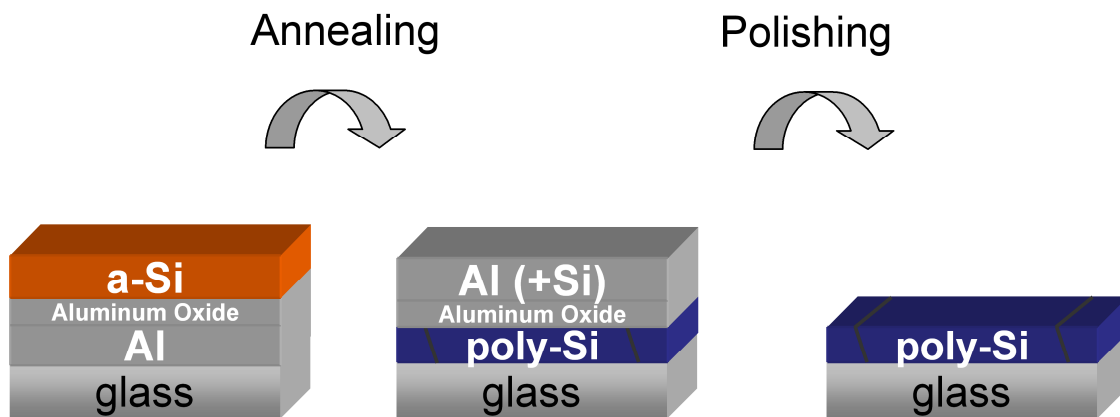


Figure 3.1 Schematic illustration of the aluminum-induced-crystallization (AIC) of a-Si. During an annealing step the initial glass/Al/a-Si stack is transformed into a glass/poly-Si/Al(+Si) stack. The permeable membrane between the layers stays in place during the whole process. Finally, Al layer with Si islands and the membrane are removed by chemical mechanical polishing.

- f) **Removal of Al(+Si) and the membrane:** Finally, the resulting top layer (Al and Si islands) and the membrane were removed by chemical mechanical polishing (CMP). For CMP we applied a Syton[®] HT-50 colloidal silica slurry (from DuPont Air Product NanoMaterials L.L.C). During the CMP process some part of the poly-Si film was also removed. Therefore, the final poly-Si seed layer has a thickness of about 200 nm. Finally, the samples were cleaned using hot water in an ultrasonic bath after CMP process and by a standard RCA procedure [69].

The physical phenomena of the AIC process has been described by Nast [70] as follows: The a-Si dissociates at the oxidized a-Si/Al interface, diffuses into the aluminum layer and starts to nucleate at the Al/a-Si interface. Si crystals grow within the former Al layer until they reach the Al/glass interface. Subsequently, the growth process proceeds laterally until neighboring Si crystals border onto each other. Finally, this leads to a continuous poly-Si film. The aluminum is displaced from its original position by the crystallizing Si, forming an Al layer on top of the poly-Si film. It has to be noted that the formation of an oxide layer between the a-Si and Al layer is of crucial importance for the functioning of the layer exchange process [70]. The driving force for the dissociation, diffusion and crystallization is the chemical potential difference

between the a-Si/Al interface and the c-Si/Al interface. Structural and electrical properties of the poly-Si seed layers on glass will be described in chapter 5 in detail.

3.2 Substrate Cleaning

The substrate surface is of crucial importance and must be free of metallic or organic contaminants for a high quality epitaxial growth. The 3 inch Si wafers and the glass substrates were cut into 25 x 25 mm². After cutting of the wafer substrates and the complete poly-Si seed layer preparation on glass, both substrates were cleaned by a standard RCA procedure [69]. Immediately prior to epitaxial growth, the substrates have been treated with 2 % HF for 30 s for the removal of native oxide. The wafer substrates were dipped into the HF solution. Since the HF solution would also etch the glass substrate strongly, they were treated by dropping the HF solution on the poly-Si seed layer surface carefully and not by dipping. Finally, the substrates were dried by blowing nitrogen. After the HF treatment, the substrates were immediately transferred to the load lock of the e-beam evaporation system for the epitaxial growth of the absorber layer. No additional in-situ cleaning was applied.

3.3 E-Beam Evaporation

Epitaxial growth of the Si absorber layers with a thickness about 2 μm on mono-Si wafer substrates and poly-Si seed layer coated glass substrates have been realized by non-ultra high vacuum (base pressure > 10⁻⁹ mbar), high-rate, low temperature e-beam evaporation system. The e-beam evaporation system is a modified commercial MBE system (Balzers UMS500). There exist two chambers, a load lock and a deposition chamber. The existence of a load lock allows keeping the deposition chamber still in high vacuum during the sample loading and unloading which is necessary for obtaining high quality epitaxial growth. The load lock is equipped with a scroll pump (Varian, SH-110, 90 l/min) and a turbo molecular pump (Balzers/Pfeiffer, TMU260, 230 l/s). The load lock temperature is held at about 50 °C (by the use of a heater) during loading and unloading of the substrates. Heating the load lock prevents the contaminants to stick on the chamber walls and enables faster pumping times. The substrates are transferred from the load lock to the deposition chamber (and vice versa) by the help of a

manipulator. In this work, a specially designed sample holder (stainless steel, diameter of 115 mm) has been used, which allows five samples to be deposited in the same deposition run with a sample size of $25 \times 25 \text{ mm}^2$. Thus, a combination of wafer and glass substrates, as well as wafers with different crystallographic orientations could be deposited in exactly the same deposition run. This allowed a direct comparison of the epitaxially grown absorber layer quality on different substrates. In addition, there exist sample holders with $98 \times 98 \text{ mm}^2$ and $76 \times 76 \text{ mm}^2$ for depositing Si on larger substrates.

The deposition chamber of the e-beam evaporation is equipped with a Cryogenic Pump (CTI Cryogenics ON-Board 8F, 1500 l/sec) which allows base pressures of about $3\text{-}5 \times 10^{-9}$ mbar. Note that, previously the deposition chamber was equipped with a turbo molecular pump. However, high-rate deposition of Si causes long pumping times and high power losses. Figure 3.2 illustrates a schematic drawing of the components used in the deposition chamber of the e-beam evaporation system. The partial pressures of the residual gases that play a critical role in the epitaxial growth were observed by a mass spectrometer (QME 125). In particular, partial pressures of hydrogen, oxygen, nitrogen, carbon, water and carbon dioxide were monitored during the whole deposition process. Another mass spectrometer (QME 425) which is placed closer to the substrate surface was used to monitor the Si flux. However, the attempts for using this spectrometer for controlling the Si deposition rate did not reveal reliable results. Therefore, the deposition rate was cross-checked afterwards by thickness measurements using a profilometer. There exists a shutter in front of the substrate holder equipped with a mirror. The mirror serves for observing the melt of Si in the crucible through a glass window before starting the deposition. The distance between the Si crucible and the substrate holder is 530 mm. The chamber walls are water cooled to ensure the vacuum quality in the chamber areas. In addition, a water cooled shroud is placed about 100 mm above the crucible with an opening in the middle which has a diameter of 70 mm. Since the sources are heated at high temperatures, the shroud surrounding the high temperature sites serve as a radiation shield. Hence, unwanted out-gassing from the components in the vacuum system, including the inner chamber wall are drastically reduced. The opening in the middle of the shroud is placed for the evaporation of the silicon. A cylindrical tantalum chimney is placed through this opening to minimize the Si deposition onto the parts of the e-beam evaporation system. The deposition chamber can be lifted by a pneumatic lifter for maintenance purposes.

Silicon is evaporated from a water cooled copper crucible (100 cm³) using an e-gun (ESQ300) with a 270° electron beam deflection. In that e-gun configuration, the electrons are forced into a curved path through a transverse magnetic field provided by

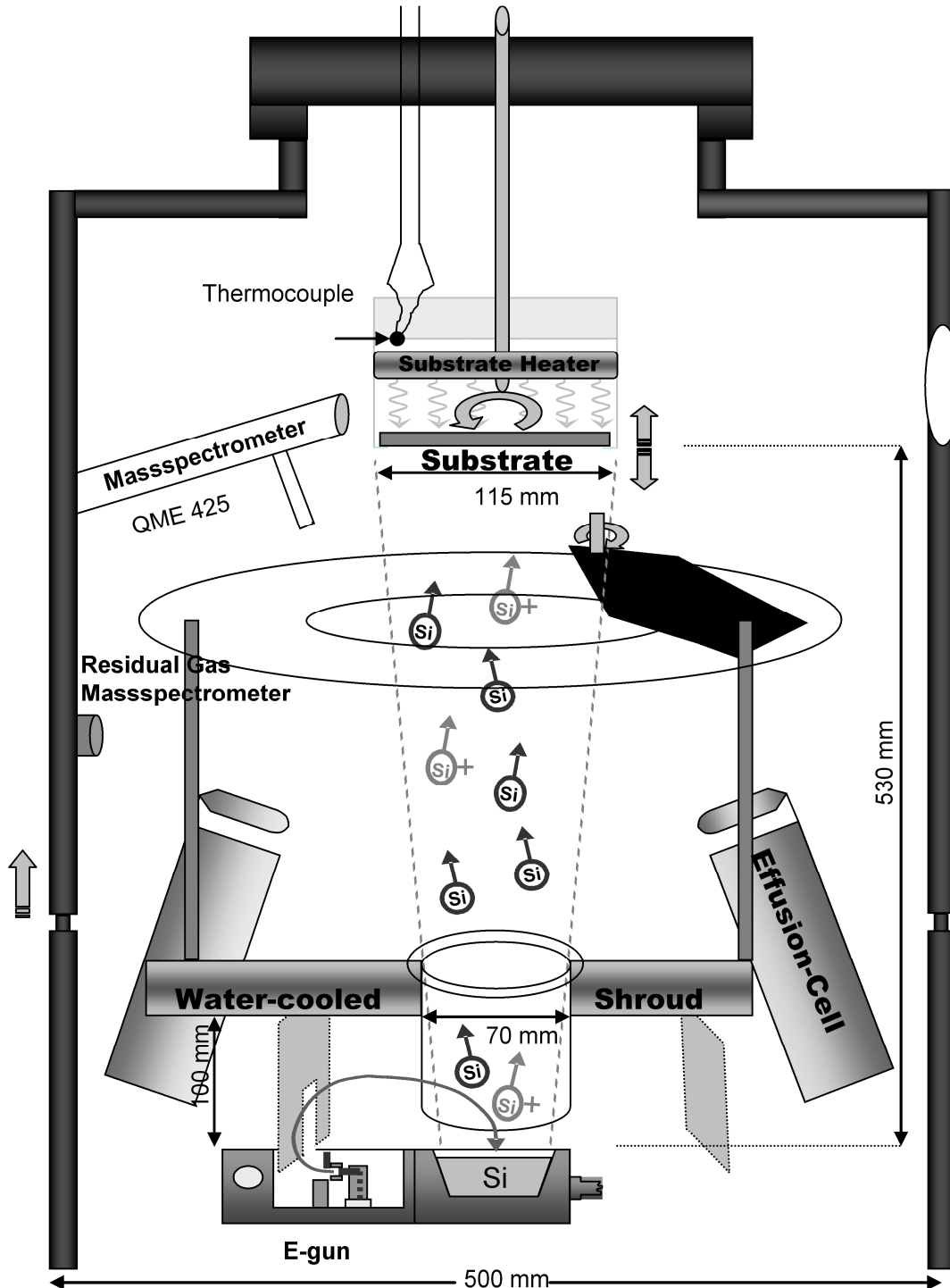


Figure 3.2 Schematic drawing of the components used in the deposition chamber of the e-beam evaporation system. The details are explained in the text.

an electromagnet, which permits focusing of the electron beam during operation. This allows the gun structure to be effectively separated from the vapour source without resorting too long distances. In a 270° deflection system, the tungsten filament of the e-gun is hidden from the Si substrate, which avoids possible tungsten contamination of the epitaxial films. Water cooling prevents melting of the Si at the edges of the crucible in order to impede contamination.

The high quality evaporation material Si has been supplied by the company Umicore with a purity of 99.9999% and a resistivity $> 1000 \Omega\text{cm}$ (undoped). The evaporation material is made of Si tablets with a diameter of 21 mm and a thickness of 5 mm. Regular shapes of the Si tablets makes the use of a magazine and a Si feeding system easier. A magazine filled with about 40 tablets is used for refilling the crucible. By this way the system can be kept closed for about up to $80 \mu\text{m}$ of silicon deposition.

3.3.1 Si Deposition Rate

The electrons are thermally emitted by resistive heating of the tungsten filament and accelerated towards the anode under a constant potential of 11 kV (Figure 3.2). The Si deposition rate (r_{Si}) was varied by adjusting the emission current (I_{em}) of the electrons

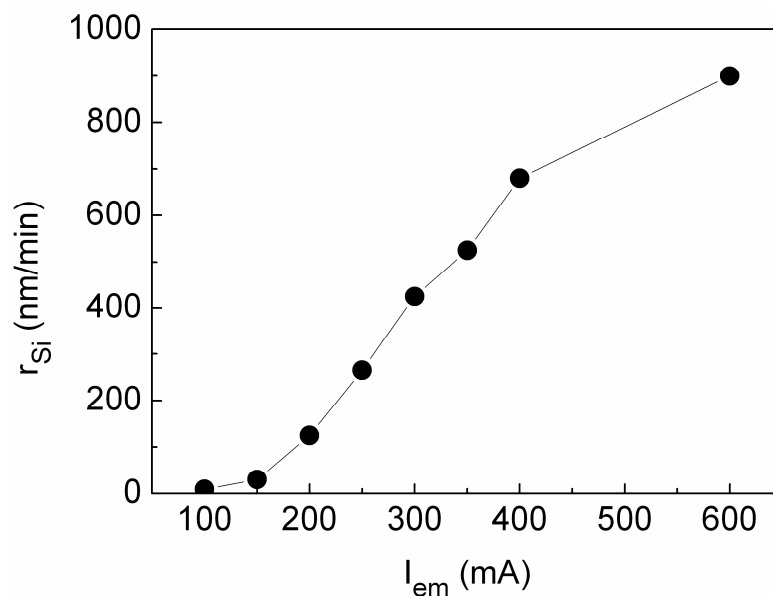


Figure 3.3 Si deposition rate (r_{Si}) controlled by adjusting the emission current (I_{em}) of electrons of the e-gun. For standard depositions a constant emission current of 200 mA was used.

from the e-gun. Principally, I_{em} can be varied up to 1 A. The e-beam evaporation method has a fast response time of the evaporant to the heating source, thus it is easy to modulate the evaporant beam intensity. Figure 3.3 presents the variation of the deposition rate (r_{Si}) for different applied I_{em} . The Si deposition rate gradually increases by increasing the emission current of the electrons.

As a standard, a constant $I_{em} = 200$ mA was applied for the Si depositions of this work. This resulted in an initial deposition rate of about 125 nm/min. After a longer use of the e-beam system the deposition rate increased up to about 300 nm/min for the same emission current used. This is caused by a better filled level of the Si material inside the crucible and a better controlled Si tablet melting process compared to the initial experiments. Therefore, the deposition rate of each experimental result will be indicated individually in the next chapters.

3.3.2 Substrate Heating

The substrates have been heated during deposition by a radiation heater which was made of graphite and was placed about 5 mm above the substrate holder (Figure 3.2). The substrate heating system was carefully designed to minimize out-gassing and maintain good vacuum conditions. This heater allows substrate temperatures of up to

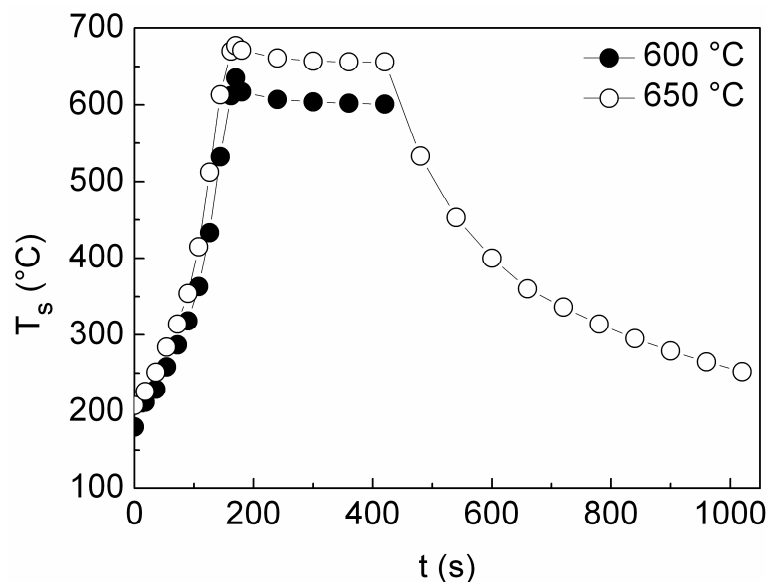


Figure 3.4 Substrate temperature (T_s) versus process time (t) during heating to 600 °C and heating/cooling for 650 °C measured by a thermocouple attached to a 3 inch Si wafer.

about $T_s = 800$ °C. A thermocouple connected to the back side of the heater measures the temperature. The temperature is regulated by the input of the thermocouple over a PID-controller. The temperature calibration was performed by using a “Sense Array”, a 3 inch Si wafer with five thermocouples connected on it. Fig 3.4 shows the substrate temperature (T_s) versus process time (t) for $T_s = 600$ °C and 650 °C respectively. For 650 °C also the cooling down phase was recorded. The substrates were heated from $T_s = 200$ °C to the target substrate temperature in 3 minutes (standard deposition procedure). The stabilization of the substrates temperature takes about 1 minute. At the end of the deposition, the substrate heater was switched off and the substrate left for cooling down naturally. The substrate heated to 650 °C cools down to 250 °C in 12 minutes. In order to have a homogeneous temperature distribution, an epitaxial layer thickness and a doping distribution over the samples the substrate holder was rotated during the depositions.

3.3.3 Doping

The doping of the evaporated Si was realized by co-evaporation of boron from a high temperature effusion cell. Thereby, p-type Si films were prepared. The adjustment of the doping concentration of the Si films was realized by controlling the boron effusion cell temperature. In other words, the deposition rate of Si was kept constant by a constant $I_{em} = 200$ mA applied and by adjusting the temperature of the boron effusion cell the flux of the evaporated boron was varied. In order to determine the principle doping range of the e-beam evaporation system, Si films of about $1\mu\text{m}$ thickness were deposited on Si(100) wafers at $T_s = 600$ °C with $r_{Si} = 150$ nm/min using different effusion cell temperatures. The temperature of the effusion cell was varied from 1600 °C to 2050 °C. The concentration of boron atoms in Si films was measured by secondary ion mass spectroscopy (SIMS) and is plotted as a function of the effusion cell temperature in Figure 3.5. The linear line in the figure represents a polynomial fit of data points. Corresponding concentrations of boron atoms in the Si films yield 1×10^{16} cm^{-3} (at 1600 °C) and 1×10^{19} cm^{-3} (at 2050 °C). This range allows the preparation of low doped absorber layers as well as highly doped layers acting as a back surface field. In order to achieve boron concentration levels higher than 1×10^{19} cm^{-3} , the Si deposition rate should be decreased. It is important to keep in mind that this is only the atomic

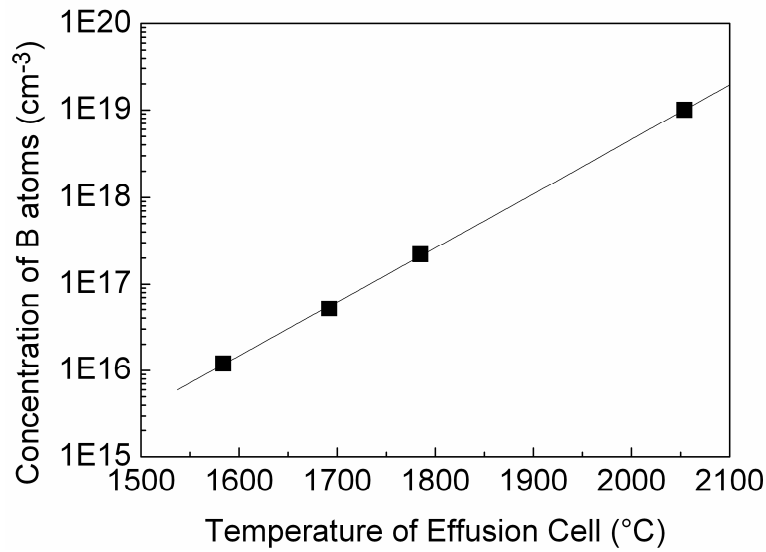


Figure 3.5 Concentration of boron atoms in the epitaxially grown Si films on Si(100) wafers versus the effusion cell temperature. ($T_s = 600$ °C, $r_{Si} = 150$ nm/min)

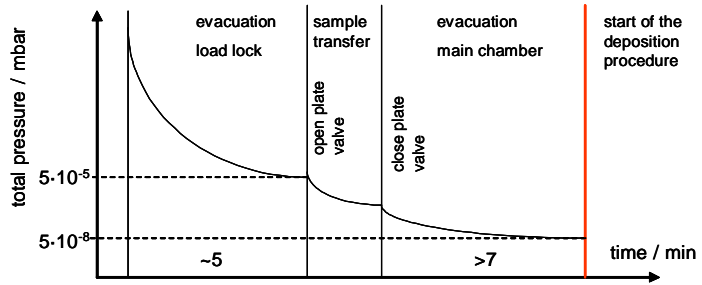
concentration of boron. The investigations of active carrier concentration and doping efficiency will be discussed in chapter 4.

Principally, a GaP effusion cell is also installed in the e-beam evaporation system, which may allow preparation of n-type Si films. The main concern about phosphorous doping is the high background level left after the deposition. In this work, n-type a-Si emitter layers were prepared by PE-CVD (section 3.5). So far the e-beam evaporation system was only used for the preparation of p-type Si layers.

3.3.4 Deposition Process

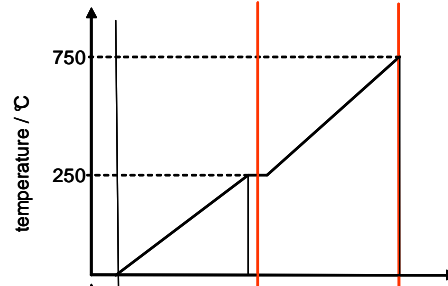
The deposition process is summarized in Figure 3.6. It comprises of the evacuation procedure, deposition procedure and cooling down phase. The HF treated substrates (wafer and/or poly-Si seed layer coated glass) are immediately loaded to the load lock of the e-beam evaporation system. After reaching a pressure of about 5×10^{-5} mbar (about 5 minutes), the samples are transferred to the deposition chamber by the help of the manipulator. This pressure level for the load lock is chosen to prevent fast contamination of the deposition chamber during the sample transfer. When a pressure of about 5×10^{-8} mbar is reached in the deposition chamber, the preparations for the deposition procedure begin. In general, the substrate temperature is held at a stand-by

Evacuation procedure

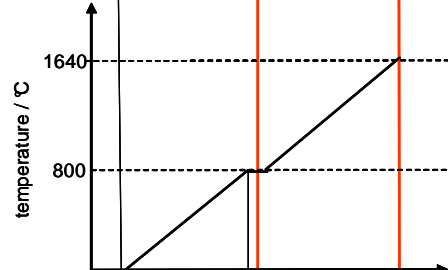


Deposition procedure

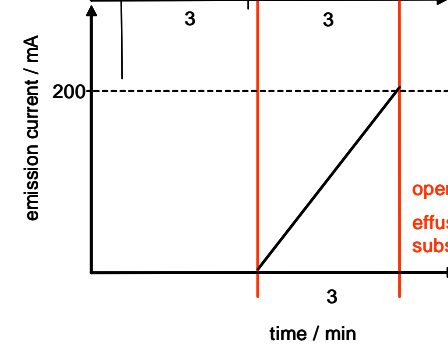
substrate heater



effusion cell



e-gun



Cooling down

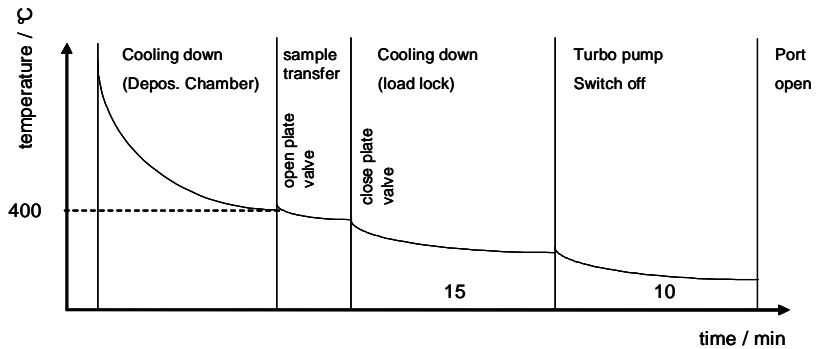


Figure 3.6 Overview of the Si deposition process. Details and explanation are given in the text.

temperature of 200 °C ($T_{\text{heater}} = 250$ °C) and the effusion cell at a stand-by temperature of 800 °C. When the desired low level of pressure is reached in the deposition chamber, the substrate temperature and effusion cell temperatures are increased to their desired values in 3 minutes, concurrently the substrates start to be rotated. For example, raising the substrate temperature and the effusion cell temperature to 600 °C and 1640 °C, respectively, yields a doping level of about $2\text{-}3 \times 10^{16}$ cm⁻³ in the epitaxial Si layers. In the meanwhile, the e-gun is switched on and the emission current is increased to 200 mA in 3 minutes. This level of the emission current of the e-gun provides a Si deposition rate of about 200 nm/min. Note that the deposition rate also depends on the amount (level) of Si in the crucible as already described before. In order to obtain higher Si deposition rates the emission current of the e-gun has to be increased. When the desired values of the substrate heater, effusion cell and emission current are reached the effusion cell shutter and finally the main shutter are opened to start the deposition. For a deposition rate of 200 nm/min, it takes 10 minutes to deposit 2000 nm thick p-type Si absorber layers. The e-beam evaporation system allows deposition rates as high as 1 μm/min. When the desired thickness of Si is reached, the main shutter is closed. In the cooling down phase, the substrate heater and effusion cell temperatures run back to their stand-by values. The emission current of the e-gun is slowly decreased and switched off. The samples wait in the deposition chamber until a heater temperature of 400 °C has been reached. Afterwards, the substrates are transferred back to the load lock. Finally, after a cooling down time of about 25 minutes in the load lock, the samples can be unloaded. With such a standard deposition process it takes in total less than 1 hour to deposit 2000 nm epitaxial Si layers.

3.4 Post Deposition Treatment: Hydrogen Plasma Passivation

Hydrogenation experiments were carried out in a special hydrogen plasma tool (developed by FAP Dresden, Germany together with the institute) which allows passivation temperatures of up to 650 °C. The passivation system consists of a hollow cathode plasma source (13.56 MHz). The remote lamp heater enables rapid heating and cooling rates. For the heating phase slow ramps were used around the transformation temperature ($T = 525$ °C) of the glass substrates. When the desired passivation temperature was reached, the plasma was ignited. Before the passivation, the samples

were treated with 2 % HF for 30 s to remove the native oxide on the surface of the epitaxial Si films. In this work, a passivation temperature of 600 °C and a passivation time of 10 minutes were used. The process partial pressure of H₂ is 1 mbar with a flux of 100 sccm. An 8 inch Si wafer was used as a carrier which permits passivation of many different samples in the same run. At the end of the passivation time, the samples were rapidly cooled down to 350 °C in about 3 minutes. In order to prevent the out-diffusion of hydrogen during the cooling down phase the plasma was still kept ignited. A detailed discussion concerning the influence of the hydrogen plasma passivation on the properties of the poly-Si films can be found in the work of Gorka et al [71,72] and is published in detail in the PhD thesis of B. Gorka [73].

3.5 Solar Cell Structures

The schematic sketch of the two solar cell structures that were used in the presented thesis are shown in Figure 3.7.a (wafer-based) and Figure 3.7.b (glass-based). Mono-Si wafers with different crystallographic orientations (Si(100) and Si(111)) (Figure 3.7.a) and poly-Si seed layer coated glass substrates (Figure 3.7.b) serve as templates for the epitaxial growth of the Si absorber layers. The epitaxial growth of the boron doped (p-type) Si absorber layers was realized by low temperature high-rate e-beam evaporation. The typical absorber layer thickness is 2 μm. After growing the epitaxial absorber layer, if not stated otherwise, post deposition treatment of hydrogen plasma passivation was applied for defect passivation. In some experiments as-grown solar cells (without hydrogen passivation) were also prepared in order to reveal the impact of hydrogenation. A rapid thermal annealing step which is typically applied for defect annealing was not used in this work. As hetero-emitters, highly phosphorous doped (n-type), about 10 nm thick a-Si:H layers were deposited by PE-CVD at 200 °C. The deposition parameters of the emitter layers were identical to the parameters which had led to high-efficiency wafer-based a-Si:H/c-Si heterojunction solar cells [74]. So far no special optimization of emitter layer deposition has been performed for poly-Si thin film solar cells on glass. In order to increase the lateral conductivity, a transparent conducting oxide (TCO) of about 80 nm thick ZnO:Al was deposited by reactive DC magnetron sputtering. This ZnO:Al film also provides an effective anti-reflective coating.

Finally, a photolithography process and subsequent wet-chemical mesa-etching were used to define the emitter area of the solar cells. After mesa-etching, metal contacts (Al) were evaporated on both the ZnO:Al and the absorber layer. The shape of the metal contacts was also defined by photolithography using a lift off process. There exist two different contacting schemes: a mesa structure (Figure 3.7.a) and an interdigitated structure (Figure 3.7.b). For the wafer-based solar cells a typical mesa etching was applied. For glass-based solar cells an interdigitated contacting scheme was used to lower the series resistance (R_s). The total area of a solar cell is $4 \times 4 \text{ mm}^2$. Analysis of the I-V measurements of the solar cells under illumination has to take the emitter area into account. The emitter areas of the mesa structure (wafer-based solar cell) and that of the interdigitated structure (glass-based solar cell) are 12.24 mm^2 and 8.55 mm^2 , respectively. Only for the best solar cell results (section 6.4) the current density was calculated using the active area of the solar cells which is 10.65 mm^2 for the mesa and 7.44 mm^2 for the interdigitated structure. Each substrate consists of 16 solar cells, 8 mesa and 8 interdigitated structures. For the wafer-based solar cells only the 8 mesa and for the glass-based solar cells only the 8 interdigitated structures were used for calculating the average solar cell parameters. For the measurement of glass-based solar cells white papers (2 sheets) were used as a diffused back reflector.

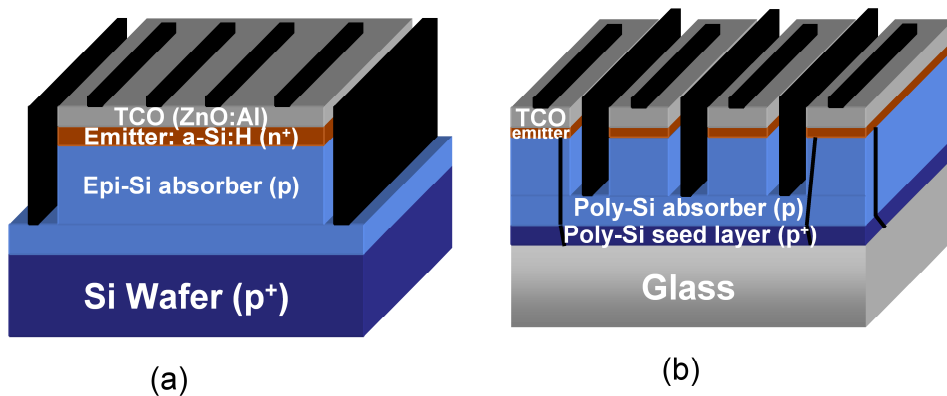


Figure 3.7 Schemes of (a) wafer-based (mesa) and (b) glass-based (interdigitated) (with poly-Si seed layer) solar cells that were used in the presented study. P-type c-Si absorber layers of about $2 \mu\text{m}$ were deposited by e-beam evaporation. N-type a-Si emitter layers of about 10 nm were deposited by PE-CVD (hetero-junction). The ZnO:Al film with a thickness of 80 nm serves as a transparent conductive front contact and an anti-reflective coating.

3.6 Characterization Methods

The structural and the electrical properties of the epitaxially grown mono-Si and poly-Si layers were characterized by the following methods.

3.6.1 Scanning Electron Microscopy (SEM)

The surface morphology of the epitaxially grown films was investigated by using a SEM (Hitachi S4100) equipped with a cold field emission cathode (5-25 kV). The samples were subjected to the electron bombardment and the secondary electrons were used to form the SEM micrographs. The epitaxial Si layers contain extended defects due to the low substrate temperatures used during the deposition of the films. These defects were revealed using an anisotropic defect etching (Secco etching for 10 s) [75]. The Secco etching solution was composed of 50 % HF and 0.15 ml/l $K_2Cr_2O_7$ in a ratio of 2:1. Afterwards the density of the extended defects was determined from SEM micrographs.

3.6.2 Electron Back Scattering Diffraction (EBSD)

The grain orientation distribution of the epitaxially grown poly-Si layers were determined by electron back scattering diffraction (EBSD). EBSD was performed in the SEM tool described above which was equipped with a back scatter diffraction camera. The samples were polished and placed with a 70° tilt in the EBSD set-up. When the electrons impinge on the specimen, they interact with the atomic lattice planes of the crystalline structures. Many of these interactions satisfy Bragg conditions and undergo backscatter diffraction. Due to the angle of the specimen, these diffracted electrons can escape the material and are directed towards and collide with the phosphor screen of the diffraction camera causing it to fluoresce. This fluorescent light is then detected by a low light CCD. The diffraction pattern contain Kikuchi bands, which correspond to each of the lattice diffracting planes and can be indexed individually by the Miller indices of the diffracting plane which formed it. By this way, the crystallographic orientation of the individual grains can be identified.

3.6.3 Electron Beam Induced Current (EBIC)

Electron beam induced current (EBIC) is a semiconductor analyses technique performed in a SEM. It is used to identify the recombination active defects (e.g. stacking faults, dislocations, grain boundaries) in semiconductors and to examine the minority carrier properties [76]. EBIC depends on the creation of electron-hole pairs by the microscopes electron beam. When the p and n sides of a solar cell (or a Schottky contact) are connected to an amperimeter and the sample is exposed to the electron beam, electron-hole pairs will be generated and separated by the internal electrical field. When the separated electrons and holes complete the circuit, a current will be measured. By this way, the electron beam is scanned across the sample and variations in the electron induced current are used to map the electronic activity of the sample. By using the signal from the amperimeter as the imaging signal, an EBIC image is formed on the screen of the SEM. When the sample is examined in top view, areas with good crystal quality will show a bright contrast, whereas areas containing defects will show a dark EBIC contrast. For the EBIC measurements, Schottky contacts were prepared on epitaxial Si films (p-type) on mono-Si wafer substrates and poly-Si seed layer coated glass substrates by the evaporation of Al. In order to complete the circuit also an ohmic contact is needed and this is realized by the deposition of an InGa alloy. For epitaxial Si films on Si-wafers the ohmic contact was placed on the back side of the wafer. For the glass samples however, both contacts were placed on the front surface with a certain distance to each other. The EBIC measurements of this study were performed in collaboration with University of Cottbus.

3.6.4 Cross-Sectional Transmission Electron Microscopy (TEM)

Cross-sectional transmission electron microscopy (TEM) is a microscopy technique where a beam of electrons strikes a thin specimen and part of it is transmitted through depending on the interactions with the specimen. These interactions are mainly effected by the film thickness, crystal orientation and the defects. Therefore TEM is extensively used for the determination of the origin of defects in the epitaxially grown films. An image is formed from the electrons transmitted through the specimen, magnified and focused by an objective lens and appears on an imaging screen. For

cross-sectional TEM investigations the specimens were prepared using the Focused Ion Beam (FIB) method. TEM investigations presented in this study were performed by Interuniversity Microelectronics Centre (IMEC), Belgium (Tecnai F30, 300 kV).

3.6.5 Raman Spectroscopy

Raman spectroscopy was used for determining the phonon properties; hence the crystallinity of the epitaxially grown layers on mono-Si wafer and poly-Si seed layer coated glass substrates. Raman measurements were performed using a HeNe laser with a wavelength of $\lambda = 632.8$ nm. An objective with a magnification of 100 was used to focus the laser to a spot with a diameter of about 1 μm . The Full-Width-Half-Maximum (FWHM) of the phonon line was determined by a Lorentzian fitting procedure. The spectral width is interpreted in terms of phonon confinement, i.e it is a measure for the density of defects in the films, as these determine the unperturbed phonon propagation. Therefore, small crystallites as well as the high density of defects in poly-Si films can lead to broadening of the Raman spectrum [77].

3.6.6 Hall Effect Measurements

Hall Effect measurements elucidate information about the electrical properties of the epitaxial Si layers. The electrically active dopant concentration, dopant type and mobility of the majority carriers of the epitaxially grown Si films were determined by this method. Most of the measurements were performed at room temperature with a magnetic flux of 0.64 T, in Van-der-Pauw Geometry [78] by depositing ohmic contacts on the four corners of a specimen. P-type epitaxial Si layers were deposited on n-type Si(100) wafers (> 3 k Ωcm) to eliminate the influence of the substrate during the measurement. As ohmic contact, gold with a thickness of 20 nm was thermally evaporated through a shadow mask on the four corners of the samples. The sample size was 4.9 x 4.9 mm². Then the sample was placed on a ceramic plate with 4 contact points and the ohmic contacts of the sample were connected by using gold-wires. For some of the samples a temperature dependent Hall Effect was measured for the temperature range of 20-300 K. The temperature variation of the measurement gives more information concerning the scattering mechanism present in the epitaxial films.

3.6.7 Capacitance-Voltage (C-V) Measurements

C-V measurements give information about the ionized acceptor/donor level present within the epitaxial layers and information concerning the quality of the p-n junction [79]. For these measurements a C-V analyzer and a voltage supply from Keithley instruments were used. P-type epitaxial Si layers were grown on p⁺-Si(100) wafers and liquid mercury was used to form the Schottky contact.

3.6.8 Secondary Ion Mass Spectroscopy (SIMS)

Secondary ion mass spectrometry (SIMS) is a technique used to analyze the composition of solid surfaces and thin films by sputtering the surface of the specimen with a focused primary ion beam and collecting and analyzing ejected secondary ions. These secondary ions are measured with a mass spectrometer to determine the elemental, isotopic, or molecular composition of the sample. As ion guns Cs⁺ or O⁺ were used (14,5 keV). Using a constant sputtering rate, the depth profile of the impurities ejected from the samples was analyzed. Mainly contaminants such as C, O and N, as well as dopant impurities such as B and Al were examined for epitaxial layers on mono-Si wafer substrates and poly-Si seed layer coated glass substrates. Also the metal impurities (Fe, Cu, Ta, W, Mo) were measured for some of the samples. The measurements that are presented in this work were performed by the company RTG Mikroanalyse GmbH.

3.6.9 Current-Voltage (I-V) Measurements

The current-voltage (I-V) characteristics of the solar cells were measured under 1 Sun illumination (AM 1.5, 100 mW/cm²). Figure 3.8 depicts the typical I-V characteristic of a solar cell under illumination. Open circuit voltage (V_{oc}) is the voltage obtained when the circuit operates under open circuit conditions (current is zero), similarly short circuit current (I_{sc}) is the current generated when the circuit operates under short circuit conditions (voltage is zero). The fill factor (FF) is a measure of the squareness of the I-V characteristics and is always less than 1. It is the ratio of the two areas shown in Figure 3.8:

$$FF = \frac{P_{\max}}{I_{sc} V_{oc}} = \frac{V_{\max} I_{\max}}{I_{sc} V_{oc}} \quad [80]$$

where P_{\max} , V_{\max} , and I_{\max} refer to the electrical maximum output power, the voltage and the current corresponding to the maximum power, respectively. The conversion efficiency (η) of a solar cell is defined as the ratio of the maximum power (P_{\max}) output to the incident power of the light (P_{in}):

$$\eta = \frac{P_{\max}}{P_{in}} = \frac{V_{\max} I_{\max}}{P_{in}} = \frac{I_{sc} V_{oc} FF}{P_{in}} \quad [80]$$

Among significant parameters of the solar cell that can be extracted from I-V characteristics are the series (R_s) and parallel resistances (R_p). R_s is determined by the slope of the I-V curve under open circuit conditions, where as R_p is determined under short circuit conditions. For the ideal solar cell R_s would be zero and R_p would be infinite.

The solar cell is placed on a temperature controlled sample holder and contacted with 4 point probes. The wafer-based solar cells were measured at 25 °C; where as glass-based solar cells were measured at 26 °C. The incident light intensity was calibrated with a reference solar cell. For the illuminated I-V measurements of the glass-based solar cells, white papers (2 sheets) were used as a back reflector.

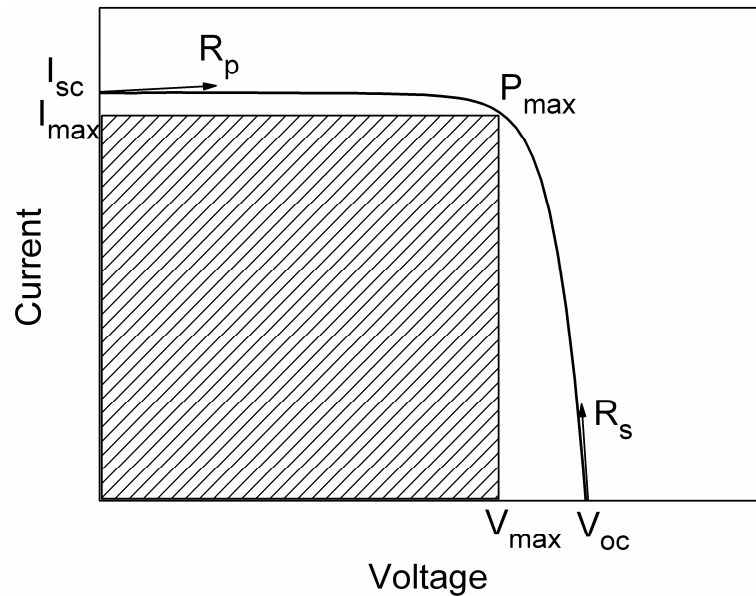


Figure 3.8 Current-Voltage (I-V) characteristics of a solar cell under illumination

3.6.10 Spectral Response Measurements

Quantum efficiency (QE) refers to the percentage of photons that are converted to electric current (i.e., collected carriers) when the cell is operated under short circuit conditions. The QE is most usefully expressed as a spectral response (SR) measurement (that is, as a function of photon wavelength or energy). Therefore, QE relates to the response of a solar cell to the various wavelengths in the spectrum of light. Since some wavelengths are absorbed more effectively than others in most semiconductors, spectral measurements of quantum efficiency can yield information about which parts of a particular solar cell design are most in need of improvement. If all the photons of a certain energy are absorbed, and the resulting minority carriers are collected (e.g. electrons in p-type absorber layer) then the QE at that particular wavelength has a value of 1. The QE for most solar cells is reduced because of the effects of recombination, where charge carriers are not able to move into an external circuit. From theoretical aspect, the QE corresponds to the SR, which determines the spectral distribution of the short circuit current. The SR is given by:

$$SR(\lambda) = \frac{I_{sc}(\lambda)}{P_{beam}(\lambda)} \quad [80]$$

where I_{sc} is the short circuit current and P_{beam} is the wavelength dependent power of the beam. To determine the SR, I_{sc} is measured as a function of the wavelength (λ) of the incident monochromatic light. The wavelength λ is usually scanned from 300-1200 nm which is the interesting region for the Si based solar cells. The set-up is equipped with a monochromatic light and in addition with a continuous white light. The SR of the solar cell is measured with a lock-in amplifier.

The QE spectrum reflects the cell design and the material quality. For a p-n junction solar cell the short wavelength response is provided at the front of the cell. Since, carriers generated near the front surface are susceptible to surface recombination, the short wavelength QE is particularly sensitive to the surface recombination velocity. Surface recombination velocity can be reduced by passivating the surface. Long wavelength QE is affected by the back-surface quality and the thickness of the cell. The abruptness of the QE edge reflects the form of the absorption.

The QE involves EQE and IQE, which stand for external quantum efficiency and internal quantum efficiency, respectively, with the latter defined as the number of minority carriers contributing to the short circuit current divided by the number of photons entering the cell. External Quantum Efficiency (EQE) is the fraction of incident photons that are converted to electrical current and it is calculated as follows:

$$EQE(\lambda) = SR(\lambda) \frac{hc}{q\lambda} \quad [80]$$

where h is Planks constant, c is speed of the light and q is the charge of an electron.

CHAPTER 4

Epitaxial Growth on Mono-Si Wafers

4.1 Introduction

This chapter describes the growth of epitaxial Si films on mono-Si wafers by e-beam evaporation. In particular, the influence of the underlying crystallographic orientation and the growth parameters on the structural and the electrical properties of the epitaxial Si films grown on Si(100) and Si(111) wafers are investigated. In the course of this thesis, mono-Si wafers serve as an “ideal seed layer” reference when assessing maximum achievable electronic quality for a particular e-beam evaporation process. (100) and (111) crystallographic orientations are chosen due to the fact that they constitute the main crystallographic orientation distribution of the poly-Si seed layers on glass as it will be introduced in the next chapter. In this chapter, the epitaxial growth of Si on Si(100) and Si(111) wafers are compared. Then the doping efficiency of the epitaxially grown Si films on Si(100) is presented. The growth parameters examined are substrate temperature, Si deposition rate, base pressure and substrate bias. For each section, structural and electrical properties of the epitaxial films are discussed separately.

4.2 Influence of Underlying Crystal Orientation

Structural Properties

Boron doped Si films of about 1.8 μm thickness were grown on Si(100) and Si(111) wafers at $T_s = 600\text{ }^\circ\text{C}$ and afterwards Secco-etched to reveal the defects. Figure 4.1 presents the SEM images of the defect-etched surfaces of epitaxially grown Si films. As seen in Figure 4.1.a, (100) epitaxial layers do not exhibit any etch pits typical for dislocations or stacking faults of Si(100) epitaxy within the detection limits of SEM. This illustrates the high structural quality achieved on (100) surfaces by using e-beam

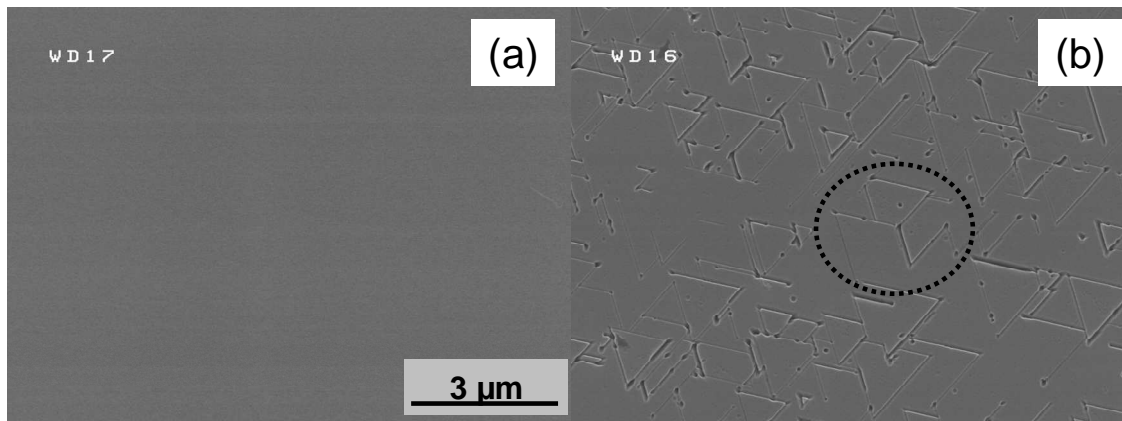


Figure 4.1 SEM images of Secco-etched surfaces of epitaxially grown Si films on (a) Si(100) and (b) Si(111) wafers at $T_s = 600$ °C. (100) epitaxial layer exhibits no extended defects. (111) epitaxial layer shows stacking faults (triangles) and dislocations (circles). The marked region (dashed circle) illustrates inter-grown stacking faults.

evaporation. In the literature, using an optical microscope an extended defect density of about $1 \times 10^3 \text{ cm}^{-2}$ for (100) epitaxial layers has been reported [52].

In comparison, the (111) epitaxial layer grown by e-beam evaporation shows etch pits typical for stacking faults (triangles) and dislocations (circles) (Figure 4.1.b). However, the stacking fault density is drastically higher compared to the dislocation density. Counting the number of triangular etch pits on the surface, the density of stacking faults has been calculated. The density of the stacking faults on (111) epitaxial layer yields about $1 \times 10^8 \text{ cm}^{-2}$. The stacking faults are formed along the $\{111\}$ planes

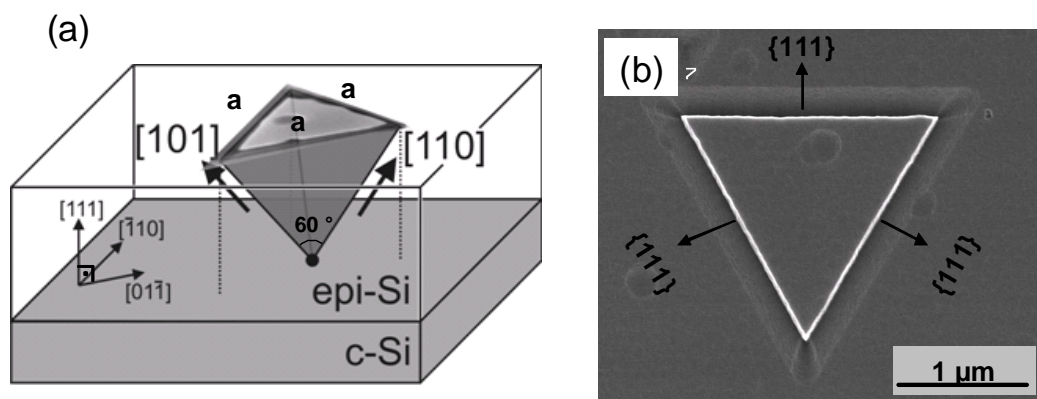


Figure 4.2 Sketch of stacking faults observed on epitaxially grown Si films on Si(111) wafers (a) and the SEM image of an etch pit with $\{111\}$ planes.

resulting in an inverted equilateral triangular pyramid in the epitaxial layers (Figure 4.2.a). These triangles on the sample surface correspond to the base plane of this tetrahedron (Figure 4.2.b). From the size of the triangles it is possible to calculate the origin of the stacking faults. In Figure 4.1.b, triangles with similar size (originating at the same depth) and triangles of a smaller size (defects in the epitaxial layers) coexist. This means, stacking faults have a depth distribution within the epitaxial layers.

Figure 4.3 presents the depth distribution of the origin of stacking faults for an epitaxial film grown on Si(111) wafer at $T_s = 600$ °C. A high defect density originates at the interface of the substrate epitaxial film and can be explained by the surface treatment before deposition. In this work, no in-situ oxide removal process was used. Only a HF dip was applied to the substrate surface prior to loading the sample into the vacuum system. However, it is well known that H desorbs from the Si surface as trihydride by 200 °C, as dihydride by 400 °C and as monohydride by 550 °C [81]. Considering a typical substrate temperature of 600 °C, we can estimate that H desorbs from the substrate surface already before the start of the deposition. However, most defects have their origin in the bulk of the film. In this case in a depth between 0.4 and 1.4 μm . We assume that most of the defects have been created during the epitaxy, probably due to non-ultra high vacuum conditions of the e-beam system.

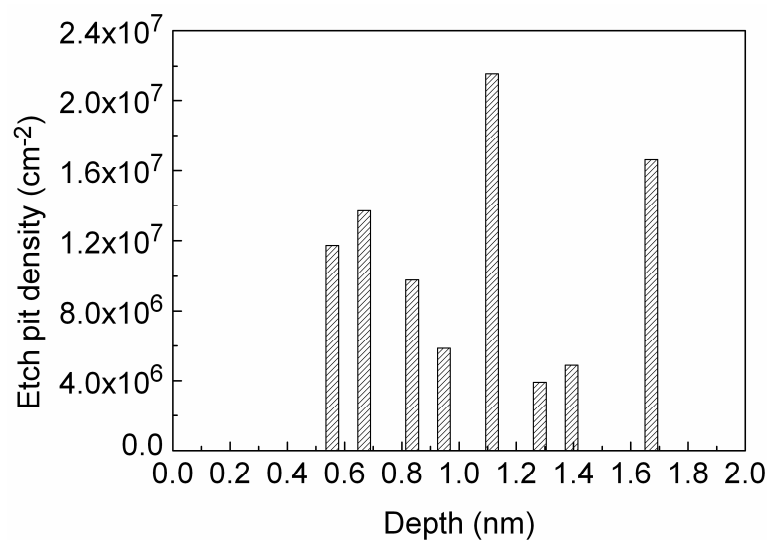


Figure 4.3 Etch pit density probed as a function of the depth of their origin in the epitaxial Si film grown on Si(111) wafer at $T_s = 600$ °C (thickness = 2 μm)

Electrical Properties

For the detection of electrical activity of the defect centers in the epitaxially grown layers, EBIC measurements have been performed. The EBIC collection efficiency versus the beam energy for the epitaxially grown films on Si(100) and Si(111) wafers at $T_s = 600$ °C are plotted in Figure 4.4. The beam energy of 15 keV is marked in the figure which corresponds to a penetration depth of 2 μm (epitaxial Si film thickness) by the vertical dashed line. The collection efficiency is affected by the electrically active defect centers that act as recombination centers and hence decrease the charge carrier collection from the junction. The maximum collection efficiencies measured in (100) and (111) epitaxial layers yield about 93 % and 82 %, respectively. The collection efficiency of the (100) epitaxial films is obviously higher than that of the (111) epitaxial films for the whole beam energy (penetration depth) range that was measured. The difference in the collection efficiency is in good agreement with the difference in extended defect densities observed for the two epitaxial films (Figure 4.1). It can be inferred that extended defects that are observed for epitaxial films grown on Si(111) wafers are electrically active and may degrade the device quality.

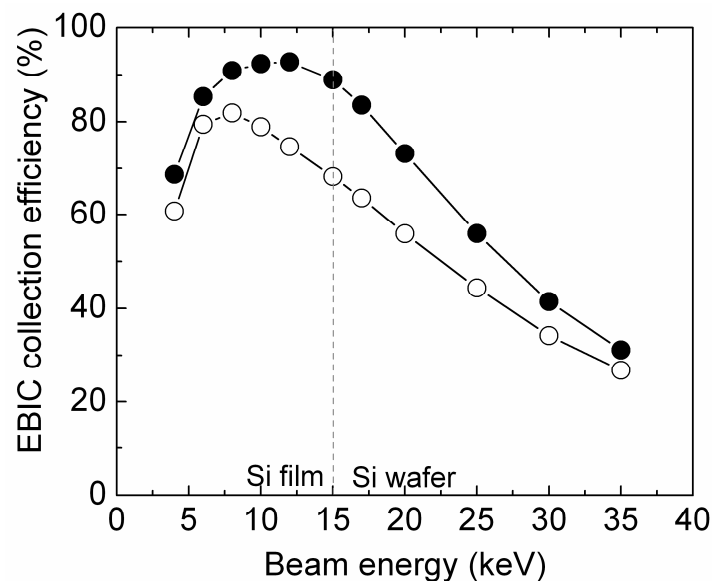


Figure 4.4 EBIC collection efficiency versus the beam energy for the epitaxial Si films grown on Si(100) (●) and Si(111) (○) wafers at $T_s = 600$ °C.

4.2.1 Doping Efficiency of Epitaxially Grown Si Films

Epitaxial Si films were doped by the co-evaporation of boron from a high temperature effusion cell. The doping level of the epitaxial Si films was calibrated for a given substrate temperature of 600 °C and a constant Si deposition rate of about 150 nm/min for the epitaxial Si films grown on Si(100) wafers. A substrate temperature of 600 °C was chosen to be able to transfer the results to the glass substrates later on. The doping level of the epitaxial films was varied by changing the effusion cell temperature. By SIMS measurements the concentration of B atoms were determined while C-V and Hall effect measurements revealed the electrically active concentration of the dopant atoms. Figure 4.5 summarizes these measurements by probing the carrier concentrations determined by Hall effect and C-V as a function of the atomic boron concentration. A wide doping range from about 1×10^{16} to about $1 \times 10^{19} \text{ cm}^{-3}$ could be obtained by varying the effusion cell temperature (see Figure 3.5). The comparison of atomic concentration of boron atoms incorporated to the measured carrier density gives the information about the doping efficiency of the investigated layers. The straight line in Figure 4.5 represents full activation of the dopant atoms. From the measurement results it is clearly seen that for epitaxial Si films all of the incorporated boron atoms are also

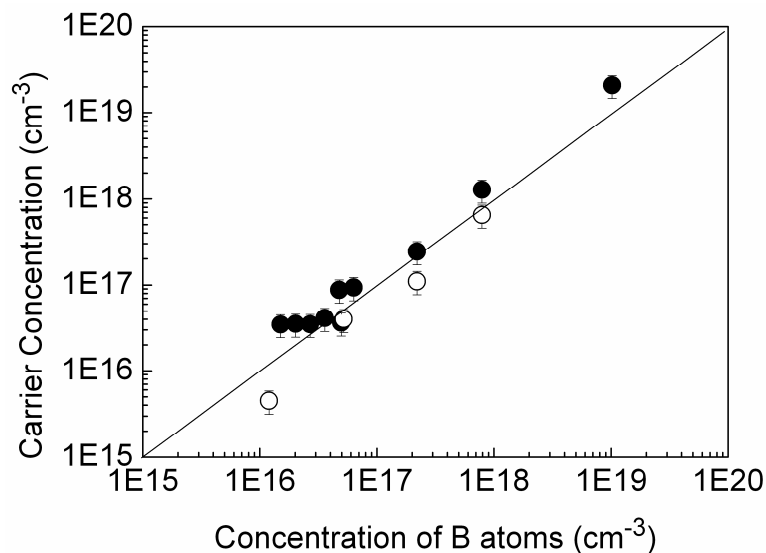


Figure 4.5 Carrier concentration (holes) determined by Hall effect (●) and C-V (○) as a function of the concentration of boron atoms measured by SIMS. The straight line represents the full activation of the carriers. The error bars represent the error caused by the measurements.

electrically active, resulting in a doping efficiency of unity. Note that, Hall effect measurements yield slightly higher carrier concentrations in comparison to C-V measurements. Due to the principle doping range, by using e-beam evaporation it is possible to prepare low doped absorber layers (p) or if needed highly doped Si layers (p^+) as well. Lowering the Si deposition rate (< 150 nm/min), even higher doping levels can be achieved. For very low-doped Si layers with $\leq 10^{16}$ cm $^{-3}$, the conductivity type of the layers change from p-type to n-type. From previous investigations, it is known that intrinsic (unintentionally doped) epitaxial films prepared by the same e-beam system exhibit an n-type conductivity [57] which can be explained by the background level of residual O $_2$ which acts as a donor in Si once incorporated in the growing epitaxial films. For this reason, the carrier concentration of the epitaxial films investigated in this study was adjusted to $3-4 \times 10^{16}$ cm $^{-3}$.

The mobility of majority carriers (holes) in the epitaxial Si films versus carrier concentration determined by Hall-effect measurements is plotted in Figure 4.6 for the carrier concentration range investigated above. As a reference mobility of holes in bulk c-Si is calculated by the formula (inset of Figure 4.6) [82] and plotted together. The mobility of majority carriers in the epitaxial Si films decreases with increasing carrier

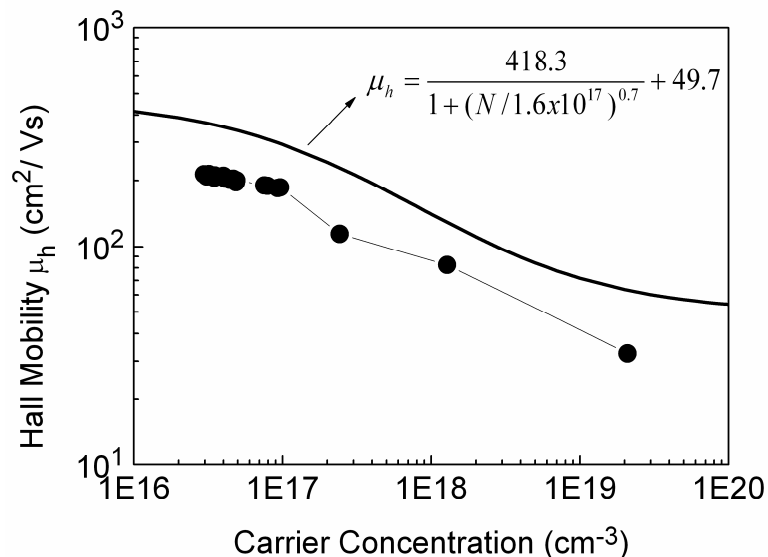


Figure 4.6 Mobility of majority carriers (holes) versus carrier concentration in the epitaxial Si films grown on Si(100) wafers at $T_s = 600$ °C, experimentally measured by Hall-effect (●) and as reference calculated by the formula (inset) for bulk c-Si (solid line) [82]. N refers to the carrier concentration.

concentration as a result of increased impurity scattering. For carrier concentrations of about $3\text{-}4 \times 10^{16} \text{ cm}^{-3}$, the mobility of holes yields about $200 \text{ cm}^2/\text{Vs}$. The high mobility that has been reached can be addressed to the high crystalline quality of (100) epitaxial layers prepared by e-beam evaporation. In comparison, the mobility of holes in the bulk c-Si for the same carrier concentration level is about $350 \text{ cm}^2/\text{Vs}$. Note that, the mobility of holes in the epitaxial layers is still lower compared to that of bulk c-Si for the whole carrier concentration range.

4.3 Influence of Substrate Temperature

Structural Properties

The substrate temperature (T_s) is one of the most critical growth parameters since it controls the surface processes such as adatom mobility for the low temperature epitaxial growth. Epitaxial Si layers were grown on mono-Si(100) and Si(111) wafers at substrate temperatures of $T_s = 450\text{-}700 \text{ }^\circ\text{C}$. The crystalline quality of the films was examined by SEM and preferential defect etching. Secco etching was applied to reveal the extended defects (dislocations and stacking faults) in the epitaxially grown layers. Figure 4.7 presents the SEM image of a Secco-etched surface of an epitaxially grown Si film on Si(100) wafer and it is representative for the whole temperature range investigated.

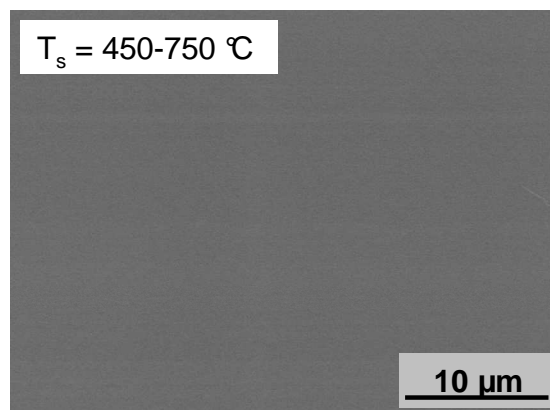


Figure 4.7 SEM image of a Secco-etched surface of an epitaxially grown Si film on Si(100) wafer at $T_s = 450\text{-}700 \text{ }^\circ\text{C}$. Epitaxial films exhibit no etch pits for the whole temperature range investigated.

The epitaxial Si films grown on Si(100) wafers exhibit no characteristic etch pits for the whole temperature range, indicating the high quality epitaxial growth on these substrates. Figure 4.8 shows the SEM images of Secco-etched surfaces of the epitaxially grown Si films on Si(111) wafers for the same substrate temperature range. The typical etch pits for stacking faults (triangles) and dislocations (circles) of epitaxial growth on Si(111) are observed. The strong influence of T_s on the etch pit density is clearly visible. The etch pit density decreases dramatically by increasing T_s , which corresponds to an enhancement of the structural quality of the epitaxial films on Si(111) wafers by increasing substrate temperature. At $T_s \leq 550$ °C, the etch pit density is above 10^8 cm⁻², indicating that not enough thermal energy has been supplied for high quality epitaxial

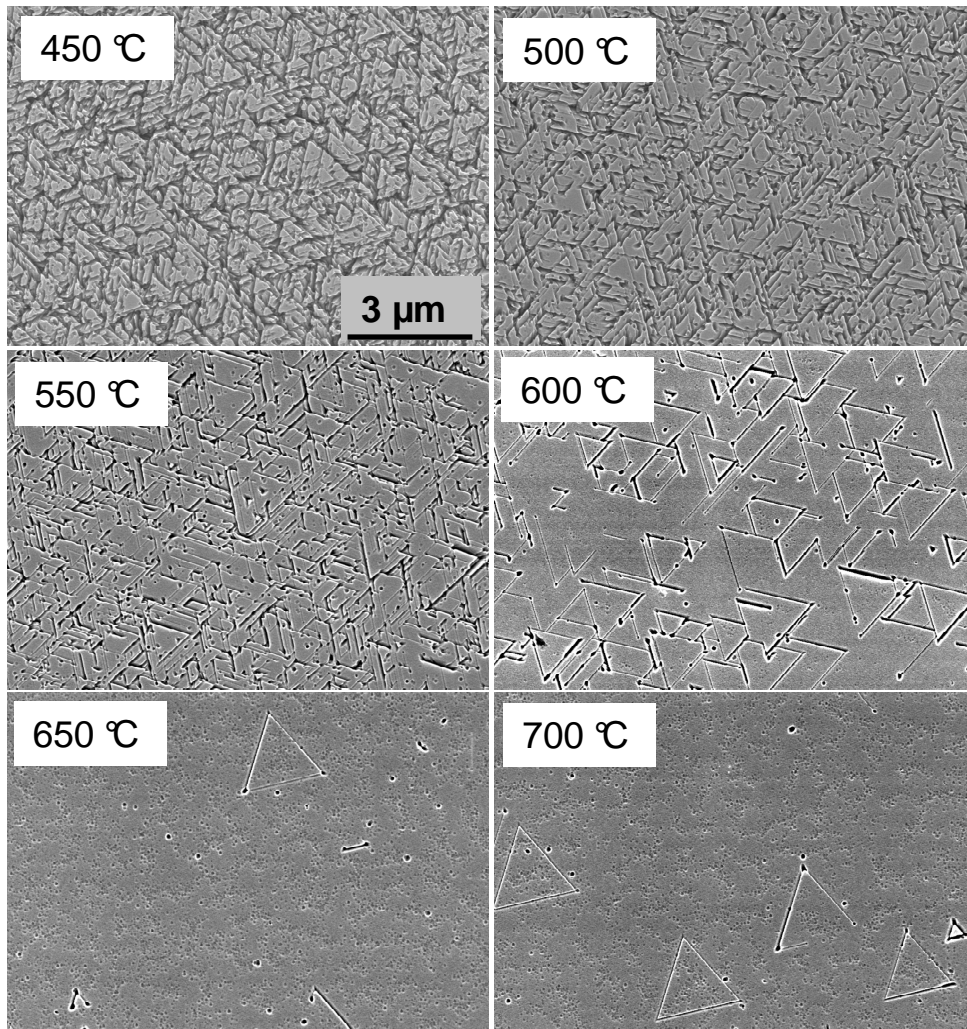


Figure 4.8 SEM images of Secco-etched surfaces of epitaxially grown Si films on Si(111) wafers at $T_s = 450$ - 700 °C. Typical etch pits are observed (stacking faults, dislocations). Increasing T_s , causes the etch pit density to decrease.

growth. However, the etch pit density decreases dramatically for $T_s \geq 600$ °C. It is about 1×10^8 cm⁻² for $T_s = 600$ °C and decreases to 4×10^6 cm⁻² for $T_s = 650$ °C. For $T_s = 700$ °C, the etch pit density slightly increases to 5×10^6 cm⁻². The latter increase is probably induced by additional outgassing of the system parts at higher temperatures leading to a higher contamination in the epitaxial films. In addition, the surface of the epitaxial films grown at $T_s = 650$ and 700 °C reveal presence of surface roughening. In conclusion, the lowest etch pit density for the epitaxial Si films grown on Si(111) wafers is observed at about 650 °C. These results reveal that epitaxial growth-quality (extended defect density) depends strongly on the substrate temperature as well as the underlying crystallographic orientation.

To gain a deeper insight in the structural film properties, Raman spectra have been recorded for the epitaxial Si layers grown on Si(100) and Si(111) wafers for the substrate temperature range of 450 - 700 °C. In Figure 4.9 the spectra for the epitaxial Si layers grown on Si (100) wafers together with a c-Si wafer (reference) are plotted. The measured intensities are normalized to 1. The position of the dominant Raman peak for c-Si, the LO-TO phonon mode, is at around 520 cm⁻¹. The spectra of the films exhibit the same peak position that is characteristic for c-Si. This confirms the epitaxial film growth on Si(100) wafers for the whole temperature range investigated in this work. Similar Raman spectra were observed for the epitaxial films grown on Si(111) wafers

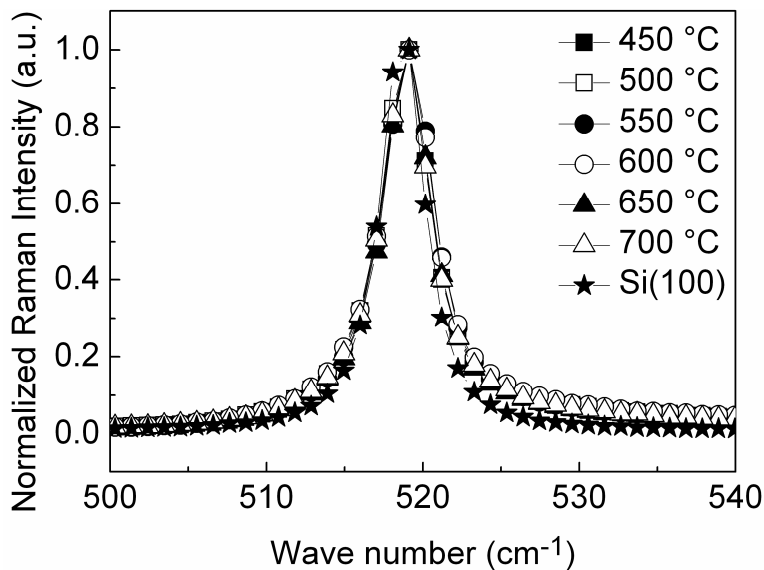


Figure 4.9 Normalized Raman intensity versus wave number for the epitaxial Si films on Si(100) wafers at $T_s = 450$ - 700 °C and a bare c-Si wafer as a reference.

(not shown here). In addition, the Raman spectra of the epitaxial films on Si(100) wafers compared to bare c-Si wafer exhibit a slightly asymmetric curve towards high wave numbers. The asymmetric broadening of the LO-TO phonon lines of the epitaxial films on Si(100) are caused by the highly boron doped underlying Si(100) wafers.

To determine the Full Width at Half Maximum (FWHM) of the phonon line a Lorentzian was used as fitting procedure. The spectral width is interpreted in terms of phonon confinement, and so it is a measure for the density of defects in the films, as these determine the unperturbed phonon propagation. The FWHM of the Raman spectra is plotted as a function of T_s for epitaxial Si films on Si(100) wafers (Figure 4.10.a) and for epitaxial Si films on Si(111) wafers (Figure 4.10.b). The error bars were obtained by several measurements of the same sample for a given T_s . The FWHM values for epitaxial Si films on Si(100) wafers are found between 3.7 and 3.9 cm^{-1} and are independent of T_s . In comparison, the FWHM value of a bare c-Si wafer is around 3.0 cm^{-1} , which is still lower than the obtained values for the epitaxial films on Si(100). Even though no extended defects could be observed on epitaxial films grown on Si(100) wafers after Secco etching in the SEM images, it can be concluded from the Raman measurements that the structural properties of the epitaxial films are not perfect. In comparison, for epitaxial films on Si(111) wafers FWHM values decrease towards higher T_s before they slightly increase at $T_s=700 \text{ }^\circ\text{C}$. This result is in good agreement with decreasing etch pit density observed for higher T_s from SEM images (Figure 4.8). In other words, by increasing the substrate temperature the density of extended defects decreases and the structural quality of the films are improved. Comparing the FWHM of epitaxial Si films on Si(100) and on Si(111) at for example $600 \text{ }^\circ\text{C}$, we obtain a value of about 3.9 cm^{-1} for both structures. Despite the difference of extended defect density on both structures, the comparison of the FWHM indicates that the structural quality is not only disturbed by extended defects but probably also by point defects which can not be revealed by defect etching.

Electrical Properties

The free carrier concentration and the mobility of majority carriers determined by Hall-effect measurements as a function of T_s in the p-type Si films grown on Si(100) wafers at $T_s= 450\text{-}700 \text{ }^\circ\text{C}$ are depicted in Figure 4.11.a and b, respectively. The effusion

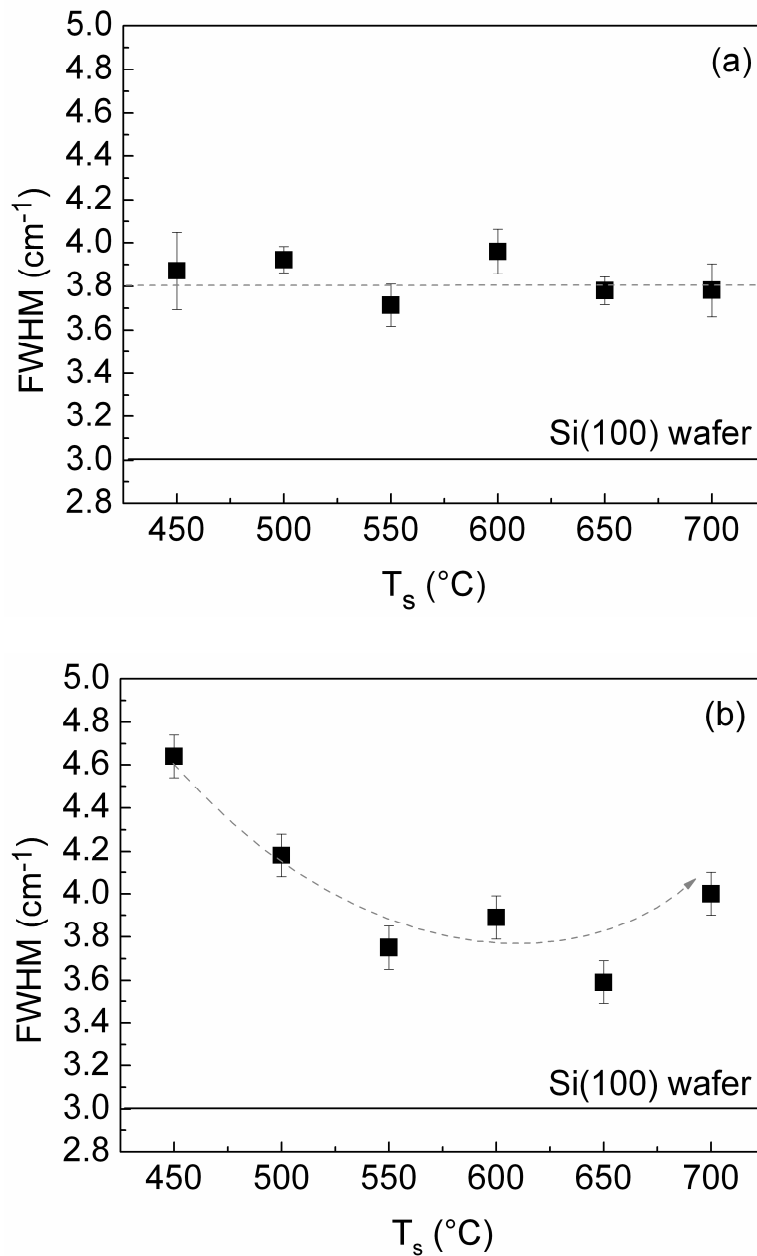


Figure 4.10 FWHM of the Raman spectra for the epitaxial Si films a) on Si(100) wafers b) on Si(111) wafers grown at $T_s = 450\text{-}700$ $^{\circ}\text{C}$. For comparison FWHM of a bare c-Si wafer is drawn at 3.0 cm^{-1} as a solid line. Dashed curves are only guides for the eye.

cell temperature was kept constant at 1640 $^{\circ}\text{C}$ to achieve a constant doping level in the epitaxial films. The average deposition rate was about $60\text{-}70$ nm/min .

As can be seen from Figure 4.11.a the free carrier concentration is between 6 to $8 \times 10^{16} \text{ cm}^{-3}$ at $T_s \geq 600$ $^{\circ}\text{C}$. This value is higher compared to the previously mentioned doping level of $3\text{-}4 \times 10^{16} \text{ cm}^{-3}$ due to the lower Si deposition rate. Below $T_s = 600$ $^{\circ}\text{C}$, the free carrier concentration drops down to $3 \times 10^{16} \text{ cm}^{-3}$. Knowing that at $T_s = 600$ $^{\circ}\text{C}$ the

doping efficiency is almost unity, lower free carrier density at lower T_s can be attributed to a lower doping efficiency. The fluctuations of the free carrier concentration at higher substrate temperatures $T_s \geq 600$ °C can be attributed to slight variations of the deposition rate. As a result, free carrier concentration increases with increasing T_s and for $T_s \geq 600$ °C full activation of the dopant atoms has been obtained.

The majority carrier mobility of these epitaxial films is plotted as a function of

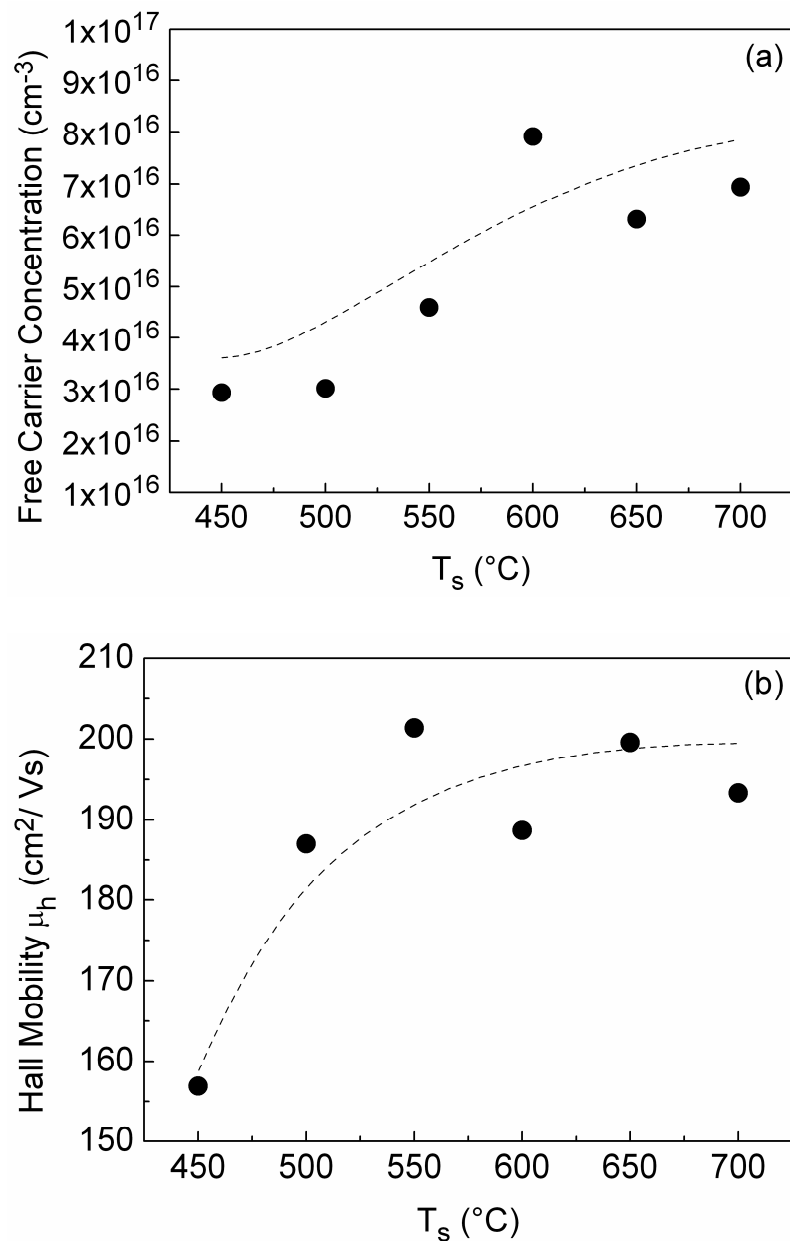


Figure 4.11 (a) Free carrier concentration and (b) Hall mobility of holes as a function of T_s in the range of 450-700 °C measured in the epitaxial Si films grown on Si(100) wafers. Dashed curves are guides for the eye.

T_s in Figure 4.11.b. The mobility of holes is below $160 \text{ cm}^2/\text{Vs}$ for the low temperature regime ($T_s = 450 \text{ }^\circ\text{C}$). Probably defects created at low substrate temperatures are responsible for the low mobility of majority carriers. For $T_s \geq 550 \text{ }^\circ\text{C}$, the mobility increases to about $200 \text{ cm}^2/\text{Vs}$ and stays constant for the higher temperature regime. The small fluctuations of mobility are attributed to the changes in the deposition rate and so in the free carrier concentration. As it was mentioned before, even at higher substrate temperatures the value of the mobility is still less compared to a theoretical value of $300 \text{ cm}^2/\text{Vs}$ of a perfect c-Si within the dopant impurity concentration range of the samples and indicates scattering by defect centers present in the films. Despite the high quality of the epitaxial films grown on Si(100) wafers revealed by defect etching, electrical characterization of the layers shows that substrate temperature is a critical deposition parameter that can influence the defect generation within the epitaxial films.

For a better understanding of the carrier scattering mechanism by the defect centers, hall mobility of holes have been measured at different temperatures in the range of 20-300 K for the films deposited at different substrate temperatures on Si(100) wafers. The results are plotted in Figure 4.12. The mobility of holes first starts to increase towards higher measurement temperatures and then gradually decreases when the temperature is further increased towards room temperature. At lower measurement

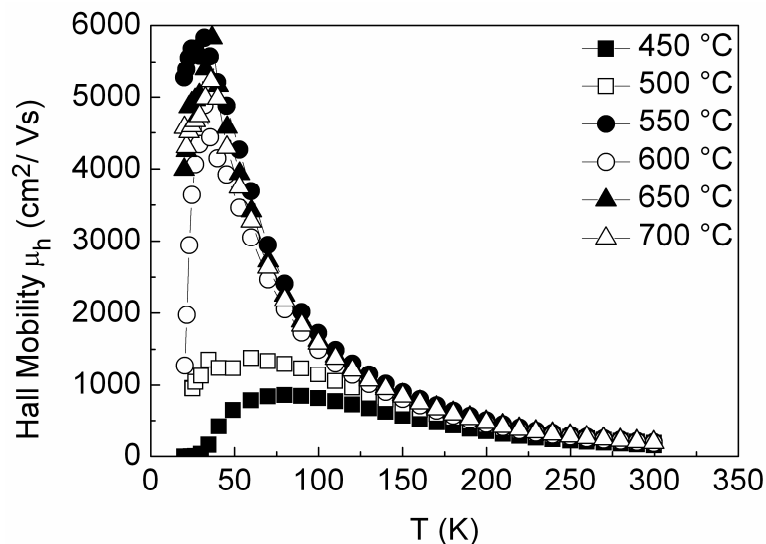


Figure 4.12 Hall mobility of holes versus measurement temperature (20-300 K) of the epitaxial Si films grown on Si(100) wafers ($T_s = 450\text{-}700 \text{ }^\circ\text{C}$).

temperatures a clear difference in the peak value of the mobility for epitaxial layers grown at 450 and 500 °C compared to higher substrate temperatures is observed. It is clearly seen that the mobility of holes for $T_s = 450$ and 500 °C is much lower compared to $T_s \geq 550$ °C. In general, the mobility is related directly to the scattering time, which in turn is determined by the various scattering mechanisms. The two most important mechanisms are phonon scattering and impurity scattering.

Phonon scattering results from thermal vibrations of the lattice atoms at any temperature above absolute zero. These vibrations disturb the lattice periodic potential and allow energy to be transferred between the carriers and the lattice. Since lattice vibration increases with increasing temperature, lattice scattering becomes dominant at high temperatures, therefore the mobility decreases with increasing temperature. The mobility due to acoustical phonon scattering decreases with temperature as $T^{-3/2}$. In Figure 4.12 the decrease of mobility due to phonon scattering is observed towards higher measurement temperatures for the whole substrate temperature range of 450-700 °C. The same graph is plotted in a logarithmic scale in Figure 4.13 in order to see possible differences for different samples. The solid line represents the reference $\mu \sim 1/T^{3/2}$ behavior. As it can be seen the slope of the investigated epitaxial films (dashed

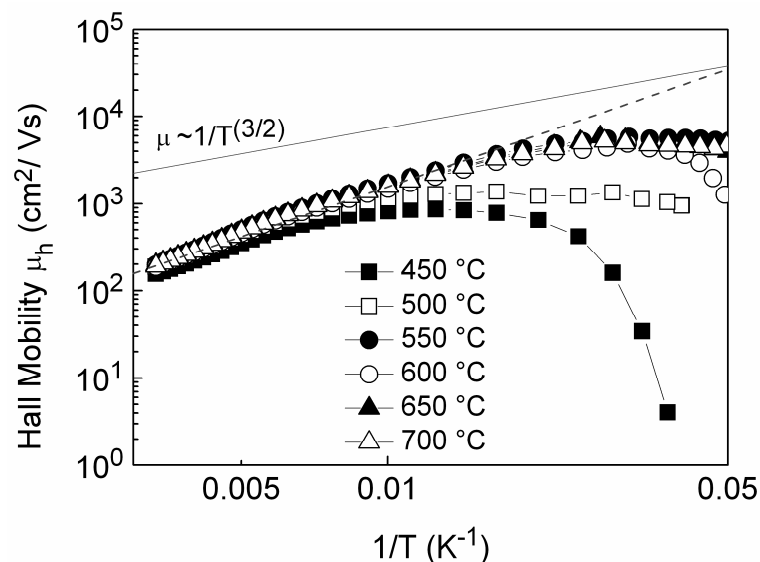


Figure 4.13 Hall mobility of holes (logarithmic scale) versus inverse measurement temperature (logarithmic scale) of the epitaxial Si films grown on Si(100) wafers ($T_s = 450$ -700 °C). The solid line represents the reference $\mu \sim T^{-3/2}$ behavior. Dashed line represents the slope of the measurements on epitaxial Si films.

line) is slightly deflected from $T^{-3/2}$ line. That means another scattering center is present in addition to lattice scattering, e.g. scattering via defect centers. At lower measurement temperatures, impurity scattering becomes dominant. Ionized impurity scattering results when a charge carrier travels near an ionized dopant impurity. The charge carrier path is deflected due to Coulomb force interaction. The probability of impurity scattering depends on the total concentration of ionized impurities, that is the sum of the concentration of ionized negatively and positively charged ions.

However, unlike lattice scattering, impurity scattering becomes less significant at higher temperatures. Because the carriers move faster at higher temperature, they remain near the impurity center for a shorter time and are therefore less effectively scattered. As a conclusion, the mobility of holes in the epitaxial films grown on Si(100) wafers is controlled by the combination of different scattering mechanisms: lattice scattering, impurity scattering and scattering via defect centers.

Finally, the EBIC collection efficiency has been recorded for the epitaxial films grown on Si(111) wafers for $T_s = 450-700$ °C (Figure 4.14). The collection efficiency of the epitaxial films increases with increasing T_s . This result is again in good agreement with decreasing etch pit density observed for these films for increasing T_s (Figure 4.8) and confirms that the extended defects that are observed for epitaxial films on Si(111) wafers are electrically active recombination centers. For $T_s = 700$ °C, a slight decrease

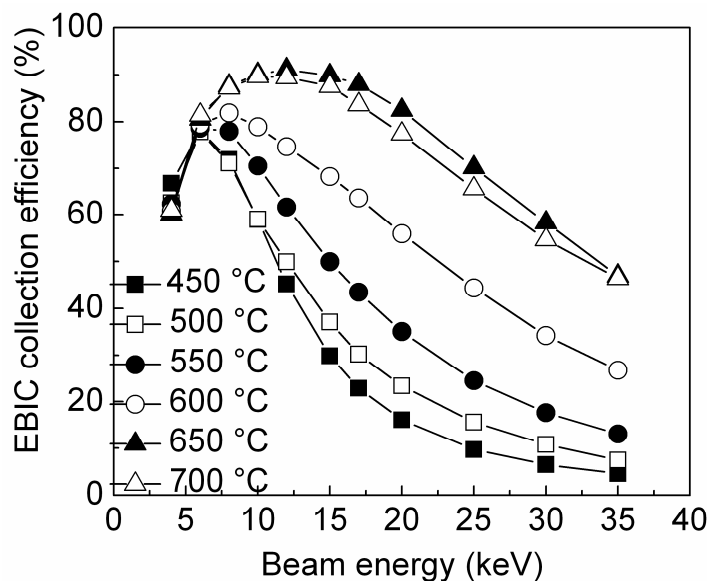


Figure 4.14 EBIC collection efficiency versus the beam energy for the epitaxial Si films grown on Si(111) wafers at $T_s = 450-700$ °C.

in the collection efficiency is observed compared to that of $T_s = 650$ °C which is caused by the slight increase that is observed in the etch pit density.

As a summary, epitaxial growth quality depends strongly on the substrate temperature as well as the underlying crystallographic orientation. Best epitaxial growth is obtained for epitaxial films grown on Si(100) wafers for $T_s \geq 600$ °C.

4.4 Influence of Si Deposition Rate

Structural Properties

A deposition rate as high as possible is certainly desired in the contest of a commercial application. Moreover, a high deposition rate can reduce the amount of contaminations built into the films during growth. The influence of the deposition rate on the extended defect density for the epitaxially grown films on Si(111) wafers is presented in Figure 4.15. Since epitaxial films on Si(100) wafers reveal no extended defects within the detection limits of SEM, the extended defects for the epitaxial films grown on Si(111) wafers were investigated only. Investigations of the influence of the substrate temperature already revealed that $T_s \geq 600$ °C should be preferred for a high quality epitaxial growth. Considering the seed layer approach which is based on glass substrates, the substrate temperature is limited to about 600 °C. Therefore, the substrate temperature was kept constant at 600 °C.

The deposition rate (r_{Si}) was varied from 40 to 475 nm/min by adjusting the emission current of the e-gun. The effusion cell temperature was also readjusted according to the change in Si deposition rate to be able to keep the doping level of the epitaxial films constant. SEM images of the Secco etched surfaces of epitaxial films reveal that the density of extended defects increased with increasing r_{Si} . The lowest etch pit density of 1.7×10^7 cm⁻² was obtained for $r_{Si} = 40$ nm/min. Whereas, the etch pit density is $\geq 10^8$ cm⁻² for $r_{Si} \geq 185$ nm/min. One reason of the increased extended defect density at higher deposition rates can be the shorter time given for the adatoms to find their correct place in the lattice.

On the other hand, at higher Si deposition rates the total pressure during the deposition increases. This is caused by the more effective outgassing of the system parts close to e-gun when a higher emission current has been applied in order to obtain higher deposition rates. This outgassing causes an increase in the background level of the

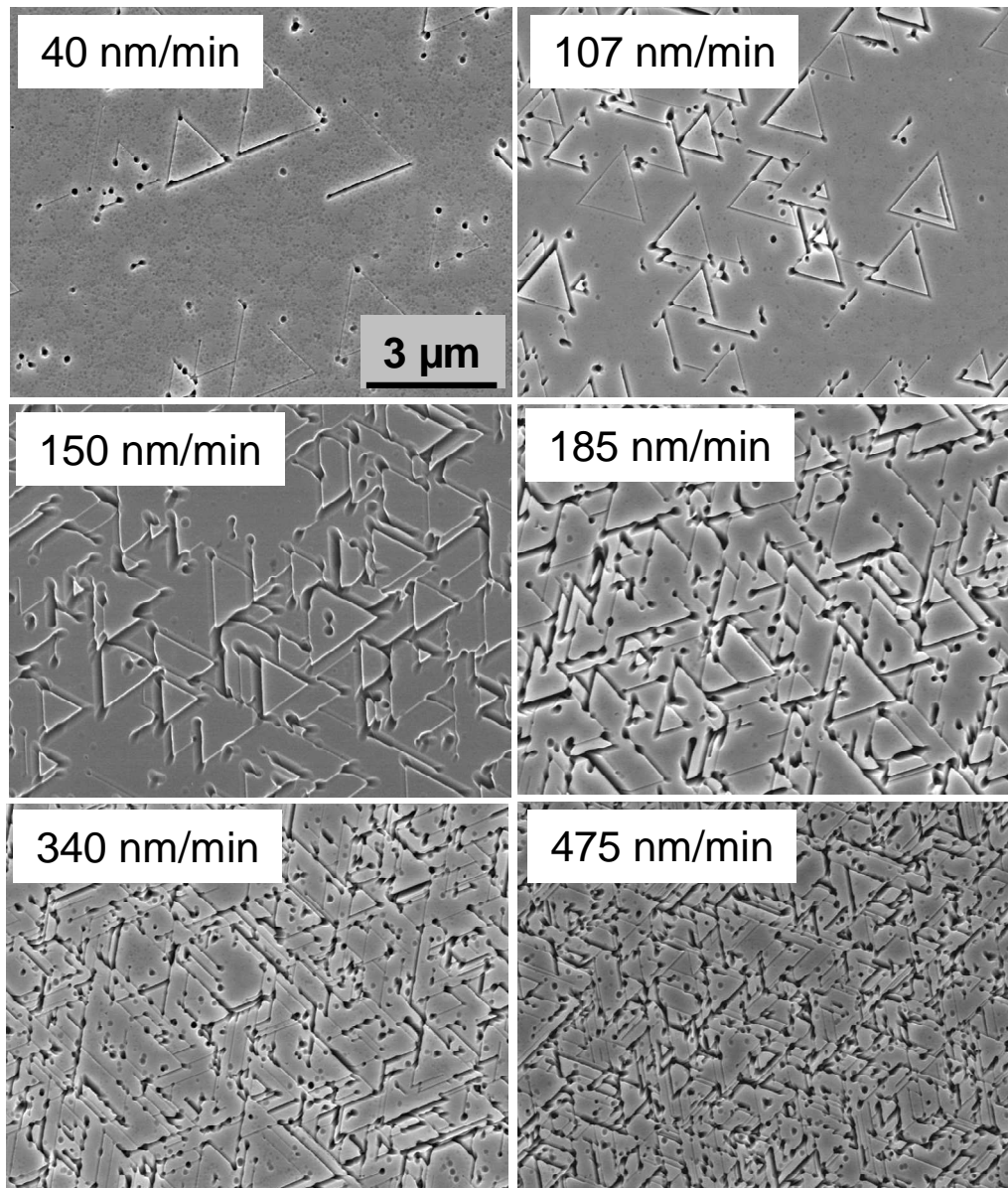


Figure 4.15 SEM images of Secco-etched Si films grown on Si(111) wafers at $T_s = 600$ °C with $r_{Si} = 40$ -475 nm/min.

contaminants and is responsible for the generation of additional extended defects at high deposition rates.

Electrical Properties

The majority carrier concentration of the epitaxial films on Si(100) substrates was determined by Hall-effect measurements. It was found that the free carrier concentration in the layers varies between 3.6×10^{16} and 9.6×10^{16} cm^{-3} for $r_{Si} = 40$ -475

nm/min (Figure 4.16.a). The difference in the doping level is mainly caused by the fluctuations of the deposition rate.

The corresponding Hall mobility of majority carriers is plotted in Figure 4.16.b. An average mobility of about $195 \text{ cm}^2/\text{Vs}$ is obtained. This level of mobility is in agreement with the mobility level obtained from the investigations of the substrate temperature. The fluctuations of the mobility are again caused by the fluctuations of the free carrier concentration.

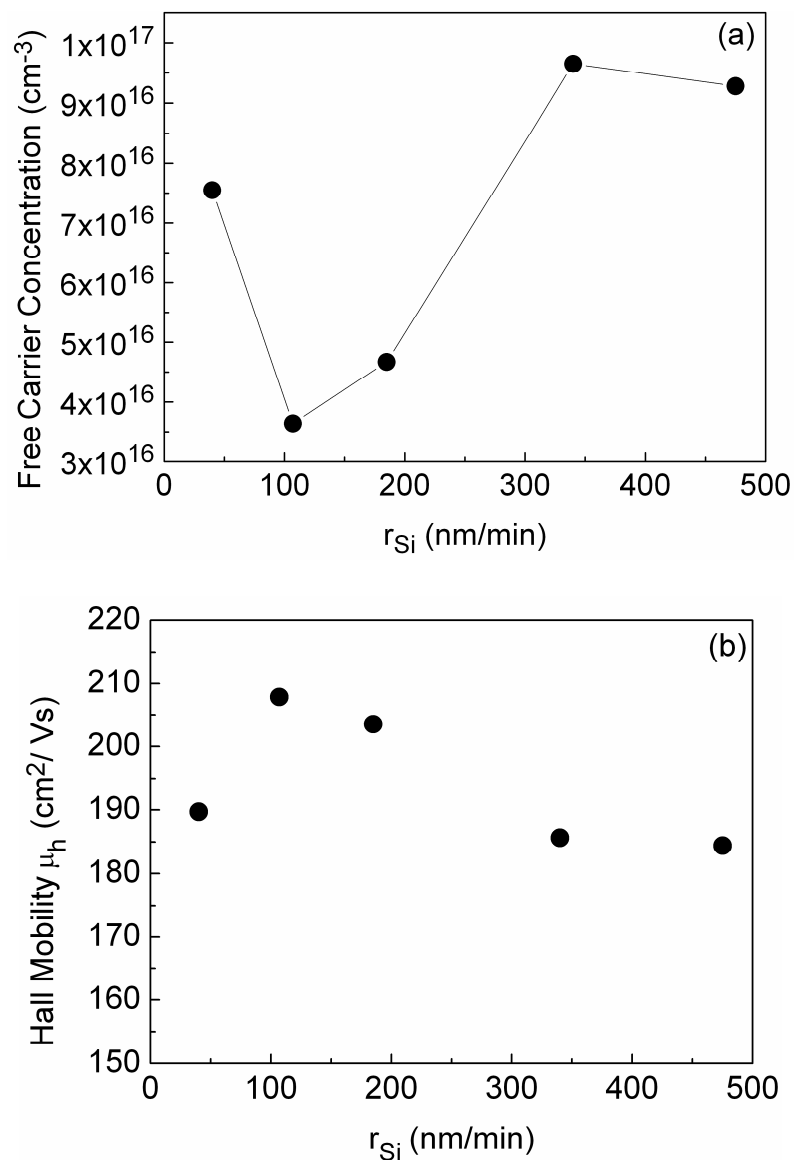


Figure 4.16 (a) Free carrier concentration and (b) Hall mobility of holes as a function of r_{Si} in the range of 40-475 nm/min measured in the epitaxial Si films grown on Si(100) wafers at $T_s = 600 \text{ }^\circ\text{C}$.

4.5 Influence of Base Pressure

Structural Properties

It is well known from Si MBE that the base pressure of a deposition system is of crucial importance in terms of incorporation of contaminants inside the growing films

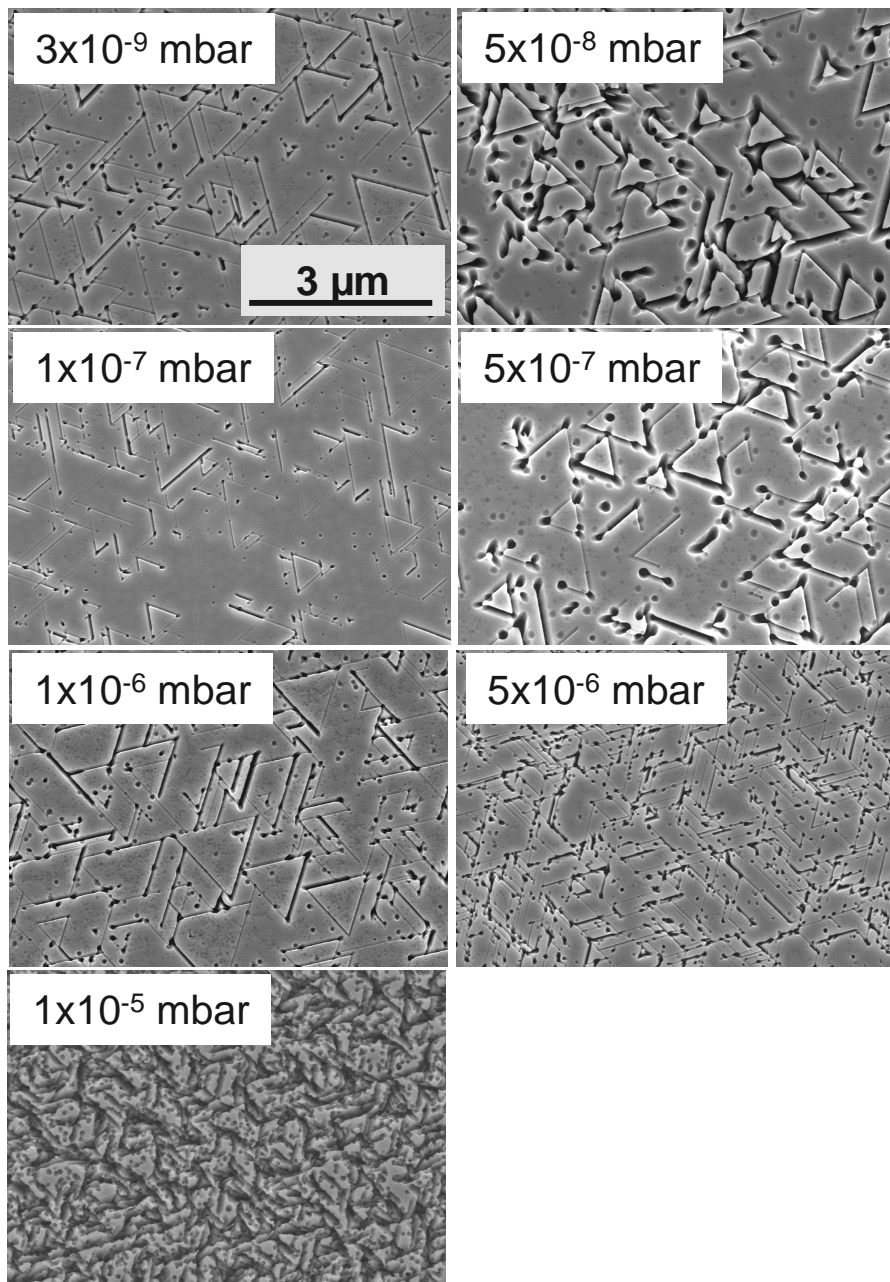


Figure 4.17 SEM images of Secco-etched Si films grown on Si(111) wafers at $T_s = 600^\circ\text{C}$ for $p = 3 \times 10^{-9} - 1 \times 10^{-5}$ mbar.

and hence for the corresponding defect formation. The purpose of this investigation is to find the limits of the base pressure of such an e-beam system before it starts to influence the structural and electrical properties of the growing films. In order to vary the base pressure of the e-beam system, laboratory air was introduced inside the deposition chamber through a needle valve in a controlled way. The variation of the residual gases were observed by the use of the mass spectra. During these experiments, the main increase of the pressure is caused by the partial pressures of N₂ and O₂. Individual influences of the N₂, O₂ and H₂O partial pressures on the solar cell characteristics of epitaxially grown Si films were also investigated (see Annex I).

By introducing air, the base pressure of the system was varied between $p = 3 \times 10^{-9}$ (reference without gas inlet) and 1×10^{-5} mbar. After applying Secco etching typical triangular stacking faults for epitaxial films grown on Si(111) wafers were revealed (Figure 4.17). An increase of the etch pit density is observed towards higher base pressures. The highest etch pit density is observed for $p = 1 \times 10^{-5}$ mbar. At this pressure epitaxial growth is strongly disturbed. Whereas, a slight increase in the etch pit density can be already detected at $p = 5 \times 10^{-6}$ mbar. Different sized etch pits can be detected in the SEM images. This means the increase in the base pressure not only causes to an initial wafer surface contamination but also contamination and defect formation within the epitaxial films. Raman measurements (not shown) performed for epitaxial layers on Si(100) and Si(111) substrates reveal no clear dependence for increasing base pressure. Only an increase in FWHM for epitaxial films grown at $p = 1 \times 10^{-5}$ mbar is observed.

Electrical Properties

Figure 4.18 illustrates the majority carrier mobility for the epitaxial films grown on Si(100) wafers at $T_s = 600$ °C for base pressures between 3×10^{-9} and 1×10^{-5} mbar. Hole concentration of the epitaxial films grown within $p = 3 \times 10^{-9}$ mbar and 5×10^{-6} mbar only slightly vary between $3-5 \times 10^{16}$ cm⁻³. The carrier type of the epitaxial films grown at $p = 1 \times 10^{-5}$ mbar changes from p-type to n-type. This film shows an electron density of about 7×10^{13} cm⁻³. For such high base pressure experiments, mass spectra measurements reveal a great increase for the nitrogen and oxygen residual background levels during the deposition. Especially O₂ is known to behave as a donor once

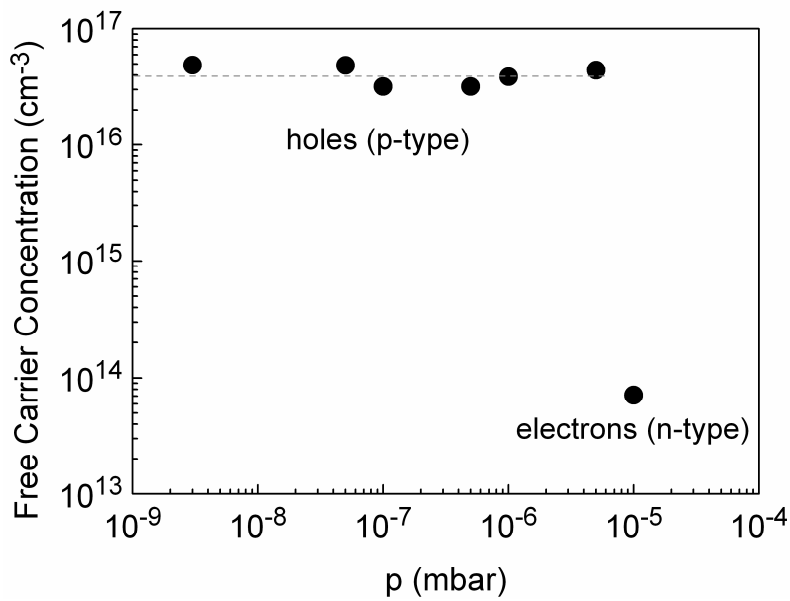


Figure 4.18 Free carrier concentration as a function of base pressure in the range of 3×10^{-9} - 1×10^{-5} mbar measured in the epitaxial Si films grown on Si(100) wafers ($T_s = 600$ °C).

incorporated and activated within such epitaxial films. Therefore, the change in the carrier type for $p = 1 \times 10^{-5}$ mbar is expected to be caused by the high level of O_2 background. O_2 compensates boron doping within the epitaxial films and changes the carrier type to n-type. The corresponding mobility of the majority carriers is plotted in

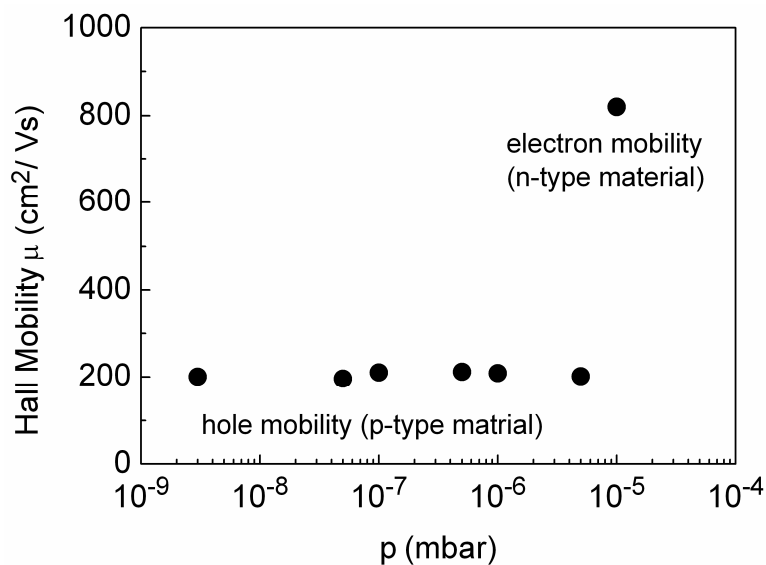


Figure 4.19 Hall mobility (μ) of carriers as a function of base pressure (p) for the epitaxial Si films grown on Si(100) wafers ($T_s = 600$ °C).

Figure 4.19. A hole mobility of about 200-210 cm^2/Vs has been obtained for $p = 3 \times 10^{-9}$ - 5×10^{-6} mbar. As the carrier type changes from p-type to n-type for $p = 1 \times 10^{-5}$ mbar, an electron mobility of about 820 cm^2/Vs has been detected.

4.6 Influence of Substrate Bias

Structural Properties

The influence of the ionized Si atoms ionized by the use of a post-ionization stage has been partly investigated by previous studies [52,57]. It was assumed that

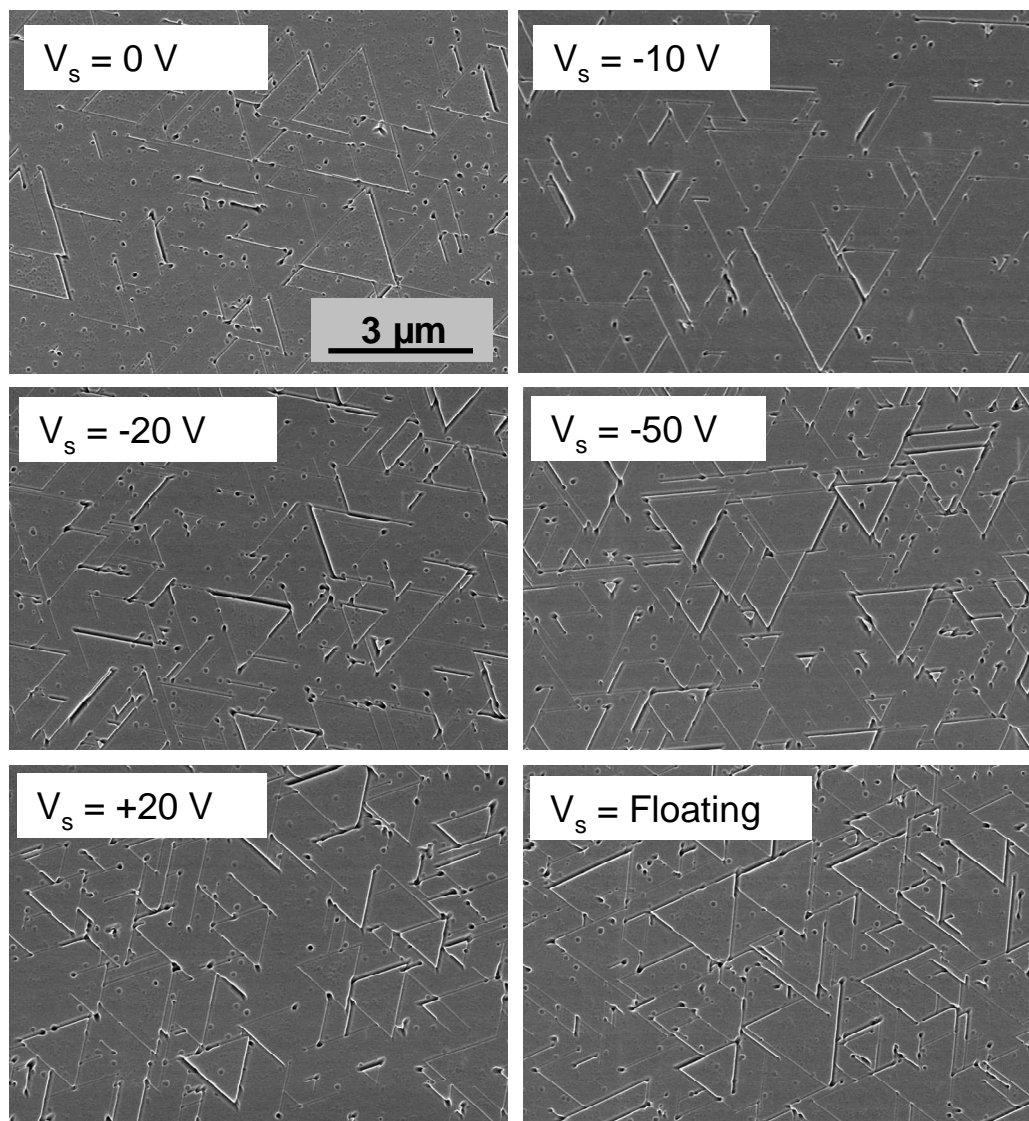


Figure 4.20 SEM images of Secco-etched Si films grown on Si(111) wafers at $T_s = 600$ °C for 0, Floating, -10, -20, -50, +20 V.

accelerated Si ions may supply an additional energy to the growth surface and thereby enhance the quality of the low temperature epitaxy. Although in this work a post-ionization stage was not used, we assumed that the e-gun itself may produce some ionized Si atoms. In this investigation these Si ions have been accelerated by applying either a positive or a negative substrate bias and the corresponding substrate current was measured. Indeed, a variation of the substrate current according to the applied bias polarity and magnitude could be detected. When the substrate is grounded ($V_s = 0$ V) a substrate current of about $10 \mu\text{A}$ is detected. When negative substrate bias values were applied, the substrate current value increases towards the negative values and substrate current values of -20 to $-30 \mu\text{A}$ could be recorded. This proves the presence of available ions that are accelerating towards the substrate under the influence of the applied substrate bias. On the other hand, application of a positive substrate bias should result in the acceleration of electrons towards the substrate. Applying a positive bias to the substrate, substrate current values in the range of 600 - $800 \mu\text{A}$ could be detected.

The purpose of this investigation is to illustrate a possible influence of the acceleration of Si ions or electrons on the structural and the electrical properties of the epitaxially grown Si films. Therefore Si films were grown under different substrate bias conditions and were subsequently characterized by defect etching, SEM and Hall-effect measurements.

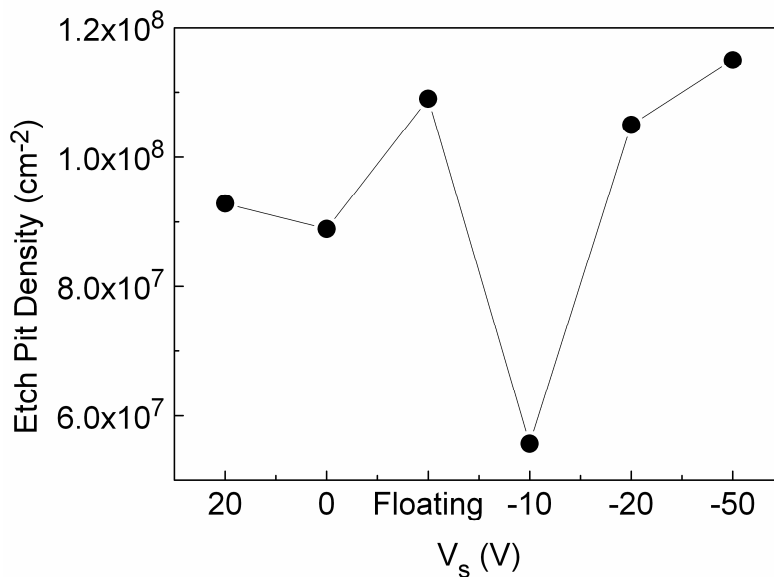


Figure 4.21 The etch pit density determined from Figure 4.20 as a function of applied bias (V_s).

The SEM images of the Secco-etched epitaxial films on Si(111) wafers and the corresponding etch pit density as a function of the applied substrate bias are shown in Figure 4.20 and 4.21, respectively. A variation in the etch pit density was detected. At ground potential ($V_s = 0V$) an etch pit density of about $9 \times 10^7 \text{ cm}^{-2}$ was obtained. As the substrate bias was floating, the etch pit density increases to about $1.1 \times 10^8 \text{ cm}^{-2}$. However, when $V_s = -10 \text{ V}$ was applied the etch pit density decreases almost half an order of magnitude to about $5.6 \times 10^7 \text{ cm}^{-2}$. As the substrate bias was increased towards more negative values the etch pit density starts to increase again. The result at $V_s = -10 \text{ V}$ indicates that the acceleration of Si ions towards substrate surface could be beneficial when the applied voltage is on the one hand high enough to provide energy to the growing film and does on the other hand not deteriorate the growing film by ion bombardment. The optimum value of -10 V obtained from this investigation is lower than the -20 V acceleration voltage value reported in the literature where a post-ionization stage has been used to create intentionally Si ions [52].

Electrical Properties

The free carrier concentration of the epitaxial Si films grown on Si(100) wafers

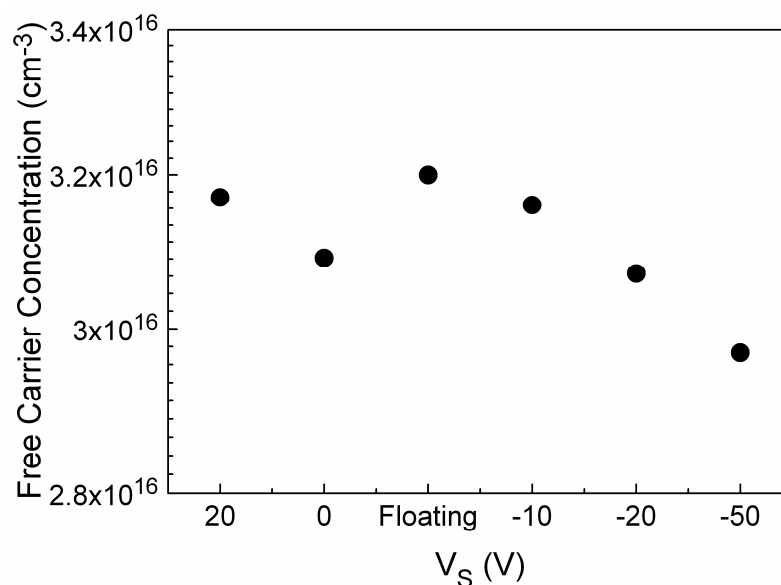


Figure 4.22 Free carrier concentration as a function of the applied bias $V_s = 0$, Floating, -10 , -20 , -50 , $+20 \text{ V}$ measured in the epitaxial Si films grown on Si(100) wafers at $T_s = 600 \text{ }^\circ\text{C}$.

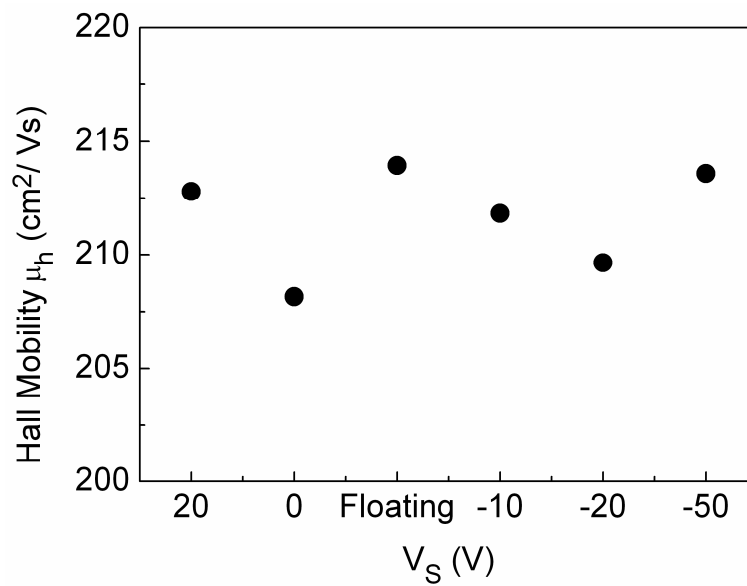


Figure 4.23 Hall mobility of holes as a function of the applied bias $V_s = 0$, Floating, -10, -20, -50, +20 V measured in the epitaxial Si films grown on Si(100) wafers at $T_s = 600$ °C.

versus applied substrate bias is plotted in Figure 4.22. It is clearly seen that for this investigation the doping level of the epitaxial films could be kept almost constant. The films exhibit a doping level of about $3\text{-}3.2 \times 10^{16} \text{ cm}^{-3}$. The corresponding mobility of majority carriers is illustrated in Figure 4.23. Mobility values of about $210 \text{ cm}^2/\text{Vs}$ could be achieved. This level of hole mobility is slightly higher than in the previous investigations. This result shows that these films contain less scattering centers to disturb the carrier mobility, which in turn corresponds to an enhanced epitaxial quality of the Si films.

4.7 Summary and Conclusions

In this chapter, the influence of the deposition parameters (substrate temperature, Si deposition rate, base pressure and substrate bias) were investigated to characterize and control the epitaxial growth of Si films on mono-Si wafers. Using a high rate e-beam evaporation, it was demonstrated that epitaxial film growth can be performed at low temperatures on mono-Si wafers with different orientations. The films exhibit the best structural and electrical quality if $T_s \geq 600$ °C. The epitaxial films grown on Si(100) wafers have shown no extended defects for the whole temperature range investigated $T_s = 450\text{-}700$ °C. However, the films grown on Si(111) wafers have shown

typical etch pits. The density of the extended defects decreases with increasing T_s . EBIC measurements exhibit that the collection efficiency is affected by the defects present in the epitaxial films.

Investigations of the electrical quality of the epitaxial films on Si(100) wafers revealed that incorporated dopants are fully activated for $T_s = 600$ °C. As a consequence no additional rapid thermal annealing is necessary. The mobility of the majority carriers is about $200 \text{ cm}^2/\text{Vs}$ for $T_s \geq 600$ °C. The high mobility values that were reached in the epitaxial layers on Si(100) wafers reveal information about the electrical quality of these films. For comparison, the mobility in bulk Si of $350 \text{ cm}^2/\text{Vs}$ (for the same doping range) is still higher than the value in epitaxial films. Defects present inside the films act as scattering centers and therefore they are responsible for lower mobility values obtained in the epitaxial films.

Increasing the substrate temperature, the structural and electrical properties of the epitaxial Si films are improved dramatically. Investigations of the deposition rate reveal that the extended defect density of epitaxial films grown on Si(111) wafers increase with increasing deposition rate. However, this result is mainly due to additional outgassing of the system parts at high rates and can be eliminated by conditioning the deposition prior to high rate experiments. Base pressure investigations were performed with intentional air inlet to vary the base pressure of the e-beam system. Increasing the base pressure of the system an increase in the extended defect density in the epitaxial films grown on Si(111) wafers starting at 5×10^{-6} mbar was observed. Hall-effect measurements reveal that epitaxial films grown until a base pressure of 5×10^{-6} mbar reveal a p-type conductivity ($3\text{-}5 \times 10^{16} \text{ cm}^{-3}$), whereas at $p = 1 \times 10^{-5}$ mbar the conductivity type changes to n-type ($7 \times 10^{13} \text{ cm}^{-3}$). Compensation of the p-type Boron doping of the epitaxial films prepared at high base pressures are probably due to the increased background level of the residual oxygen which can behave as a donor once it is incorporated into the structure (see Annex I). In order to prepare p-type epitaxial films with reasonable structural and electrical quality, the base pressure of the e-beam system should be kept below 1×10^{-5} mbar. Finally, substrate bias investigations reveal that Si ions generated by the e-gun can be accelerated towards the substrate in order to give the growth surface additional energy to promote low temperature epitaxy. The extended defect density decreases to $5.6 \times 10^7 \text{ cm}^{-2}$ for the epitaxial films grown on Si(111) wafers at $V_s = -10$ V. With excess substrate bias applied the extended defect density starts to increase again. An enhanced majority carrier mobility of about 212

cm^2/Vs was also detected for the epitaxial films grown on Si(111) wafers at $V_s = -10 \text{ V}$. This result shows that an acceleration of the Si ions towards the substrate surface during epitaxial growth may be beneficial for the structural and electrical quality of the growing films.

The main conclusions of the investigations performed on the epitaxially grown Si films on Si wafers which will be transferred and investigated for the glass substrates and solar cells in the following chapters are as follows :

- The crystalline quality of the epitaxially grown Si films strongly depends on the underlying crystallographic orientation. The best crystalline quality was obtained for epitaxially grown Si films on Si(100) wafers.
- However, the FWHM of the Raman spectra and a lower majority carrier mobility as compared to bulk Si indicate the presence of defects in these films.
- The substrate temperature has a strong impact on the epitaxial growth of Si films. Considering the structural and electrical properties of the epitaxial films, the substrate temperature (T_s) should be at least $600 \text{ }^\circ\text{C}$.

CHAPTER 5

Epitaxial Growth on Poly-Si Seed Layers on Glass

5.1 Introduction

Poly-Si is an attractive candidate for the realization of high efficiency thin film Si solar cells due to its potential to provide high material quality. One of the major challenges for low cost high quality poly-Si thin film production is the growth of poly-Si films on glass substrates at low temperatures by using fast and simple deposition processes. This thesis pursues an attractive approach for the preparation of large-grained poly-Si thin film solar cells on glass which is based on “seed layers”. In this approach, first poly-Si seed layers on glass have been prepared by Aluminum Induced Crystallization (AIC) of a-Si. These poly-Si seed layers have the characteristic of a large grain size (5-20 μm). However, due to too high Al doping of about 10^{20} cm^{-3} and rather low thicknesses of about 200 nm they can not be used as an absorber layer. Therefore, these poly-Si seed layers have been used as templates for the epitaxial growth of poly-Si absorber layers using high-rate e-beam evaporation. By this way, doping level and the thickness of the epitaxially grown poly-Si absorber layer can be optimized separately and independent from the poly-Si seed layers. In chapter 4, using c-Si wafers as “ideal seed layers” influence of the deposition parameters on the epitaxial growth quality of the absorber layers were presented. This chapter addresses the properties of poly-Si seed layers. Then these poly-Si seed layers prepared on glass are used as templates to study the influence of substrate temperature and underlying crystallographic orientation of the grains on the epitaxial growth of absorber layers. The origin and electrical activity of the defects in the epitaxially grown poly-Si absorber layers are studied. Moreover, the crystallographic quality of the epitaxial growth on poly-Si seed layers prepared by AIC and on seed layers prepared by laser crystallization (LC) are compared. The doping level of the epitaxial poly-Si absorber layers and out-diffusion processes that occur during growth are discussed. Finally, poly-Si films are also prepared based on depositing Si film directly on glass substrates and subsequently applying solid phase crystallization (SPC).

5.2 Properties of Poly-Si Seed Layers on Glass Prepared by AIC of a-Si

The experimental details of the poly-Si seed layer preparation have been described in chapter 3.1.2. The poly-Si seed layers have the characteristics of a large grain size and a preferential (100) orientation of the grain surface. A typical EBSD orientation map of the poly-Si seed layers and its corresponding pole figure is illustrated in Figure 5.1. Poly-Si seed layers prepared at 425 °C showed an average grain size of 7 μm and a maximum grain size of 18 μm . Large grains of the poly-Si seed layer have usually (100) grain orientation (red areas), whereas smaller grains usually have other crystallographic orientations (e.g. (111), blue areas). In total, the poly-Si seed layers used in this work exhibit a preferential (100) orientation of about 60% of the total area [83,84,85]. The preferential orientation is defined as the percentage of the poly-Si seed layer surface which is tilted by less than 20° with respect to the perfect (100) orientation. Poly-Si seed layers with preferential (100) orientation of up to 75% were obtained [86]. The preferential (100) orientation of the poly-Si seed layers is favorable for the subsequent low temperature homo-epitaxial growth of the absorber layers.

The poly-Si seed layers are heavily doped (p⁺-type) with Al. The aluminum

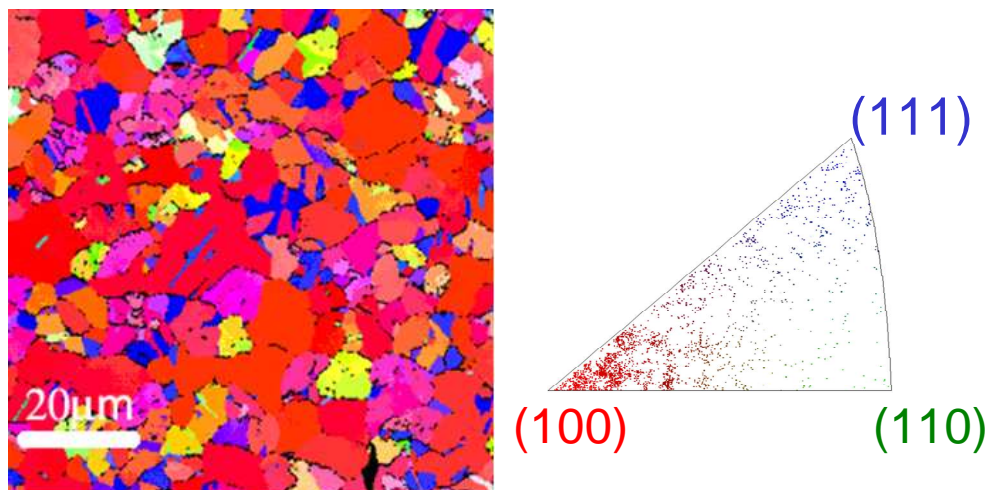


Figure 5.1 EBSD orientation map of the poly-Si seed layer prepared by AIC on glass substrates at $T = 425$ °C and the corresponding inverse pole figure [83].

concentration in the poly-Si seed layers determined by SIMS measurements yields to about $1\text{-}3 \times 10^{20} \text{ cm}^{-3}$. The value determined by SIMS gives however the total Al concentration, including ionized and unionized Al on both interstitial and substitutional lattice sites. Room temperature Hall-effect measurements on the Al doped poly-Si films prepared by AIC yield charge carrier concentrations of about $8 \times 10^{17} \text{ cm}^{-3}$ for films prepared at $425 \text{ }^\circ\text{C}$ on glass. The difference between the concentration of Al atoms and the free carrier concentration shows that most of the incorporated Al atoms are not ionized. However, the doping level of the poly-Si seed layer is still too high to use it as an active absorber layer in a solar cell configuration. Moreover, the material is highly defective, already indicated by the poor Al activation. Therefore, the p^+ -type poly-Si seed layers act as a Back Surface Field (BSF) in our solar cell structure. The majority carrier mobility determined by Hall-effect measurements results in about $40 \text{ cm}^2/\text{Vs}$ in poly-Si seed layers, compared to a value of $152 \text{ cm}^2/\text{Vs}$ in monocrystalline Si of the same doping level. The lower majority carrier mobility measured in poly-Si seed layers prepared by AIC compared to that in mono-crystalline Si have been explained in the literature by the potential barriers at the grain boundaries [87]. However, the appealing structural properties (large grain size, (100) preferential orientation) of the poly-Si seed layers prepared by AIC make them attractive for a use as a seed layer for the subsequent epitaxial growth of the absorber layers. Thereby, the structural properties of the absorber layers are determined by the poly-Si seed layer whereas the doping level of the absorber layer can be separately optimized. In the following sections, poly-Si seed layers prepared by AIC are epitaxially thickened by high-rate e-beam evaporation and the corresponding structural and electrical properties of the poly-Si epitaxial absorber layers are investigated.

5.3 Epitaxial Growth on Poly-Si Seed Layers

Using e-beam evaporation, about $2 \text{ }\mu\text{m}$ thick epitaxial poly-Si films were deposited on the poly-Si seed layers on glass. The intentional doping level of the absorber layer was adjusted to about $2\text{-}3 \times 10^{16} \text{ cm}^{-3}$. The following subsections discuss the influence of the substrate temperature, and underlying crystallographic orientation on the structural properties of epitaxially grown poly-Si absorber layers. In addition, the origin and

electrical activity of the defects present in the poly-Si epitaxial layers have also been investigated.

5.3.1 Influence of the Substrate Temperature

Achieving an epitaxial growth on poly-Si seed layers on glass is strongly dependent on the substrate temperature as it highly influences the defect formation during the growth. In chapter 4, the results of the influence of the substrate temperature on the

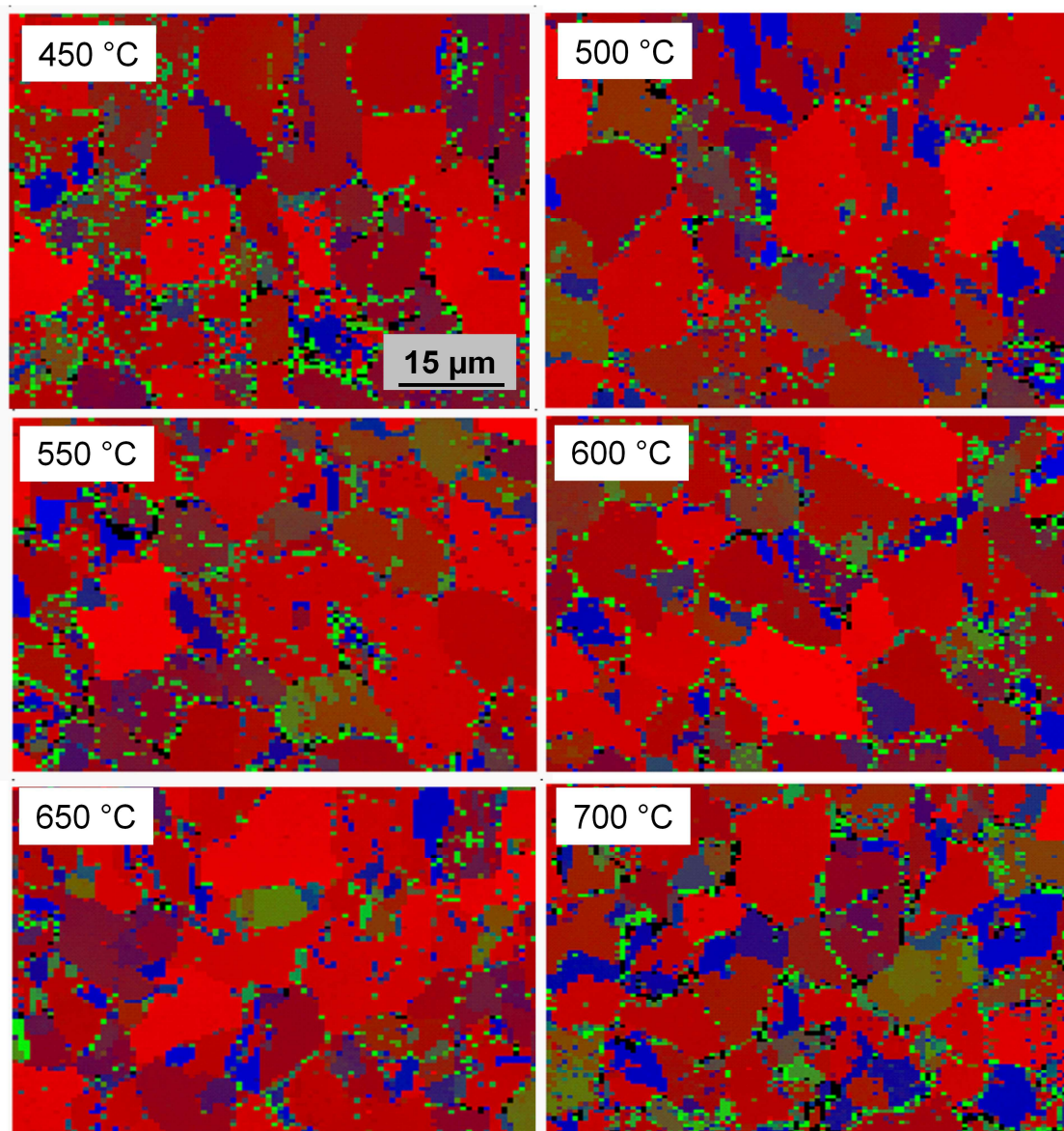


Figure 5.2 EBSD orientation map of the epitaxially grown Si films on the poly-Si seed layers on glass substrates deposited at $T_s = 450-700$ °C. (Color coding: red (100), blue (111), green (110))

epitaxially grown Si films on mono-Si wafers were presented. In the following work, poly-Si films are grown on poly-Si seed layers on glass at $T_s = 450\text{-}700\text{ }^\circ\text{C}$. Structural properties of the poly-Si films on poly-Si seed layers are examined using EBSD and Raman measurements. Investigations of EBSD measurements provide information about the crystallographic orientation of the near surface of the films.

Figure 5.2 exhibits the color-encoded orientation map of the poly-Si films grown on

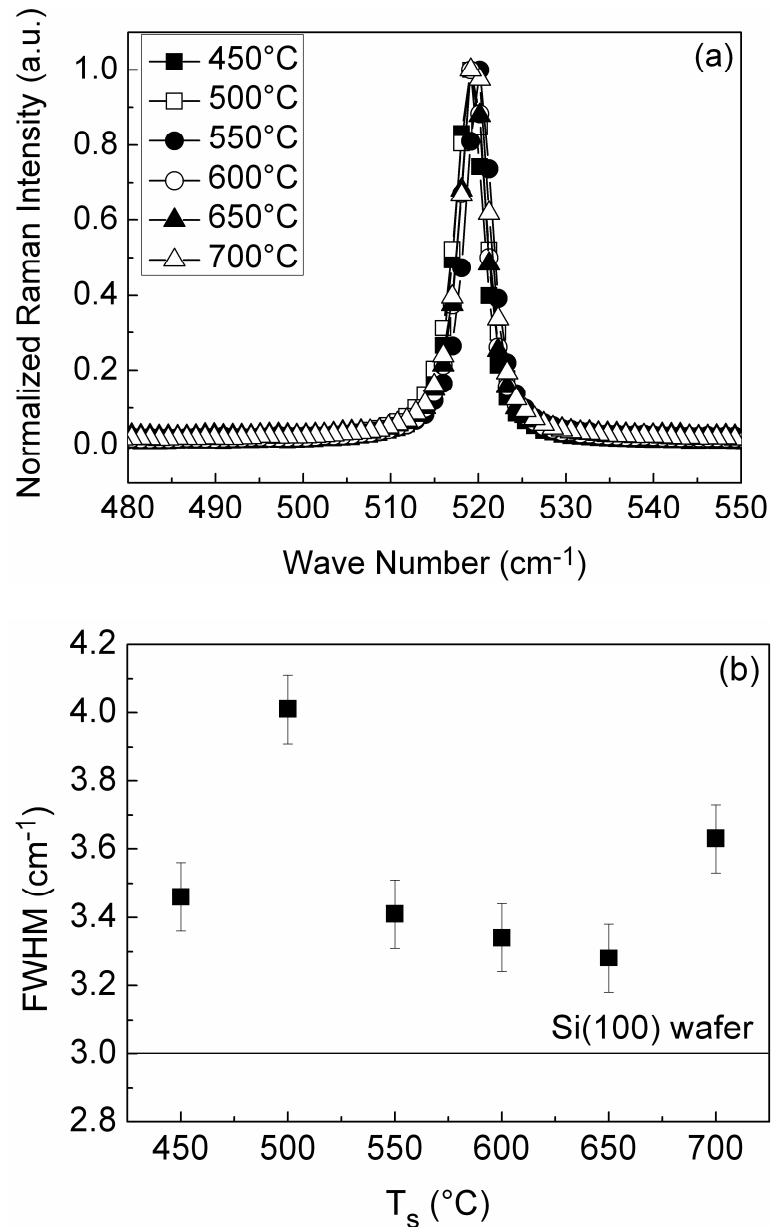


Figure 5.3 Normalized Raman intensity versus wave number for the epitaxial poly-Si films grown on poly-Si seed layers on glass deposited at $T_s = 450\text{-}700\text{ }^\circ\text{C}$ (a) and corresponding FWHM values (b). The solid line represents the FWHM value of a c-Si wafer as a reference.

the poly-Si seed layer on glass. All the images of the poly-Si films exhibit the characteristic grain size and orientation of the poly-Si seed layers. This means on the whole area investigated, a complete epitaxial growth with a preferential (100) orientation (red areas) could be obtained for the whole substrate temperature range investigated. Based on these results, we can conclude that poly-Si seed layers behave as a template for the subsequent epitaxial growth of the poly-Si films. Smaller grains towards non-(100) orientations could be also epitaxially thickened. In this work it is shown for the first time that even at very low substrate temperatures of $T_s = 450$ °C, epitaxial growth could be obtained on the whole area of the poly-Si seed layers including grains with different crystallographic orientations. In the literature, TEM investigations of poly-Si films grown on poly-Si seed layers on glass at 500 °C reveal regions with a microcrystalline growth, meaning that not the whole seed layer area could be epitaxially thickened [56].

These results have been confirmed by the corresponding Raman measurements performed on the epitaxial poly-Si films. All poly-Si films grown on poly-Si seed layers exhibit a peak positioned at 520 cm^{-1} that corresponds to the c-Si peak (Figure 5.3.a). Even at very low substrate temperatures (e.g. $T_s = 450$ °C) no additional peaks related to a-Si or $\mu\text{c-Si}$ formation could be observed. These results additionally prove that epitaxial growth could be obtained on the whole area of the poly-Si seed layers for the whole substrate temperature range investigated. Corresponding FWHM values calculated from the Raman spectra are plotted in Figure 5.3.b. FWHM values of the epitaxial poly-Si films do not show a clear dependence on the substrate temperature. In general FWHM values between 3.3 to 4.0 were obtained. Compared to a FWHM value of 3.0 for a reference c-Si wafer, calculations show that the structural quality of the epitaxial poly-Si films are highly qualified for a use as an absorber layer in a thin-film poly-Si solar cell configuration.

5.3.2 Influence of the Underlying Grain Orientation

Defects are generated e.g. due to imperfections of the growth surface, the surface energy of the crystal grains and the incorporation of contaminants during epitaxy. In chapter 4, the influence of the underlying crystallographic orientations for an epitaxial growth on c-Si wafers was observed and discussed for Si(100) and Si(111). In this

section, influence of the underlying crystallographic orientation is examined for the epitaxial growth on poly-Si seed layers on glass. Figure 5.4 presents the surface of a Secco-etched poly-Si film grown at $T_s = 600$ °C together with its corresponding EBSD color-encoded orientation map. Secco etching serves for revealing crystallographic defects in the epitaxially grown poly-Si films.

The large grains of about 15 μm (in the center of Figure 5.4) exhibit an almost smooth surface even after defect etching. Corresponding EBSD analysis shows that these grains have a (100) crystallographic orientation (red). On the other hand, grains with non-(100) orientation reveal a higher density of defects (for example circled areas in Figure 5.4). Especially small grains towards (111) orientation (blue) result in an epitaxial growth with high density of defects. Black regions in the figure correspond to parts which could not be analyzed due to the roughness caused by strong etching. These results agree well with the results of defect etching experiments on epitaxial layers

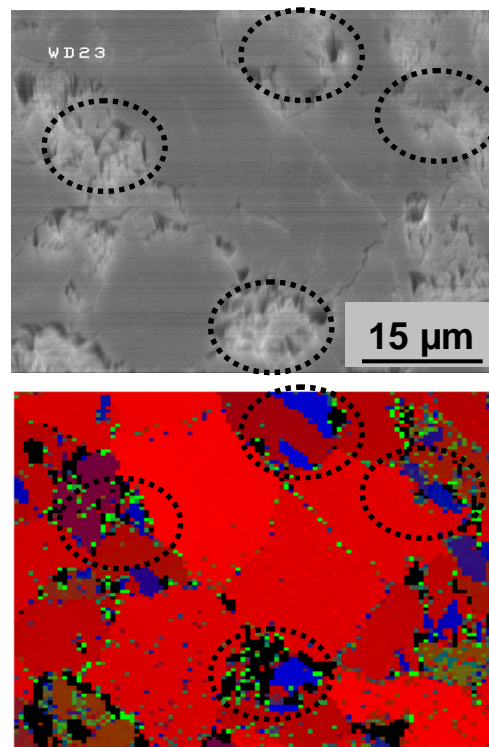


Figure 5.4 SEM image of a Secco-etched Si film grown on a poly-Si seed layer at $T_s = 600$ °C with $r_{\text{Si}} = 150$ nm/min and its corresponding EBSD color-encoded orientation map. (Color coding: red (100), blue (111), green (110))

grown on Si(100) and Si(111) wafers. Almost no etch pits were observed on the smooth films grown on Si(100), whereas about 10^8 cm⁻² etch pits could be detected on films grown on Si(111) at $T_s = 600$ °C . As a summary, the grain orientation distribution of the underlying poly-Si seed layer has a great impact on the epitaxial quality of the growing poly-Si film. In the literature the influence of the underlying crystallographic orientation on the structural quality of the epitaxial poly-Si films were discussed controversially. Harder showed that the crystallographic orientation of the poly-Si seed layer grains does not play the dominant role in determining the structural quality of the subsequently grown epitaxial poly-Si films at 630 °C [56]. On the other hand, investigations of Wagner et al. revealed that light beam induced current measured on the epitaxial poly-Si films grown on poly-Si wafer substrates shows grain orientation dependence [51].

Analyzing the SEM images (as well as optical light microscope images) of the epitaxial poly-Si films after defect etching, we found that about 60% of the total sample surface exhibits less defective grains. This finding agrees well with the EBSD measurements of our poly-Si seed layers which reveal that 60% of the grains are preferentially (100) oriented. As shown, this orientation is favorable for low defective epitaxial growth. Therefore, for obtaining device-grade poly-Si films not only the grain size is of great importance but also especially the crystallographic orientation distribution plays a crucial role.

5.3.3 Intra-Grain Defects in Epitaxial Poly-Si Films

Analysis of defect centers, their origin and electrical activity as recombination centers is of importance for understanding the performance of the epitaxially grown poly-Si absorber layers. The defects of the epitaxial poly-Si films have been revealed by means of anisotropic defect etching. A SEM image of the poly-Si film grown at $T_s = 550$ °C on a poly-Si seed layer on glass after Secco etching is shown in Figure 5.5.a. The grain marked with dashed lines is shown in Figure 5.5.b in a bigger magnification. In Figure 5.5.a, it is seen that while some of the grains exhibit less defective epitaxial growth, some other grains exhibit a more defective growth. The reason has been already explained in section 5.3.2 as the influence of the underlying crystallographic orientation. Similarly here grains towards (100) orientation exhibit low density of

defects (e.g. grain marked with dashed lines), whereas grains towards other orientations exhibit a higher density of defects (different orientations of the grains inferred from the EBSD investigations in section 5.3.2).

The area of less defectively grown grains corresponds to about 60% of the total area of the sample surface analyzed. This corresponds to the amount of preferential (100) orientation of the poly-Si seed layer grains. From Figure 5.5.b it is seen that (100) grains exhibit intra-grain line defects (points in the figure). The density of these dislocations on (100) grains corresponds to about $3.5 \times 10^8 \text{ cm}^{-2}$. However, these grains exhibit no stacking faults. In addition, grain boundary regions seem to be affected from the etching process meaning that defects were also formed along the grain boundaries.

A cross-sectional TEM image of an epitaxial poly-Si film grown on a poly-Si seed layer at $T_s = 600 \text{ }^\circ\text{C}$ is shown in Figure 5.6. The sample has seen a short defect etching in order to reveal the defects. Focused Ion Beam (FIB) lift-out has been used for the sample preparation. The interface between the poly-Si seed layer and the epitaxially grown poly-Si film can be easily distinguished. The thicknesses of the poly-Si seed layer and epitaxially grown poly-Si film are about $0.3 \text{ }\mu\text{m}$ and $3 \text{ }\mu\text{m}$, respectively. The Si film grown on the poly-Si seed layer is completely crystalline (see Figure 5.3), which showed no sign of an a-Si tissue. In Figure 5.6, two neighboring grains (grain1 and 2) with different defect types and densities can be seen. Grain 1 exhibits mainly dislocations whereas grain 2 suffers from a very high density of extended defects and twins. From the SEM images of this sample (not shown here) together with the previous

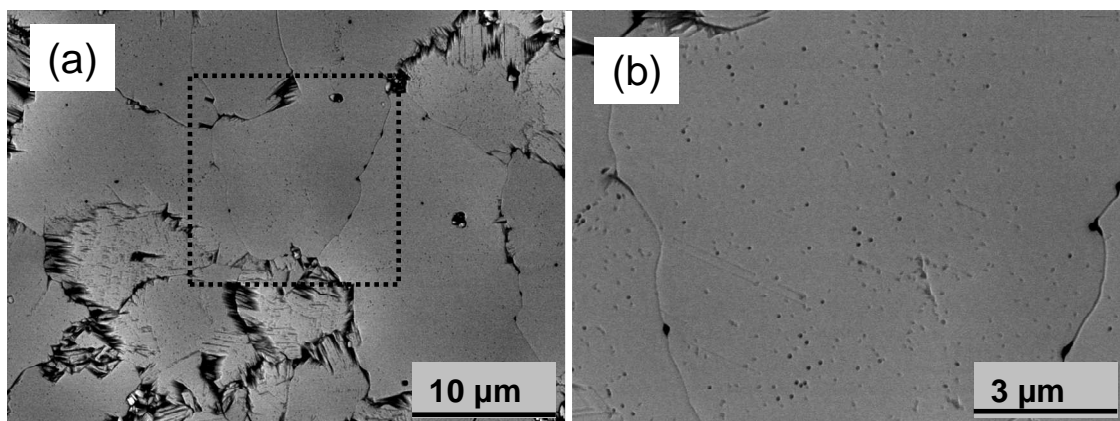


Figure 5.5 SEM image of a Secco-etched Si film grown on a poly-Si seed layer at $T_s = 550 \text{ }^\circ\text{C}$ (a), and a bigger magnification of the grain marked with dashed lines (b).

correlations of EBSD measurements, it can be inferred that grain 1 has a (100) orientation whereas grain 2 exhibits a non-(100) orientation. Despite of the high-quality epitaxy obtained on Si(100) wafers, epitaxial poly-Si films grown on poly-Si grains with (100) orientation (grain 1) exhibit dislocation lines. A part of these defects are originating at the poly-Si seed layer epitaxial film interface or inside the seed layer. Therefore, preparation of a clean and atomically flat surface of the seed layer is a critical issue for successful epitaxy on poly-Si seed layers. In this work CMP has been applied for preparing a flat seed layer surface. However, this method may also create imperfections on the seed layer surface which would strongly influence the epitaxial film quality. Another critical point is the hydrogen termination of the seed layer surface. If hydrogen termination of the seed layer surface deteriorates before the start of epitaxy, this would lead to surface contamination with C, O and N from the non-ultra high vacuum environment of the e-beam. Therefore a possible explanation for this defect distribution may be contamination of the seed layer surface or a non-ideal surface finish of the seed layer. On the other hand, with increasing distance from the seed layer epitaxial film interface the defect density decreases significantly. This behavior has been already observed by other researchers [56]. This result may be attributed to the angle of the dislocation lines which may not be parallel to the film cross section surface. On the other hand, non (100) oriented grains exhibit much more defects in the form of twins. The defective growth on non-(100) oriented grains can be already seen from the top view SEM images (Figure 5.4).

The epitaxial growth quality is strongly dependent on the underlying

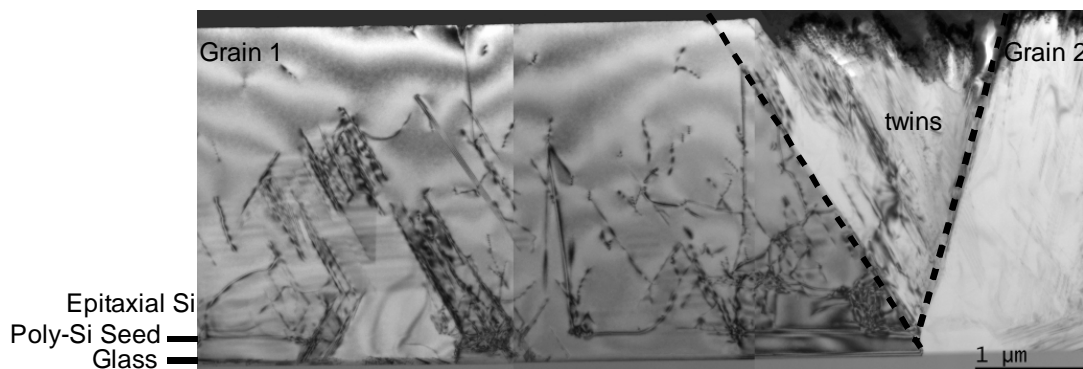


Figure 5.6 Cross-sectional TEM image of an epitaxial poly-Si film grown on a poly-Si seed layer at $T_s = 600$ °C. Sample has seen a short defect etching in order to reveal the defects.

crystallographic orientation of the seed grain and the seed layer surface imperfections. Therefore increasing the percentage of the preferential (100) orientation of the grains or preparing a defect-free seed layer surface would lead to a great improvement on the epitaxial growth quality on all of the grains of the poly-Si seed layers. In addition, further passivation of the electronically active defects can be achieved by post-deposition treatments such as rapid thermal annealing, which also activates dopants, and by hydrogenation. Correspondingly, the combination of poly-Si seed layers prepared by AIC and subsequent epitaxial growth by e-beam is a very promising candidate for producing high-quality absorber layers for thin-film Si solar cells on glass.

Defect formation in the epitaxial poly-Si films grown on the poly-Si seed layers strongly depend on the seed layer preparation conditions, substrate type, roughness and cleaning. Comparison of the epitaxial growth on poly-Si seed layers prepared by AIC from this work and prepared by another institute (IMEC) is presented in Figure 5.7.a-c. All samples were defect etched for defect revealing. Figure 5.7.a shows a defect-etched surface of a poly-Si film epitaxially grown by e-beam evaporation at $T_s = 600$ °C on a poly-Si seed layer on glass. Figure 5.7.b presents a defect-etched surface of a poly-Si film epitaxially grown by CVD at about $T_s = 1100$ °C on a poly-Si seed layer on an alumina substrate coated with flowable oxide. Figure 5.7.c illustrates the same seed layer as in Figure 5.7.b epitaxially grown by e-beam evaporation at $T_s = 600$ °C.

In Figure 5.7.a (100) oriented grains co-exist with non-(100) oriented grains. The (100) oriented grains exhibit typical etch pits for dislocations as it was observed in Figure 5.5.b. In comparison Figure 5.7.b represents a (100) grain epitaxially grown on poly-Si seed layer on an alumina substrate. This grain exhibits not only dislocations but also typical etch pits for the stacking faults of (100) epitaxy. The density of these stacking faults was recorded to be about 10^9 cm⁻² [22]. Moreover, investigations reveal that these stacking faults are active recombination centers [22]. Therefore, they play an important role for the quality of the poly-Si absorber layers. The difference obtained between Figure 5.7.a and b can have various explanations. First, different epitaxial growth methods and temperatures may result in distinct morphologies of the film surfaces and can influence the defect formation. However, Figure 5.7.c reveals that when the same seed layer on alumina has been epitaxially overgrown with e-beam evaporation, the same stacking faults on (100) oriented grains can be observed. This confirms that the formation of stacking faults on (100) surfaces is independent of the epitaxial deposition method or temperature. A possible explanation is that substrate

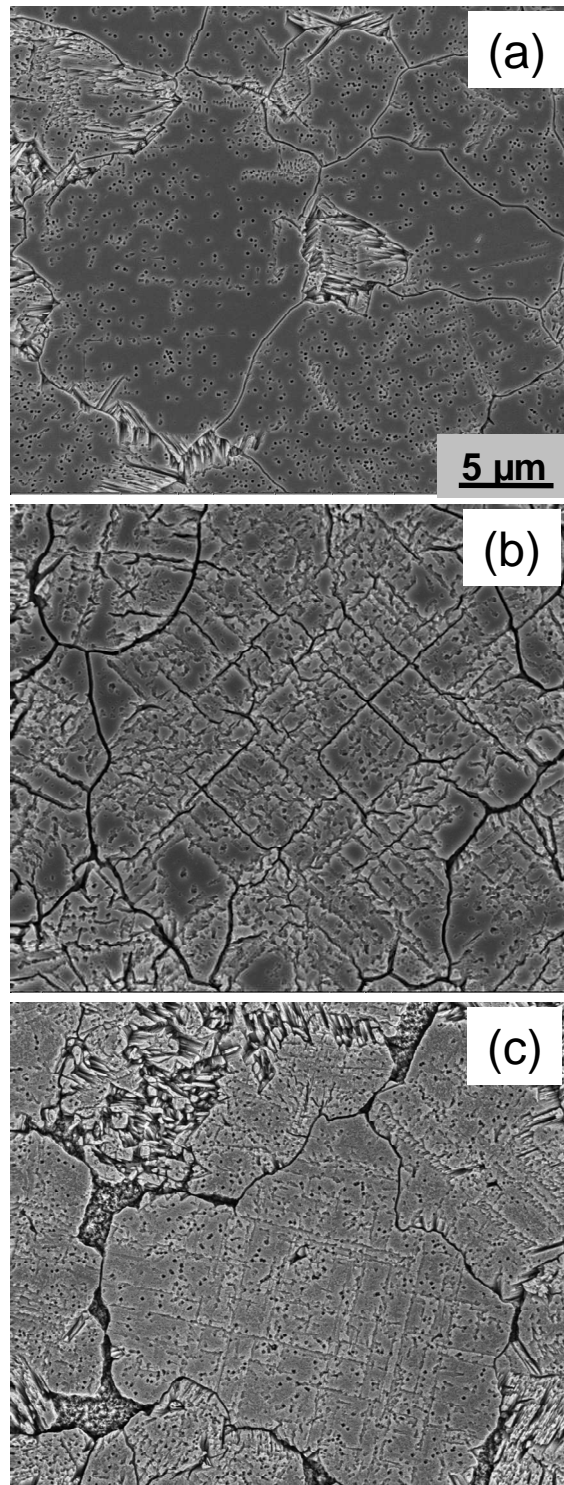


Figure 5.7 Top view SEM image of the defect-etched surfaces of epitaxial poly-Si films grown by (a) e-beam evaporation at $T_s = 600\text{ }^\circ\text{C}$ on a poly-Si seed layer on glass, (b) CVD at about $T_s = 1100\text{ }^\circ\text{C}$ on a poly-Si seed layer on an alumina substrate coated with flowable oxide, (c) e-beam evaporation at $T_s = 600\text{ }^\circ\text{C}$ on a similar seed layer as (b).

type, cleaning, roughness and/or slight variations in the seed layer preparation process lead to formation of a high density of stacking faults on (100) grains. In this work, epitaxial growth on (100) grains only exhibit dislocations but no stacking faults.

The electrical activity of defects observed in the epitaxial poly-Si films is an important property since it controls the quality of the p-n junction. Therefore defect centers and the homogeneity of the epitaxial poly-Si films grown by e-beam evaporation at $T_s = 600$ °C on poly-Si seed layers on glass were investigated by EBIC measurements. Figure 5.8.a-c illustrates the EBIC images taken at 6.5 keV, 10 keV and 15 keV beam energies corresponding to penetration depths of about 0.45 μm , 0.96 μm and 2 μm respectively. The epitaxial poly-Si film thickness under investigation was about 2 μm . In Figure 5.8.a almost no contrast between different grains can be distinguished and all grains show a bright EBIC image. This tells that the epitaxial film is homogeneous at the top 0.45 μm and no grain orientation dependent recombination can be detected. Moreover, the high collection efficiency near the surface can be also attributed to the influence of the electric field of the p-n junction. The dark spots seen at the grain boundaries correspond to holes. Once we examine deeper in the epitaxial film (0.96 μm , Figure 5.8.b), we begin to see that some smaller grains and the grain boundaries reveal a darker contrast compared to bigger grains. From previous investigations we know that bigger grains usually have preferential (100) orientation, whereas smaller grains are usually towards non-(100) orientations. Due to the higher defect density observed in non-(100) orientations, these grains reveal dark regions and therefore behave as recombination centers. As we reach to the interface of the epitaxial poly-Si film and poly-Si seed layer (2 μm , Figure 5.8.c), the contrast between the grains becomes more visible. The presence of intra-grain defects in (100) oriented grains was illustrated in Figure 5.5.b. However, due to the resolution limits of the EBIC measurement setup, we could not detect whether these intra-grain defects in (100) oriented grains are electrically active or not.

EBIC collection efficiency measured for such a typical epitaxial poly-Si film grown on poly-Si seed layers at $T_s = 600$ °C was compared to the epitaxial Si films grown on Si(100) and Si(111) substrates at $T_s = 600$ °C (from Figure 4.14). The comparison is plotted in Figure 5.9. Due to the epitaxial film thickness of about 2 μm , epitaxial film/substrate interface has been marked at 15 keV beam energy.

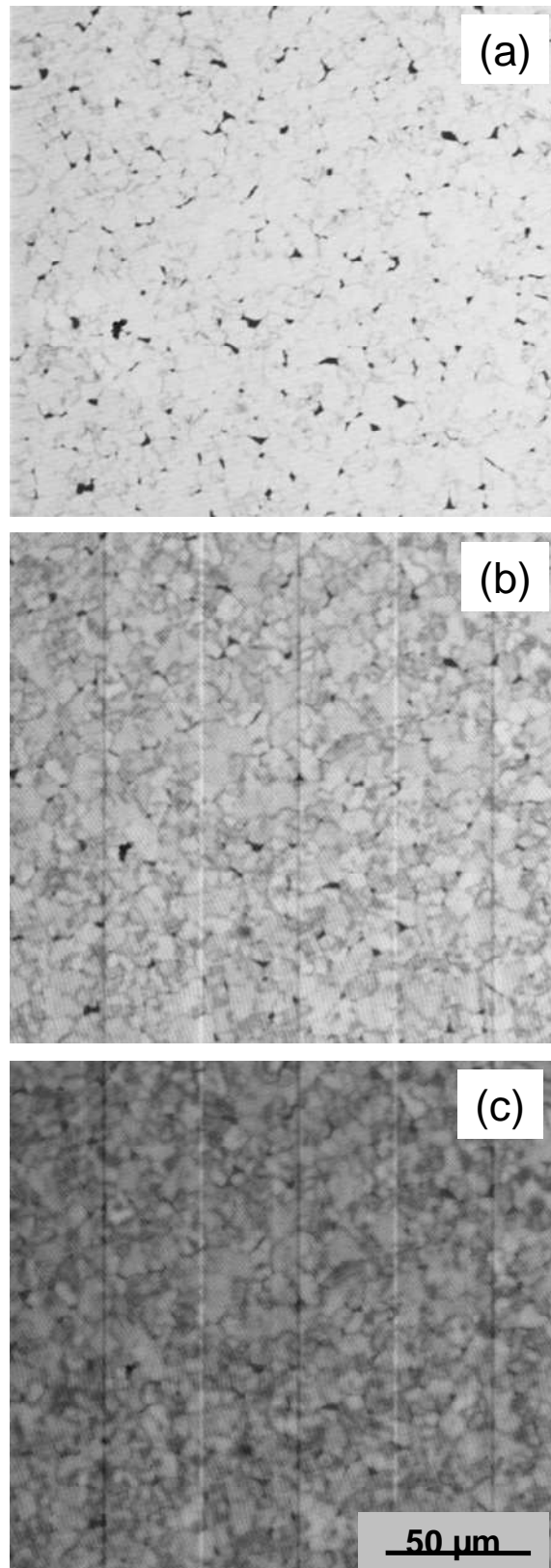


Figure 5.8 EBIC images of epitaxial poly-Si films grown by e-beam evaporation at $T_s = 600$ °C on poly-Si seed layers on glass at beam energies of (a) 6.5 keV, (b) 10 keV and (c) 15 keV respectively.

Figure 5.9 depicts that EBIC collection efficiency increases and reaches to a maximum at a certain depth of the epitaxial film and then it starts to decrease towards the epitaxial film/substrate interface again. At the epitaxial film/substrate interface the poly-Si sample on glass reveals a collection efficiency of about 47%, compared to 68% and 89% for epitaxial Si films on Si(111) and Si(100) wafers, respectively. Lower collection efficiency of the epitaxial Si films on Si(111) compared to Si(100) was explained by an enhanced extended defect density obtained as a results of epitaxy on Si(111) (section 4.3). Therefore, a lower collection efficiency of the epitaxial poly-Si films can be explained by the coexistence of different oriented grains, grain boundaries and defects generated at the interface due to the imperfections of the seed layer. The collection efficiency of the epitaxial poly-Si film increases towards the film surface and reaches to a maximum of about 71% at about 0.65 μm (8keV). For comparison the collection efficiency of the epitaxial Si film on Si(111) reaches a maximum of about 82% at about 0.65 μm and that of epitaxial Si film on Si(100) peaks at 93% at about 1.3 μm (12keV). This shows that the peak position of the epitaxial poly-Si film follows the trend for the epitaxial Si film on Si(111) wafers. However, the collection in the bulk of the epitaxial poly-Si film is lower compared to that of epitaxial film on Si(111). On the other hand, the peak position of the epitaxial Si film on Si(100) reveals that overall collection occurs in a bigger volume of the epitaxial film and with a high efficiency.

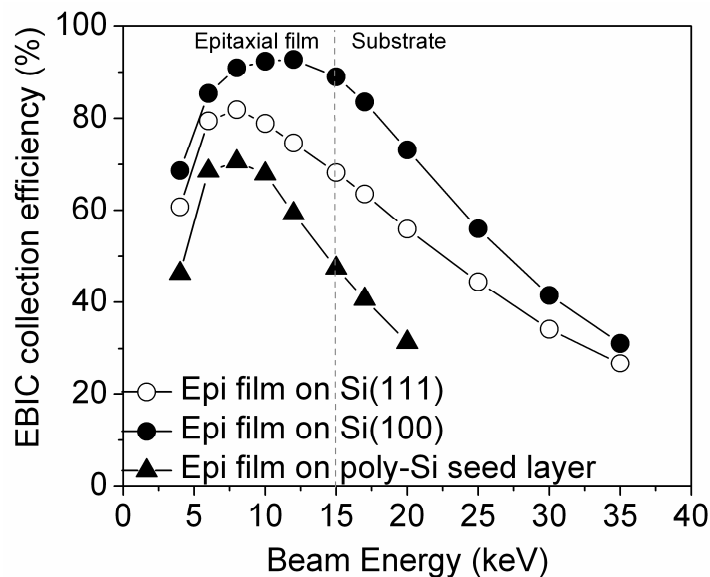


Figure 5.9 EBIC collection efficiency versus the beam energy for the epitaxial poly-Si films grown on poly-Si seed layers at $T_s = 600\text{ }^\circ\text{C}$ compared with epitaxial Si films grown on Si(100) and Si(111) wafers at $T_s = 600\text{ }^\circ\text{C}$.

5.3.4 SIMS results

The incorporation of background contaminants during the epitaxial growth (non-ultra high vacuum conditions of e-beam evaporation and due to out-gassing issues caused by the glass substrate) can strongly influence the electrical quality of growing Si films. Possible contaminants present in the epitaxial Si films grown on poly-Si seed layer coated glass and poly-Si seed layer coated oxidized wafer substrates were investigated by SIMS. Since glass itself can also cause out-diffusion of some of the elements present in Borofloat glass (eg. O, Al, B), the use of an oxidized wafer substrate serves for eliminating the influence of the glass substrate and monitoring the contaminants that are only caused by the poly-Si seed layer and/or by the non-ultra high vacuum conditions of the e-beam system. In Figure 5.10.a and b concentrations of O, N and Al, B are plotted as a function of depth, respectively. The epitaxial Si films were deposited at $T_s = 600\text{ }^\circ\text{C}$ with a Si deposition rate of about 180 nm/min and a thickness of about 2 μm . Both samples were prepared in the same deposition run in order to keep the influence of the background contamination level the same. The vertical dashed lines in the graphs represent the epitaxial film/substrate interface.

Figure 5.10.a shows the concentrations of O and N in the epitaxially grown Si films. Both elements exhibit an almost constant level throughout the epitaxial film starting from the surface. Approaching the epitaxial Si film/poly-Si seed layer interface, an increase of the level for both of the elements can be observed. The average concentration of O is about $5 \times 10^{17}\text{ cm}^{-3}$ and $1 \times 10^{17}\text{ cm}^{-3}$ for epitaxial Si films grown on poly-Si seed layer coated glass and poly-Si seed layer coated oxidized wafer substrates, respectively. This level was evaluated up to a depth of about 1.6 μm where the concentration is constant. This result reveals that a higher O concentration obtained for the epitaxial growth on glass substrate is a consequence of an out-diffusion from the glass during deposition. In a previous investigation, we have detected a concentration of O for an epitaxially grown Si film on Si(100) wafer at a level of about $5 \times 10^{16}\text{ cm}^{-3}$ [88]. This level is comparable to the level detected in the FZ Si wafer (10^{16} cm^{-3}). This shows that having a high-rate deposition the background level of O present in the epitaxially grown Si films stays at a reasonable level. However, in case of a glass substrate additional contamination is caused by the out-diffusion process. Therefore, the use of a diffusion barrier between the glass and poly-Si seed layer is necessary. In the literature,

the concentration of O in the epitaxially grown Si films could be detected at a low level of about $3 \times 10^{16} \text{ cm}^{-3}$ in the case when a SiN diffusion barrier was used between the glass substrate and the poly-Si seed layer [33]. For this reason, during this work a few investigations were performed using different diffusion barriers (SiN, ZnO). However, the investigations done so far could not reveal a clear result. The level of $1 \times 10^{17} \text{ cm}^{-3}$ obtained for poly-Si coated oxidized wafer substrates reveal that not only the glass substrate causes an out-diffusion but also the seed layer itself. The concentration of O

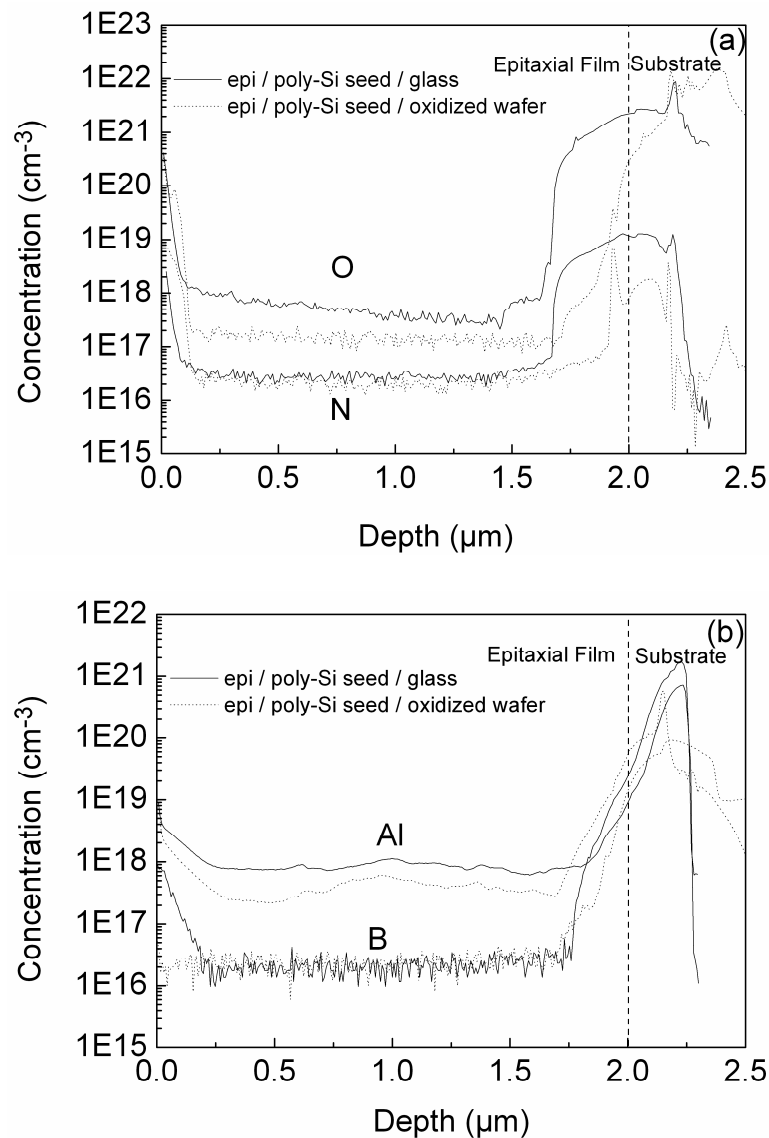


Figure 5.10 SIMS profile of (a) O, N and (b) Al, B in the epitaxially grown poly-Si films on poly-Si seed layer coated glass substrate (solid lines) and oxidized Si wafer (dotted lines). Epitaxial Si films were grown at $T_s = 600 \text{ }^\circ\text{C}$ with a Si deposition rate of about 180 nm/min. The film thickness is about 2 μm . The vertical dashed line marks the interface between the epitaxial Si film and the poly-Si seed layer.

increases dramatically approaching the epitaxial film/poly-Si seed layer interface. At this depth, one should be careful to evaluate the exact values of the levels since the sputtering rate plays a crucial role especially when measuring at the grain boundaries.

Similarly, a N concentration of about $3 \times 10^{16} \text{ cm}^{-3}$ and $2 \times 10^{16} \text{ cm}^{-3}$ for epitaxial Si films grown on poly-Si seed layer coated glass and poly-Si seed layer coated oxidized wafer substrates was detected, respectively. The level of N found in this investigation is in agreement with the N levels reported in the literature for the epitaxial Si films on poly-Si seed layer coated glass substrates [33]. The investigation of the N concentration in an epitaxial Si film grown on Si(100) wafer revealed a level of about $1.5 \times 10^{16} \text{ cm}^{-3}$ compared to a level of about $2 \times 10^{15} \text{ cm}^{-3}$ in the CZ wafer used [88]. This result reveals that an increased level of N contamination in the epitaxially grown Si films on different substrates is mainly caused by the non-ultra high vacuum environment of the deposition system. However this level is still reasonable for solar cell applications. A higher level observed for the glass substrate can be explained with additional out-diffusion from the substrate as it can be already seen in Figure 5.10.a.

The concentrations of the dopants (Al and B) are plotted in Figure 5.10.b. B doping was realized intentionally using the high-temperature effusion cell via evaporation of elemental boron. Al, however, appears as an unintentional dopant due to the high Al concentration present in the poly-Si seed layer. The level of the Al concentration was detected at about $9 \times 10^{17} \text{ cm}^{-3}$ and $4 \times 10^{17} \text{ cm}^{-3}$ for epitaxial Si films grown on poly-Si seed layer coated glass and poly-Si seed layer coated oxidized wafer substrates, respectively. This level of Al for the base region is very high, and if electrically active can dominate the doping level of the epitaxial films. The reason of high Al concentration is clearly seen as an out-diffusion from the poly-Si seed layer. The Al concentration of the poly-Si seed layer is about $1\text{-}3 \times 10^{20} \text{ cm}^{-3}$. The difference of the levels between glass and oxidized wafer substrates also reveals that an additional out-diffusion from the glass substrate is expected. In case of epitaxial Si film growth on Si(100) wafer a very low level of Al concentration below 10^{14} cm^{-3} could be detected in the epitaxial films showing that this high level for poly-Si samples are mainly caused by the out-diffusion from the poly-Si seed layer and the glass substrate [57].

The level of the B concentration is about $2 \times 10^{16} \text{ cm}^{-3}$ and $2.3 \times 10^{16} \text{ cm}^{-3}$ for epitaxial Si films grown on poly-Si seed layer coated glass and poly-Si seed layer coated oxidized wafer substrates, respectively. The level of the B concentration agrees well

with the intentional doping level as calibrated in Figure 4.5. C-V measurements performed for solar cells prepared by the epitaxial Si films on poly-Si seed layer coated glass substrates reveal a doping level of $1\text{-}2 \times 10^{16} \text{ cm}^{-3}$. This agrees well with the measured level of the B concentration by SIMS. On the other hand, this gives an information that the high Al level detected by SIMS is not electrically active and hence do not influence the doping level of the epitaxial films. However, finding the reason of this high Al level and eliminating it are critical subjects for further improvement of the thin film poly-Si solar cells.

Furthermore, the levels of other metallic impurities (e.g. Fe, Cu, Ta, W) known as the “life time killers” in Si were also investigated. The Fe concentration is found about the detection limit of $1 \times 10^{16} \text{ cm}^{-3}$. Cu and W are throughout the film close to the detection limit of $2 \times 10^{15} \text{ cm}^{-3}$. Similarly Ta has a level of $5 \times 10^{15} \text{ cm}^{-3}$. All the levels of metallic impurities are very low and close to the detection limit of SIMS.

5.4 Epitaxial Growth on Poly-Si Seed Layers on Glass Prepared by Laser Crystallization (LC) of a-Si

There are also different alternative ways for preparing large-grained poly-Si seed layers other than AIC of a-Si. One alternative approach of preparing large-grained poly-Si seed layers is based on laser crystallization (LC) of a-Si. In this approach, first a thin (about 400 nm) a-Si layer was deposited on glass substrates by e-beam evaporation. Later, this layer was crystallized using a diode laser (808 nm) in an air ambient. The

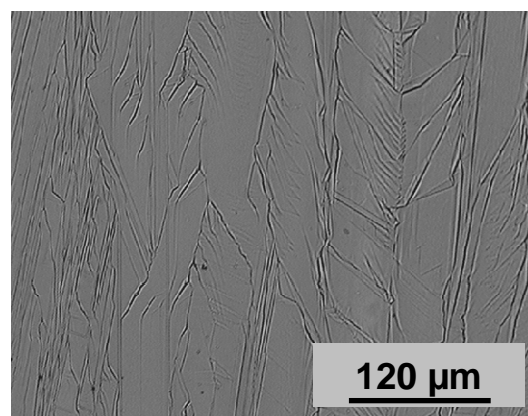


Figure 5.11 Optical microscope image of a LC poly-Si seed layer on glass showing the grain size and structure.

resulting poly-Si seed layers feature large grains in the order of 100 μm [89]. The optical microscope image of a typical LC poly-Si seed layer surface (Figure 5.11) illustrates the grain structure.

Epitaxial films of about 2 μm thickness were grown at $T_s = 600$ $^\circ\text{C}$ using e-beam evaporation on poly-Si seed layers prepared by LC. Since LC poly-Si seed layers were prepared under air ambient a thicker oxide layer was formed on the poly-Si film which has to be removed prior to epitaxy. The standard HF treatment that was applied for AIC poly-Si seed layers was applied for these seed layers, too. However, first attempts resulted in non-epitaxial growth due to an incomplete removal of the oxide layer related to short HF dipping times. Therefore, longer HF times of up to 2 minutes were applied until the poly-Si seed layer surface was completely hydrophobic. Figure 5.12 illustrates the comparison of the Raman measurements performed on poly-Si films grown on poly-Si seed layers prepared by LC and AIC (from Figure 5.3). A clear c-Si peak at 520 cm^{-1} can be observed which illustrates the successful epitaxy obtained on both type of seed layers. No a-Si or μc -Si related peak was observed at lower wave numbers, indicating that both films are fully crystalline. The FWHM of both epitaxial poly-Si films is about 3.4, not much larger than the FWHM of 3 for epitaxial Si films on mono-Si wafers, reflecting the high quality achieved.

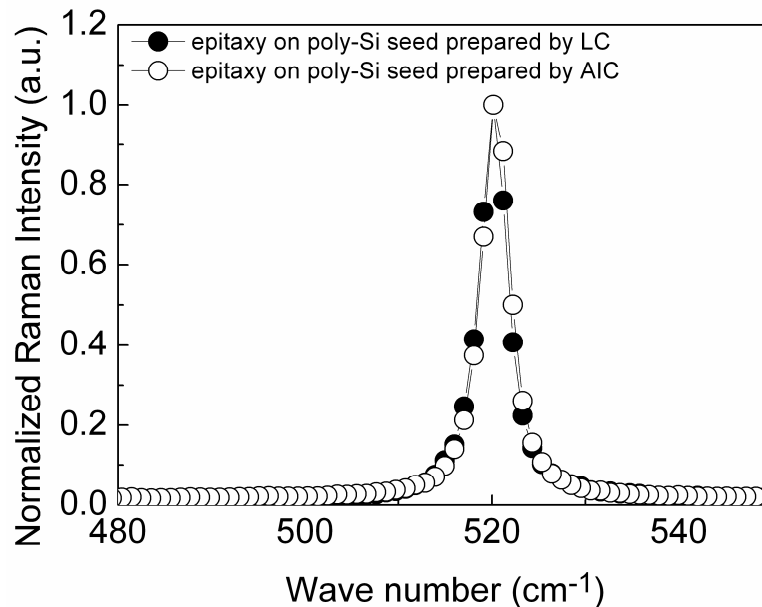


Figure 5.12 Normalized Raman intensity versus wave number for the epitaxial poly-Si films grown on poly-Si seed layers on glass prepared by (●) LC and (○) AIC at $T_s = 600$ $^\circ\text{C}$.

The EBSD color-encoded orientation map and the corresponding pole figure of the epitaxial poly-Si films grown on poly-Si seed layers prepared by LC are shown in Figure 5.13. Columnar grains up to 100 μm can be distinguished. This grain size is much larger than for the epitaxial poly-Si films grown on poly-Si seed layers prepared by AIC which is about 5-20 μm . Hence it has the potential to decrease the recombination caused by the grain boundaries given the fact that the intra-grain defect density can be kept at low levels. However, one can see that there is no clear preferential (100) orientation of the epitaxial films grown on poly-Si seed layers prepared by LC. The grains are rather randomly oriented. This is related to the fact that LC seed layer grains are randomly oriented as well. A high density of (111) oriented grains (blue) can be recognized. As it was mentioned in the previous sections, preferential (100) orientation is very beneficial for the subsequent epitaxy of the poly-Si film. On the other hand, defect formation on non-(100) orientations is inevitable.

Figure 5.14 illustrates SEM images of Secco etched surfaces of epitaxial poly-Si films grown on LC seed layers. In the upper SEM image two neighboring grains separated with a grain boundary reveal the existence of different etch pit shapes and densities. In addition, the formation of a sub-grain is also marked with the dashed lines. The typical triangular etch pits reveal that the grain on the left is (111) oriented whereas the grain on the right has a (100) orientation. The lower SEM images show the magnified areas from both grains. The stacking fault density of the (111) oriented grain is much higher than 10^8 cm^{-2} . On (100) oriented grain, circular etch pits for dislocations

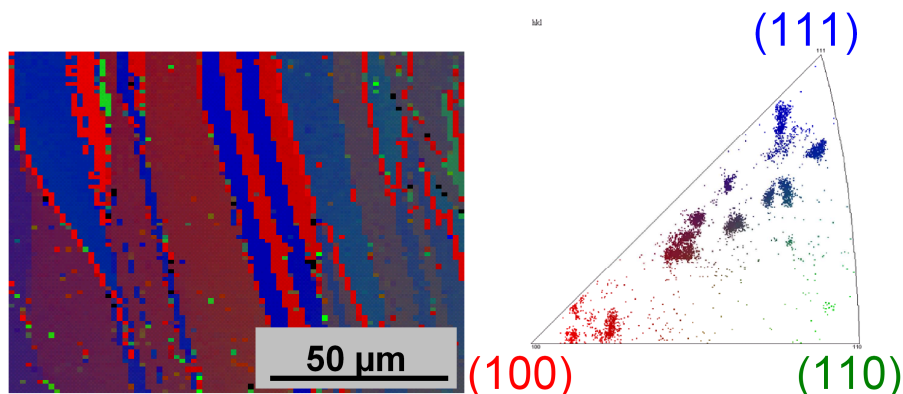


Figure 5.13 EBSD orientation map of the epitaxial poly-Si film on a poly-Si seed layer prepared by LC on glass and the corresponding inverse pole figure.

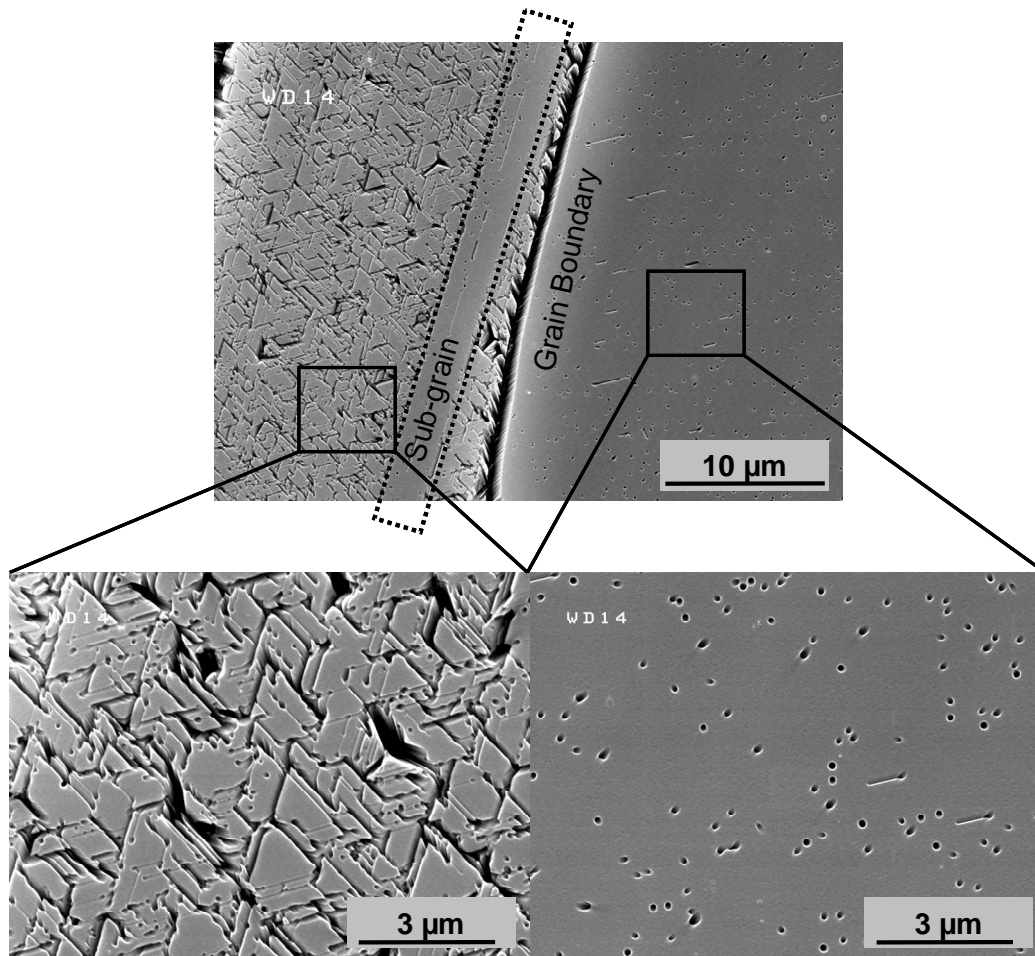


Figure 5.14 SEM image of a Secco-etched poly-Si film grown at $T_s = 600\text{ }^\circ\text{C}$ on a poly-Si seed layer prepared by LC. Lower images show the marked regions in the upper image in a bigger magnification.

result in a defect density of about 10^8 cm^{-2} . In addition a few stacking fault lines can be also observed (straight lines in the image). Compared to the dislocation density of $3.5 \times 10^8\text{ cm}^{-2}$ obtained for the (100) grains of poly-Si films grown on poly-Si seed layers prepared by AIC (Figure 5.5), epitaxial (100) grains on LC seed layers exhibit a lower defect density. However, due to a random orientation of the grains on the whole film surface and a higher density of defects observed on non-(100) oriented grains, epitaxial films prepared on poly-Si seed layers prepared by LC would contain a higher density of defects compared to epitaxial films on AIC seed layers. In this case, the benefit of the large grain size of the LC seed layers is hindered by the random orientation of the grains. Further improvement is expected by producing a higher degree of preferential (100) orientation of the grains prepared by LC of a-Si on glass substrates and by lowering the intra-grain defect density.

5.5 Poly-Si Growth on Glass

In the course of this work poly-Si thin-film preparation was based on the “seed layer approach”, where first a thin poly-Si seed layer was prepared on the glass substrate and later it was epitaxially thickened. This approach has the potential of preparing large-crystalline grains. Another way of preparing poly-Si thin-film solar cell is based on depositing Si films directly on the glass substrate and subsequently applying solid phase crystallization (SPC) at temperatures compatible with the glass substrate (at 600 °C). Using this method, sub-module efficiency of 10.5 % based on SPC of a-Si deposited by PECVD was demonstrated [16]. Unlike the seed layer approach this is not an epitaxial growth since glass has an amorphous structure. Depending on the substrate temperature, the Si film can have an amorphous or a crystalline structure. In this section, structural and electrical properties of the Si films deposited directly on glass by e-beam evaporation is discussed.

In this study, we have investigated the substitution of conventional PECVD grown p-type absorber layers with high-rate e-beam evaporation grown p-type absorber layers in a planar glass/(SiN)/n⁺(PECVD emitter)/p(e-beam absorber) sample structure. The schematic drawing of the sample prepared by SPC during this work is illustrated in Figure 5.15. The n⁺ a-Si emitter layer (30 nm) was grown by PECVD. Later, the p-type Si absorber layer (1 μm, doping level of 2x10¹⁶ cm⁻³) was grown by e-beam evaporation. For the absorber growth, substrate temperatures of T_s = 300-600 °C were used. Later, these layers were crystallized in an oven at about 600 °C.

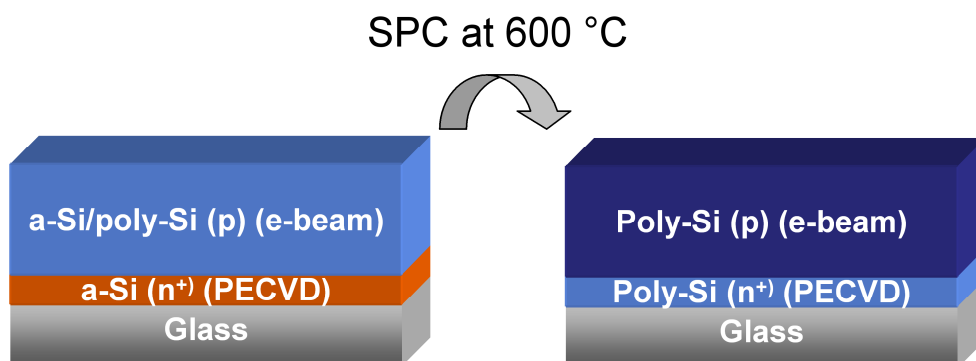


Figure 5.15 Structure of the poly-Si thin film on glass. P-type absorber layer was grown with e-beam evaporation at different substrate temperatures and subsequently crystallized at 600 °C.

The structural properties of the Si films were investigated by SEM for the substrate temperatures of 300-600 °C. Figure 5.16 shows the SEM images of the observed surface morphologies before and after SPC. The Si film grown at 300 °C exhibits no distinctive morphology as expected for an amorphous film. After SPC,

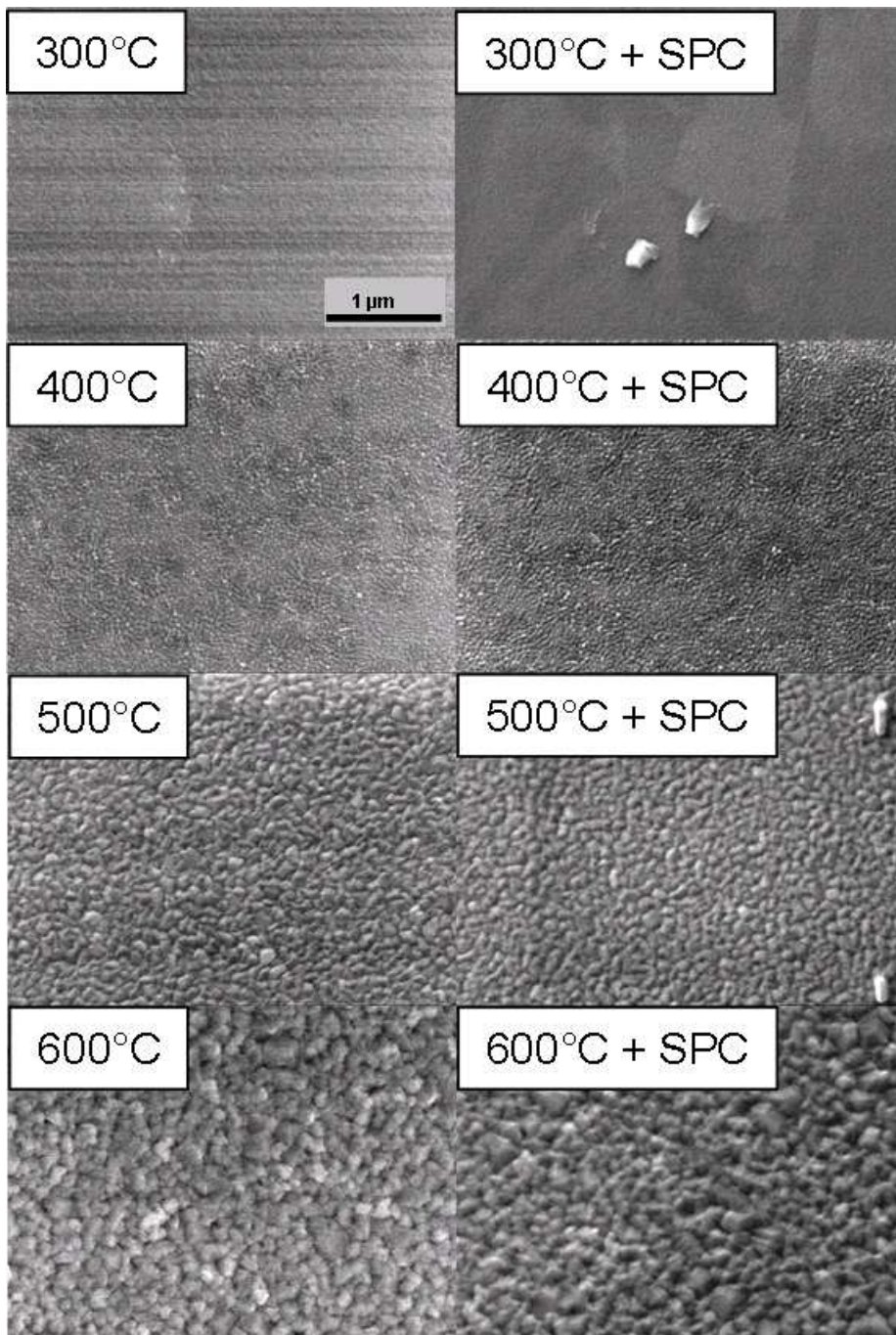


Figure 5.16 SEM images of Si film surfaces directly grown on glass by e-beam evaporation at different substrate temperatures (left row). The right row shows the same set of samples after SPC at about 600 °C [90]

crystal grains of about 1 μm size can be distinguished from the brightness contrast of the SEM image. Starting with a substrate temperature of 400 $^{\circ}\text{C}$ small crystallites can be observed already in the as grown state. After SPC, no further change could be observed in the crystal size. For higher substrate temperatures of 500 $^{\circ}\text{C}$ and 600 $^{\circ}\text{C}$, slightly bigger crystal sizes can be seen in the as-grown films. Similarly, no further change in the crystal size was observed after SPC. The grain size increases with T_s but does not exceed a few 10 nm.

Raman spectra were recorded for these films before (Figure 5.17.a) and after

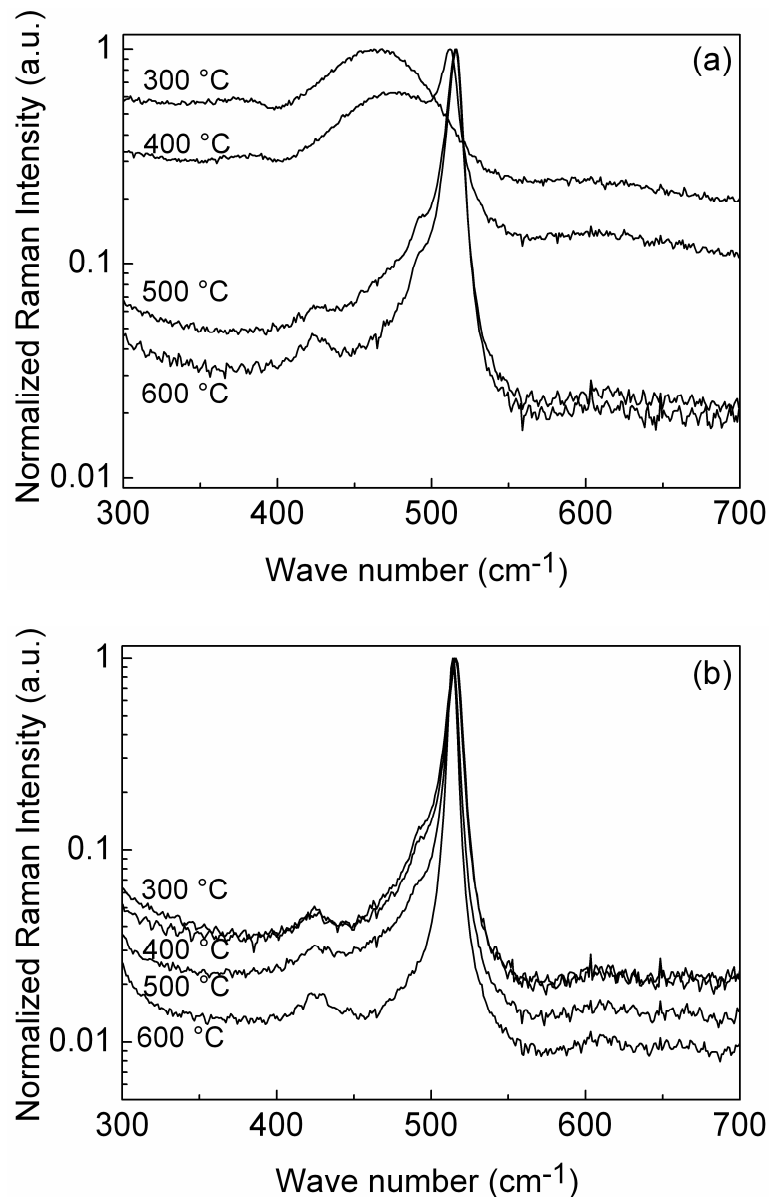


Figure 5.17 Normalized Raman intensity versus wave number for the Si films grown by e-beam evaporation at $T_s = 300\text{-}600$ $^{\circ}\text{C}$ (a) before and (b) after SPC at 600 $^{\circ}\text{C}$.

SPC (Figure 5.17.b) [90]. The Si films prepared at 300 °C has an amorphous morphology and exhibits a broad peak around 480 cm^{-1} corresponding to the transverse optical (TO) phonon of a-Si. After SPC this film is fully crystallized and exhibits the sharpest Raman peak (when compared to the other substrate temperatures) at 520 cm^{-1} corresponding to the LO-TO phonon of c-Si. In comparison, Si films prepared at 400 °C exhibit the coexistence of an amorphous and crystalline phase. For higher substrate temperatures of 500 °C and 600 °C, Raman only reveals a sharp and slightly asymmetric peak at 520 cm^{-1} . Finally, solar cells were produced by growing a p^+ BSF layer and depositing Al contacts. After the SPC process of the layers that were grown at different substrate temperatures of e-beam evaporation, the layers were treated by a hydrogen plasma in order to passivate the dangling bonds and the corresponding open circuit voltage was measured in the superstrate configuration (light entering from the glass side). Increasing the substrate temperature caused the open circuit voltages of the solar cells also to increase. The open circuit voltage increases from about 283 mV (at 300 °C) up to maximum 380 mV (at 600 °C) with increasing the absorber layer deposition temperature [91].

5.6 Summary and Conclusions

In this chapter, the properties of the epitaxial growth on poly-Si seed layers on glass were investigated in detail. Successful epitaxial growth could be obtained for a substrate temperature range of $T_s = 450\text{-}700$ °C. Even at very low substrate temperatures of 450 °C, epitaxy was obtained on the whole area with a high crystalline quality. Structural quality of the epitaxial poly-Si films revealed that they are promising candidates for the use as an absorber in thin-film Si solar cell applications. The underlying grain orientation has a great impact on the quality of the epitaxy. A much lower defect density was obtained for the (100) oriented grains compared to non-(100) oriented grains. Therefore, preferential (100) orientation of the poly-Si seed layers prepared by AIC makes them appealing for the subsequent homo-epitaxial growth. However, investigations of the intra-grain defects revealed that even (100) oriented grains contain dislocations. TEM investigations showed that these defects are usually present in the seed layer or they are originating at the seed layer/epitaxial film interface. Therefore, seed layer preparation conditions and surface treatments are extremely important for the quality of the subsequent epitaxial growth. Using SIMS measurements it was verified

that high-rate growth keeps the concentrations of most of the contaminants below the critical limit. However, the high level of Al observed in the epitaxial films is an important issue. Solving that problem can be crucial for the further improvement of the poly-Si thin films. In addition, a suitable diffusion barrier can help to prevent the out-diffusion from the glass substrate. Large grained poly-Si seed layers prepared by LC are an alternative to AIC seed layers. However, due to random orientation of the LC seed layer grains, the total defect density is also high. In order to improve epitaxial growth quality on poly-Si seed layers on glass, the imperfections in the seed layer bulk and the surface should be minimized, as well a diffusion barrier between the seed layer and the glass substrate should be implemented. A higher fraction of the preferential (100) orientation of the seed layer grains can result in a much lower defect density in the epitaxial poly-Si films. In the next chapter solar cell results of epitaxial Si films on mono-Si wafers and on poly-Si seed layers on glass will be discussed. Similar to the epitaxy on wafer we found:

- The crystalline quality of the epitaxially grown poly-Si films strongly depends on the underlying crystallographic orientation. Near-(100)-oriented grains reveal a much lower intra-grain defect density compared to non-(100)-oriented grains.
- For the whole temperature range investigated ($T_s = 450-700$ °C), epitaxial growth was obtained on the whole area of the poly-Si seed layers on glass.
- However, additional obstacles have to be taken into account. If Si films are grown on SiN coated glass (amorphous seed) smaller crystallites are obtained.
- The intra-grain defects observed in the epitaxially grown films are mainly related to defects already present inside the poly-Si seed layers or defects generated at the poly-Si seed layer / epitaxial film interface.
- Contamination of poly-Si films is caused by out-diffusion of impurities from the poly-Si seed layer and the glass substrate. If AIC seed layers are epitaxially thickened the absorber layers contain a high level of Al.
- As an alternative way, poly-Si films prepared by epitaxial growth on LC seed layers show very large grains. However, the random orientation make epitaxy more difficult. In order to benefit from the large grain size, crystallographic orientation of the grains is important.

CHAPTER 6

Solar Cells

6.1 Introduction

Solar cell structures were prepared, in order to investigate the electrical quality of the Si absorber layers epitaxially grown by e-beam evaporation. The results are presented as wafer-based and glass-based solar cells (with and without a poly-Si seed layer). The standard Si absorber layer deposition conditions are defined as $T_s = 600$ °C, emission current (I_{em}) of 200 mA (corresponding to Si deposition rate of 100-200 nm/min), base pressure of $3-5 \times 10^{-9}$ mbar and a grounded substrate. The absorber layer thickness is about 2 μm with a doping level of $3-4 \times 10^{16}$ cm^{-3} . For wafer-based solar cells the influence of substrate temperature, Si deposition rate, base pressure and substrate bias on the solar cell characteristics are presented. Here, wafer substrates serve for assessing the influence of deposition parameters on solar cells independent of the influence that would be caused by the glass substrates and poly-Si seed layers. In addition, a comparison of Si(100)-based and Si(111)-based solar cells and the influence of hydrogen plasma passivation are discussed. For glass-based solar cells with a seed layer the influence of substrate temperature and hydrogen plasma passivation are discussed. Moreover, a comparison of solar cells by using poly-Si seed layers prepared by LC and AIC is given. In addition, solar cells prepared by solid phase crystallized Si deposited by e-beam evaporation are presented. Finally, the best solar cells of this study (wafer-based and glass-based with a seed layer) are presented and the evolution of open-circuit voltage (V_{oc}) is discussed.

6.2 Wafer-Based Solar Cells

The schematic sketch of the wafer-based solar cells (Figure 3.7.a) and the preparation steps of different layers are described in section 3.5. For comparison, solar cells have been prepared both on Si(100) and Si(111) wafers with and without hydrogen passivation. The corresponding solar cell characteristics are discussed.

6.2.1 Influence of Substrate Temperature

The influence of substrate temperature (T_s) was investigated for the range 450-700 °C by preparing solar cells on Si(100) and Si(111) wafers. A Si deposition rate of 140-150 nm/min, a base pressure of $3\text{-}5 \times 10^{-9}$ mbar and a grounded substrate were used

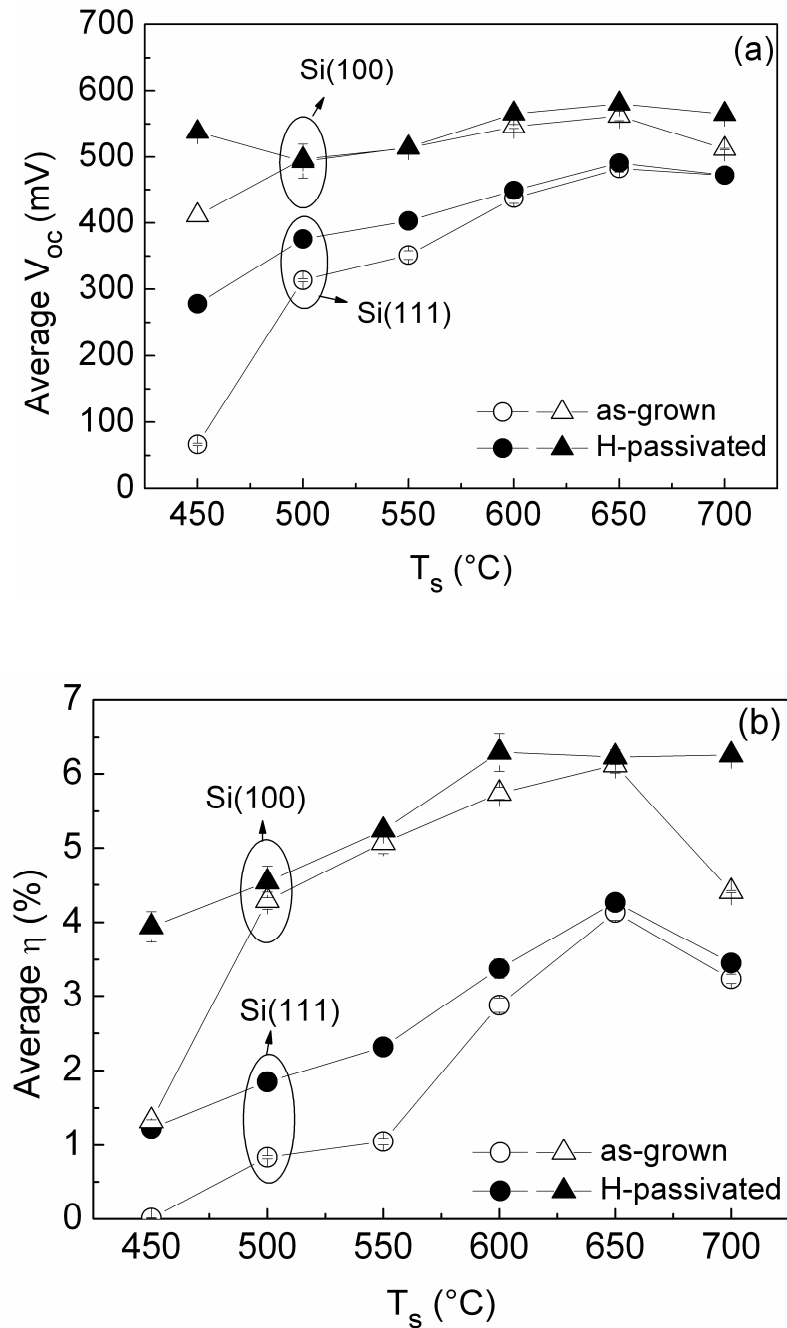


Figure 6.1 (a) Open-circuit voltage (V_{oc}) and (b) efficiency (η) versus substrate temperature (T_s) of Si(100)-based (Δ , \blacktriangle) (as-grown, H-passivated) and Si(111)-based (\circ , \bullet) (as-grown, H-passivated) solar cells.

during the depositions. After depositing Si absorber layers, half of each substrate was treated with hydrogen passivation as explained in section 3.4 while the other half served as an untreated reference. Finally, both pieces of the substrates were processed into complete solar cell structures and were analyzed by illuminated I-V measurements. Figure 6.1.a shows the open-circuit voltage (V_{oc}) and Figure 6.1.b illustrates the efficiency (η) of the solar cells as a function of T_s . Open symbols represent the results of the as-grown solar cells and solid symbols represent the results of hydrogen passivated solar cells.

For both Si(100)-based and Si(111)-based solar cells the efficiency increases with increasing T_s . This can be attributed to a decreasing number of extended defects observed towards higher T_s for example on Si(111) substrates. The increase of the efficiency is not only caused by an increase of V_{oc} but also by an increase of J_{sc} and FF of the solar cells towards higher T_s . For Si(100)-based solar cells (H-passivated) V_{oc} and the efficiency are almost constant if $T_s \geq 600$ °C. In comparison, the efficiency of Si(111)-based solar cells (H-passivated) increases until $T_s = 650$ °C. Increasing the substrate temperature to $T_s = 700$ °C results in a slight decrease in V_{oc} and the efficiency for both Si(100)-based and Si(111)-based as-grown solar cells. It was shown in Figure 4.8 that (111) epitaxial layers reveal a slightly higher extended defect density at 700 °C compared to for example 650 °C. This means that the increased contamination of the initial growth surface at $T_s = 700$ °C is responsible for the creation of additional defects and as a result the decrease in the device performance. Principally, contamination of the initial growth surface at high temperatures can be prevented by applying an in-situ removal of a protective native oxide layer [54]. However, this method is not compatible with the glass substrates which are used for the preparation of poly-Si solar cells.

Influence of the hydrogen passivation on V_{oc} and the efficiency of the Si(100)-based and Si(111)-based solar cells can be also seen in Figure 6.1.a and 6.1.b, respectively. In general, H-passivation improves V_{oc} , J_{sc} and therefore the efficiency of the solar cells. H-passivation improves the efficiency most effectively for the epitaxial layers grown at 450 °C. At this temperature, V_{oc} increases by 127 mV for Si(100)-based and by 211 mV for Si(111)-based solar cells. Similarly, J_{sc} increases from 6 mA/cm² to 14 mA/cm² for Si(100)-based and from 1 mA/cm² to 10 mA/cm² for Si(111)-based solar cells. Towards higher temperatures, H-passivation only slightly improves V_{oc} and the solar cell efficiency. In general, the improvement of V_{oc} after hydrogen passivation

compared to as-grown state is more pronounced for Si(111)-based solar cells compared to Si(100)-based solar cells. This could be explained as a result of more defective growth on Si(111) substrates and a corresponding passivation of the defects with hydrogen. For all substrate temperatures investigated, solar cells prepared on Si(100) substrates showed a higher V_{oc} and efficiency compared to that on Si(111). This result is in agreement with the findings of other researchers in the literature [52, 56]. It confirms also that better structural quality of the epitaxial Si films on Si(100) substrates compared to Si(111) substrates (demonstrated in chapter 4) results in a better solar cell performance.

For a better comparison of the influence of underlying crystallographic orientations, illuminated I-V characteristics of solar cells prepared on Si(100), Si(110) and Si(111) with epitaxial Si absorber layers deposited at $T_s = 600$ °C are plotted in Figure 6.2. Open symbols represent as-grown solar cells on different oriented substrates and solid triangles represent the hydrogen passivated Si(100)-based solar cell. Considering as-grown solar cells, it is seen that $\eta(\text{Si}(100)\text{-based}) > \eta(\text{Si}(110)\text{-based}) > \eta(\text{Si}(111)\text{-based})$. From this result, the influence of the underlying crystallographic orientation on the solar cell efficiency can be easily extracted. The solar cell efficiency of 5.8 % (with $V_{oc}=547$ mV) obtained on Si(100) wafer is a result of crystalline quality

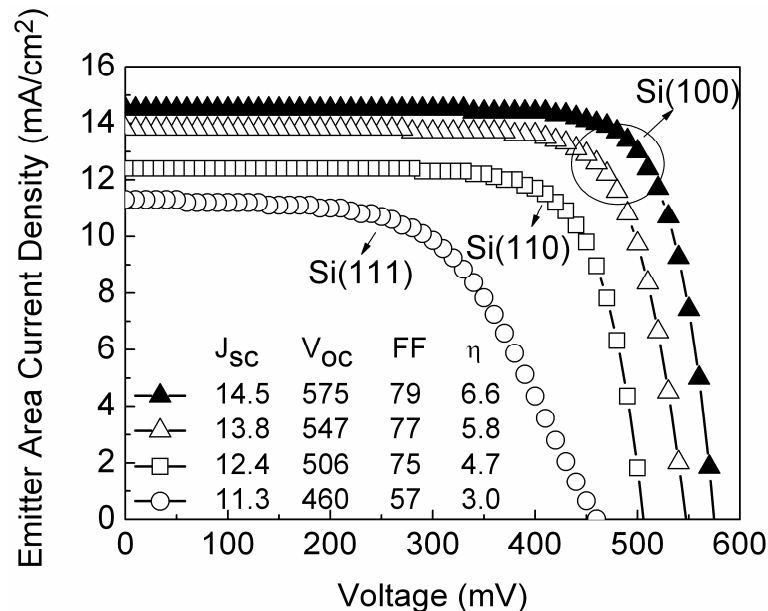


Figure 6.2 Illuminated I-V curve of solar cells prepared on Si(100): ▲(H-passivated), △(as-grown), Si(110): □(as-grown) and Si(111): ○(as-grown) wafers with epitaxial absorber layers grown at 600 °C .

of the epitaxial layers grown on these substrates. In comparison, solar cells prepared on Si(110) and Si(111) wafers reveal a conversion efficiency of 4.7 % (with $V_{oc}=506$ mV) and 3 % (with $V_{oc}=460$ mV), respectively. An increased extended defect density observed on non-(100) oriented substrates is expected to be responsible for the lower solar cell performance on these orientations. The lower FF of Si(111)-based solar cell is caused by a high series resistance due to device preparation failure. However, J_{sc} and V_{oc} of this solar cell can be still treated as the correct values. If hydrogen passivation is applied to the as-grown solar cell on Si(100) with an epitaxial absorber grown at 600 °C, V_{oc} was improved by 28 mV, whereas J_{sc} was improved by 0.7 mA/cm² and FF by 2 %. All these lead to the improvement of solar cell efficiency by 0.8 % and an efficiency of 6.6 %.

As a result of the influence of T_s investigation, it can be concluded that for the best solar cell performance $T_s \geq 600$ °C and (100) orientation of the substrate are beneficial. In addition, hydrogen passivation improves the material quality by passivating the dangling bond defects of the epitaxially grown absorber layer.

6.2.2 Influence of Si Deposition Rate

The influence of Si deposition rate (r_{Si}) was investigated by preparing solar cells on Si(100) substrates. r_{Si} was varied in the range of 40-540 nm/min. The substrate temperature was kept constant at 600 °C, since this resulted in the highest efficiency when combined with hydrogen passivation on Si(100)-based solar cells (section 6.2.1). This temperature is also compatible with the glass-based solar cells which will be presented in the next sections. A base pressure of $3-5 \times 10^{-9}$ mbar and a grounded substrate were used during the depositions. The doping level of the absorber layers was adjusted by increasing the effusion cell temperature towards higher r_{Si} (re-calculated from Figure 3.5). After depositing Si absorber layers, they were treated with hydrogen passivation. Finally, the layer stacks were processed into complete solar cell structures and were analyzed by illuminated I-V measurements. Figure 6.3 shows the normalized efficiency of the solar cells as a function of r_{Si} . The results were normalized to the standard deposition rate of at 185 nm/min. The absolute value of the efficiency in Fig. 6.3 differs from what was achieved in the previous section (Fig.6.1.a). We assume that this is caused by the use of different Si substrates with different doping levels. Solar cell

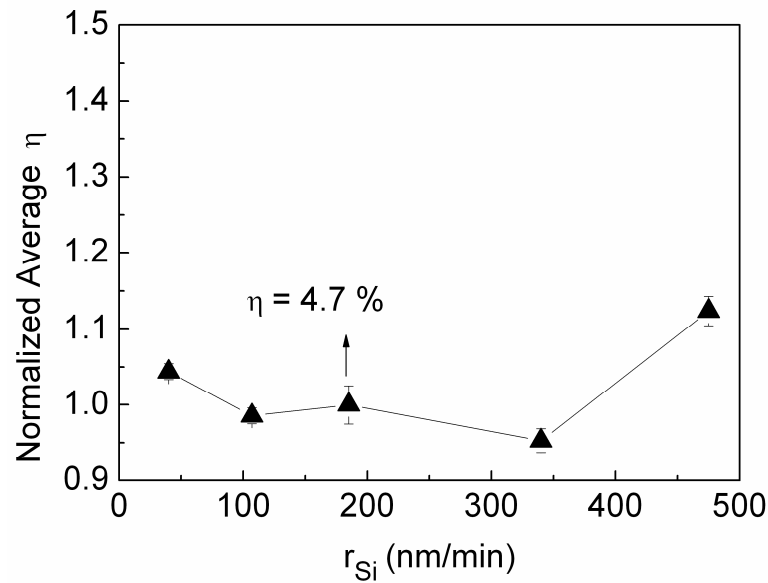


Figure 6.3 Normalized average efficiency (η) of Si(100)-based solar cells versus Si deposition rate (r_{Si}) with epitaxial Si absorber layers grown at 600 °C. (H-passivated)

efficiency is almost independent of the deposition rate up to 340 nm/min (considering error bars), and then slightly increases towards higher r_{Si} . The main contribution for the increase of the solar cell efficiency at higher rate results from an increase of mainly J_{sc} . That means a higher diffusion length and therefore an enhanced carrier collection are present in the epitaxial Si absorbers prepared at high deposition rates.

The influence of r_{Si} on the structural and electrical properties of the epitaxial absorber layers can be discussed by interplay of two defect generation mechanisms. On one hand, at higher r_{Si} , adatoms of Si will have less mean free time to find their positions in the lattice. This may result in the creation of vacancies and dislocation lines in the epitaxial Si films during the growth at high r_{Si} . However this behavior will be less important for $T_s \geq 600$ °C, since adatoms will have a higher mobility due to the substrate temperature. At such T_s values, higher r_{Si} is supposed to prevent incorporation of the impurities which are present in the non-ultra high vacuum environment of the e-beam evaporation and thereby improve the solar cell efficiency. In the literature studies about the evaluation of minority carrier diffusion length (L) reveal the influence of r_{Si} for different T_s [92, 93]. In accordance to the above mentioned defect mechanisms, epitaxial films grown at $T_s \leq 510$ °C resulted in a maximum L if r_{Si} is at about 300 nm/min. If $T_s \geq 550$ °C, higher deposition rates up to 800 nm/min resulted in an improvement of L

[93]. Within the time frame of this work, r_{Si} was investigated until 475 nm/min and it was found that high r_{Si} resulted in a slight increase in the solar cell efficiency.

6.2.3 Influence of Base Pressure

The influence of the base pressure (p) was investigated by preparing solar cells on Si(100) substrates. The base pressure was varied in the range of 3×10^{-9} (reference-without gas inlet) and 1×10^{-5} mbar by introducing laboratory air to the deposition

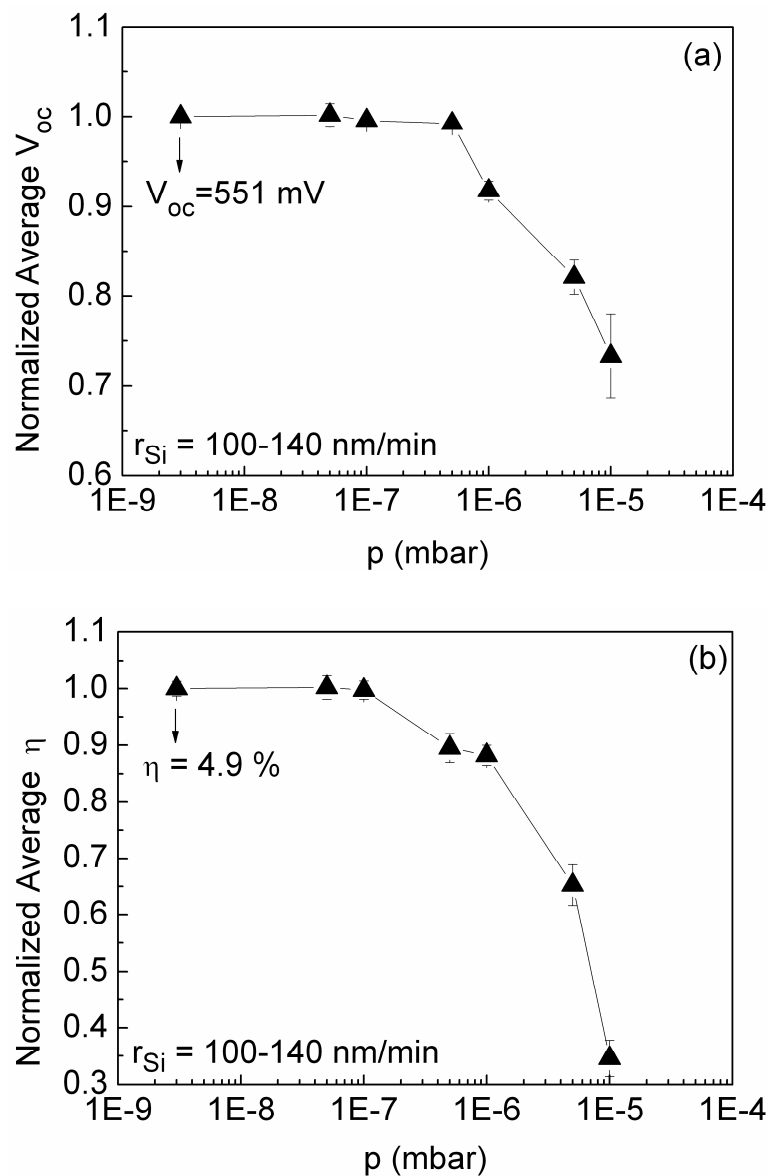


Figure 6.4 (a) Normalized open-circuit voltage (V_{oc}) and (b) efficiency (η) versus base pressure (p) of Si(100)-based solar cells. (H-passivated)

chamber through a needle valve in a controlled way. The other deposition parameters were as follows: $T_s = 600\text{ }^\circ\text{C}$, $r_{\text{Si}} = 100\text{-}140\text{ nm/min}$, and a grounded substrate. Absorber layers were hydrogen passivated and final solar cell structures were analyzed by illuminated I-V measurements. Figure 6.4.a shows the normalized V_{oc} and Figure 6.4.b illustrates normalized efficiency of the solar cells as a function of the base pressure. The results were normalized to the standard deposition at 3×10^{-9} mbar base pressure without gas inlet. For the base pressure range between 3×10^{-9} mbar and 5×10^{-7} mbar, the open circuit voltage of the solar cells is constant at about 550 mV. Similarly, the efficiency remains at 4.9 %. This means no critical change in the material quality is expected for this base pressure range. However for $p \geq 1 \times 10^{-6}$ mbar, the open circuit voltage and the efficiency of the solar cells decrease gradually. The decrease of efficiency at $p = 5 \times 10^{-7}$ mbar is caused by a lower absorber thickness ($1.7\text{ }\mu\text{m}$) and therefore a lower J_{sc} . Above $p = 1 \times 10^{-6}$ mbar all solar cell parameters (V_{oc} , J_{sc} , FF) decrease which lead to the decrease of the solar cell efficiency. This is caused by the higher level of background gases and the incorporation of the impurities inside the epitaxially growing films at high base pressures. Influences of increased partial pressures of O_2 , H_2O and N_2 at high base pressures were also investigated separately and presented in Annex I. Based on those results, an increased partial pressure of O_2 (up to 7×10^{-7} mbar) is found to be responsible for the lower solar cell efficiency at high base pressures.

At $p = 1 \times 10^{-5}$ mbar, in addition to the incorporation of impurities an n-type doping behavior of the absorber layer (Figure 4.18) leads to the lowest solar cell efficiency of 1.7 % with an open circuit voltage of 440 mV. The n-type doping is caused by the compensation of the boron atoms (intentional doping) by the residual oxygen (un-intentional doping). In this investigation the standard deposition rate of 100-140 nm/min was used. Knowing that the deposition rate has a great impact on the incorporation of impurities and thereby on the solar cell efficiency, using higher deposition rates the base pressure requirements of the e-beam system could be further tolerated. It is evident that the base pressure requirements determine the pumping time and so plays a critical role for determining the total costs of the Si solar cell production. The result of this investigation reveals that using a deposition rate of 100-140 nm/min, a base pressure of up to 1×10^{-6} mbar could be still tolerated without a decrease in the epitaxial layer quality and solar cell efficiency.

6.2.4 Influence of Substrate Bias

The influence of the substrate bias (V_s) on the solar cell characteristics of hydrogen passivated Si(100)-based solar cells was investigated. Substrate voltages of -50, -20, -10, 0, 20 V and a floating potential were applied. The other deposition parameters were as follows: $T_s = 600$ °C, $r_{Si} = 135$ -160 nm/min, and a base pressure of

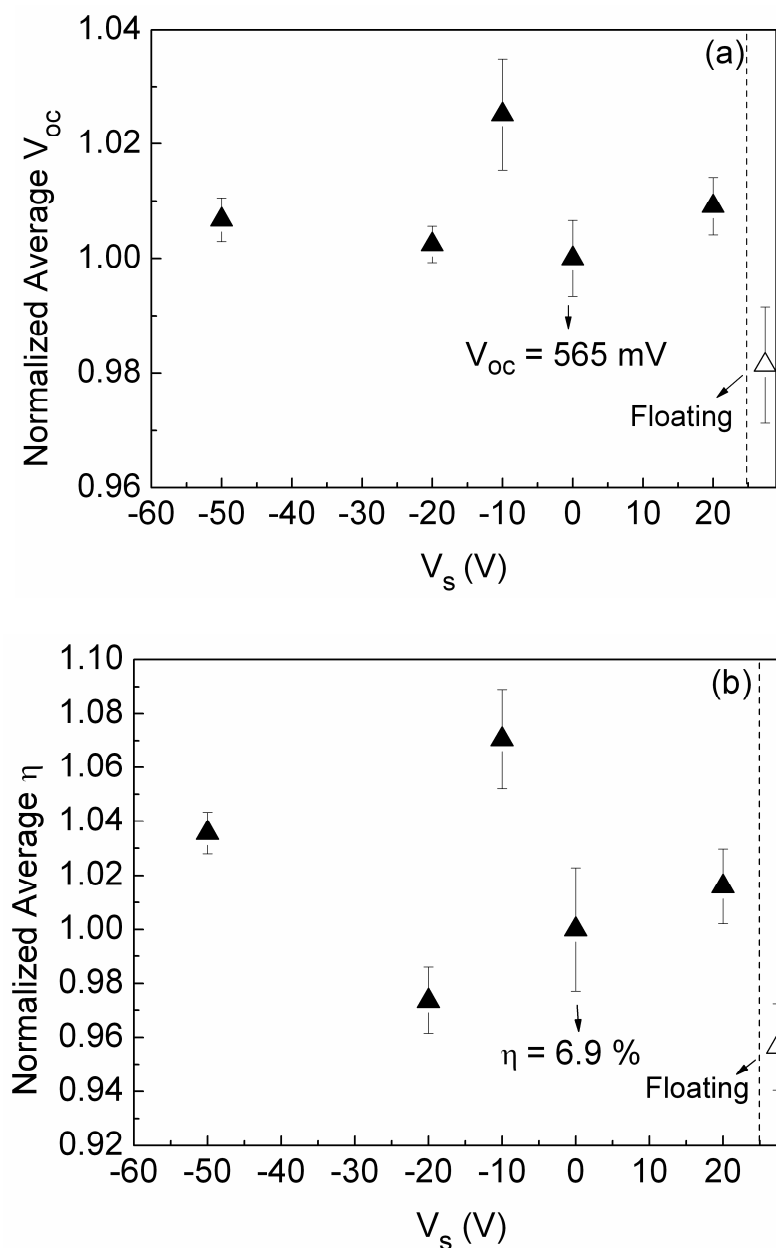


Figure 6.5 (a) Normalized average open circuit voltage (V_{oc}) and (b) normalized average efficiency (η) versus substrate bias (V_s) of Si(100)-based solar cells. (H-passivated)

about $3\text{-}5 \times 10^{-9}$ mbar. The absorber layers were doped to about 3×10^{16} cm^{-3} . The normalized V_{oc} and normalized efficiency of the solar cells are plotted in Figure 6.5.a and 6.5.b, respectively. The results are normalized to the standard deposition at 0 V substrate bias.

The change in the applied substrate bias does not result in a systematic change in V_{oc} and efficiency of the solar cells. A remarkable improvement of the solar cell parameters was observed for -10 V. At this substrate bias an average V_{oc} of 579 mV and a corresponding efficiency of 7.4 % were reached. The highest V_{oc} reached on the same substrate is 585 mV and results in an efficiency of 7.5 %. This is the highest efficiency and V_{oc} achieved in this study on Si(100) substrates with Si absorber layer deposited at $T_s = 600$ °C. In an identical deposition these results could be reproduced. Illuminated I-V curve of the best wafer-based solar cell will be presented in Figure 6.12 together with the best glass-based solar cell (with a seed layer) of this study. At negative substrate bias values, Si ions that are generated by the e-gun are accelerated towards the substrate and supply the growth surface additional energy. This additional energy is believed to promote the low temperature epitaxy. In the literature, where a specially designed post-ionization stage has been used for creating Si ions, -20 V has been recorded as an optimum substrate bias [52,54,56].

6.3 Glass-Based Solar Cells

Glass-based solar cell results will be distinguished by with or without a seed layer. Glass-based solar cells with a seed layer are prepared by epitaxial growth of absorber layers on poly-Si seed layers at $T_s = 600$ °C. On the other hand, glass-based solar cells without a seed layer are prepared by depositing an amorphous Si film directly on glass and applying a subsequent SPC at 600 °C.

6.3.1 Glass-Based Solar Cells (with a seed layer)

The schematic sketch of the glass-based solar cells (with a seed layer) is depicted in Figure 3.7.b and the preparation steps of different layers are described in section 3.5. For comparison, solar cells were prepared both on AIC and LC seed layers with and without hydrogen passivation.

6.3.1.1 Influence of Substrate Temperature

Glass-based solar cells were prepared by using epitaxially grown Si absorber layers on AIC seed layers on glass. In section 6.2, the influence of the deposition parameters on the solar cell characteristics of wafer-based solar cells was presented. In case of glass-based solar cells, the investigation of the deposition parameters become more critical due to the difficulties introduced by the use of glass substrate and a more defective nature of the poly-Si films. Similar to wafer-based solar cells, the influence of the substrate temperature on the solar cell characteristics of glass-based solar cells were investigated for 450-700 °C. For wafer-based solar cells, it was found that $T_s \geq 600$ °C is necessary for obtaining high V_{oc} and efficiency values. The results of the influence of T_s on as-grown glass-based solar cells are summarized in Table 6.1.

Table 6.1 Solar cell parameters (measured as-grown without hydrogen passivation) of glass-based solar cells deposited at different substrate temperatures (T_s). AIC seed layer was applied.

T_s (°C)	J_{sc} (mA/cm ²)	V_{oc} (mV)	FF (%)	η (%)
450	2.8	60	26	0
500	6.2	220	38	0.5
550	5.6	215	43	0.5
600	4.9	231	45	0.5

At $T_s = 450$ °C, despite the epitaxial growth achieved on the whole investigated area of the poly-Si seed layers, the solar cell results already indicate that these epitaxial absorbers were probably grown with a very high defect density which results in a very low solar cell efficiency. Increasing T_s to 500 °C, an increase in all solar cell parameters were observed. Further increase towards 600 °C resulted in an improvement in the cell V_{oc} from 220 mV to 231 mV and FF from 38 % to 45 %. However, J_{sc} of the solar cells slightly decreases towards higher T_s . The high level of Al detected in the poly-Si absorber layers epitaxially grown at $T_s = 600$ °C (Figure 5.10) is probably responsible for this result. Finally, the efficiency of the as-grown glass-based solar cells seems to be independent of temperature for $T_s \geq 500$ °C. Unlike wafer substrates, at higher substrate temperatures the out-diffusion of impurities from the poly-Si seed layer and/or from the

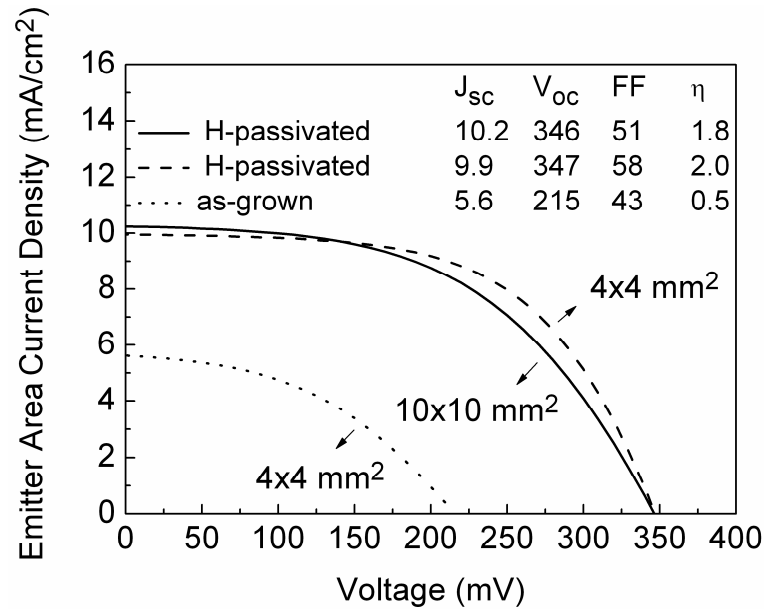


Figure 6.6 Illuminated I-V curves of glass-based solar cells, as-grown $4 \times 4 \text{ mm}^2$ (dotted line), H-passivated $4 \times 4 \text{ mm}^2$ (dashed line) and H-passivated $10 \times 10 \text{ mm}^2$ (solid line) with absorber layers epitaxially grown at $550 \text{ }^\circ\text{C}$.

glass substrate plays a critical role in determining the quality of the poly-Si absorber layers. Therefore implementation of a diffusion barrier between the glass and the poly-Si seed layer and an optimized heating profile are of crucial importance. The poly-Si films grown at $650 \text{ }^\circ\text{C}$ and $700 \text{ }^\circ\text{C}$ suffer from a high stress observed between the Si films and the glass substrate. The glass substrates used in this study are highly bended if $T_s \geq 650 \text{ }^\circ\text{C}$ and therefore they were broken during the solar cell processing. Therefore, the highest T_s compatible with Borofloat glass substrates is about $600 \text{ }^\circ\text{C}$.

The influence of hydrogen passivation on the glass-based solar cell efficiency was investigated. For this, the poly-Si absorber layer grown at $550 \text{ }^\circ\text{C}$ was treated with hydrogen passivation. Figure 6.6 shows illuminated I-V curves of as-grown (dotted line) and H-passivated (dashed-line) glass-based solar cells (with standard total area of $4 \times 4 \text{ mm}^2$). In addition, H-passivated solar cell with a total area of $10 \times 10 \text{ mm}^2$ (solid line) is also plotted. Applying H-passivation, all solar cell parameters of as-grown glass-based solar cell improve dramatically. Compared to as-grown poly-Si thin-film solar cell, V_{oc} increases by 132 mV , J_{sc} by 4.3 mA/cm^2 , FF by 14% and finally the efficiency by 1.5% . The as-grown solar cell suffers from a high series resistance (R_s) of about $15.4 \text{ } \Omega\text{cm}^2$ and a low parallel resistance (R_p) of about $204 \text{ } \Omega\text{cm}^2$. After hydrogen passivation, the solar cell exhibits a lower $R_s = 7.3 \text{ } \Omega\text{cm}^2$ and a higher $R_p = 1240 \text{ } \Omega\text{cm}^2$. For wafer-

based solar cells it was found that H-passivation improves solar cell characteristics only slightly for Si(100) substrate and in a higher amount for Si(111) substrate due to higher density of defects on Si(111). In case of glass-based solar cells, H-passivation is expected to passivate the defects of grains with different orientations and the defects at the grain boundaries and therefore lead to improved solar cell characteristics.

In order to study the homogeneity of the epitaxially grown poly-Si absorber layer, a solar cell with a total area of $10 \times 10 \text{ mm}^2$ (emitter area of 71.51 mm^2) (solid line) was prepared on the same substrate and compared to the solar cell with a total area of $4 \times 4 \text{ mm}^2$ (emitter area of 8.55 mm^2) (dashed line). It was found that both solar cells reveal very similar solar cell characteristics. The same V_{oc} values achieved for both solar cells clearly show the homogeneity of the absorber layer quality over larger areas. On the other hand, J_{sc} of $10 \times 10 \text{ mm}^2$ solar cell is slightly higher. FF of $10 \times 10 \text{ mm}^2$ solar cell decreases by 7 % as a results of lower R_p ($674 \text{ } \Omega\text{cm}^2$) and slightly higher R_s ($9.8 \text{ } \Omega\text{cm}^2$).

6.3.1.2 Glass-Based Solar Cells on AIC and LC Seed Layers

In order to compare the influence of different grain size and orientation of seed layers prepared by AIC and LC, solar cells were prepared on both types of poly-Si seed layers on glass. The poly-Si absorber layers were grown at $T_s = 600 \text{ } ^\circ\text{C}$ on AIC seed layer (with a thickness of about 200 nm) and on LC seed layer (with a thickness of about 400 nm) on glass. Figure 6.7 illustrates the comparison of hydrogen passivated glass-based solar cells prepared on an AIC seed layer (solid line) and a LC seed layer (dashed line). Both solar cells reveal a very similar solar cell efficiency. The results show that the solar cell with poly-Si absorber layer epitaxially grown on a LC seed layer reveals a remarkably higher V_{oc} .

On the other hand, the solar cell on LC seed layer reveals a slightly lower J_{sc} compared to the one on AIC seed layer. Figure 6.8 represents the external quantum efficiency (EQE) versus wavelength of glass-based solar cells on an AIC seed layer (solid line) and on a LC seed layer (dashed line) measured by using a bias light. The plots show that the spectral response of both solar cells are almost identical upto about $\lambda = 500 \text{ nm}$. In the longer wavelength range (above 500 nm) the EQE of solar cell on the AIC seed layer is slightly higher compared to the EQE of the solar cell on the LC seed

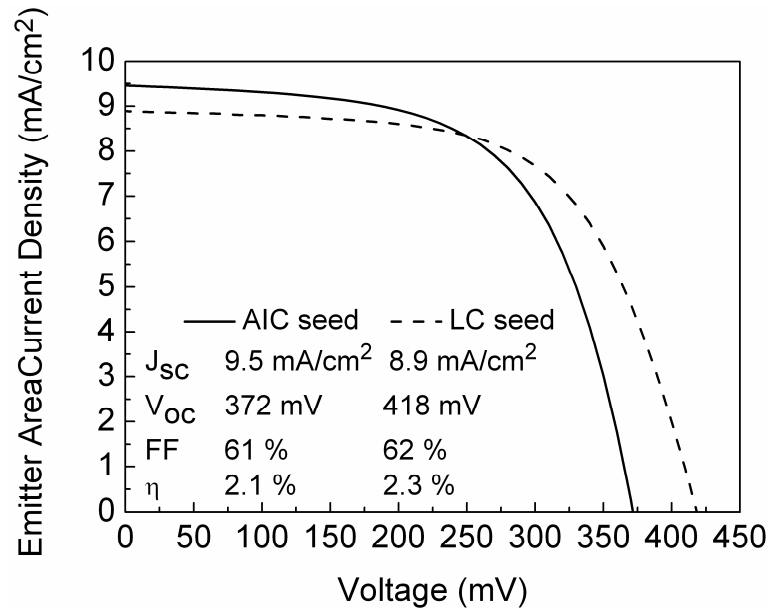


Figure 6.7 Illuminated I-V curves of glass-based solar cells on poly-Si seed layers prepared by AIC (solid line) and LC (dashed line) with poly-Si absorber layers grown at 600 °C.

layer. This is caused by the difference of the seed layer thicknesses. Since seed layers are highly doped layers, absorption of light inside the seed layers does not lead to a contribution in the charge carrier generation. Therefore thicker seed layers lead to a

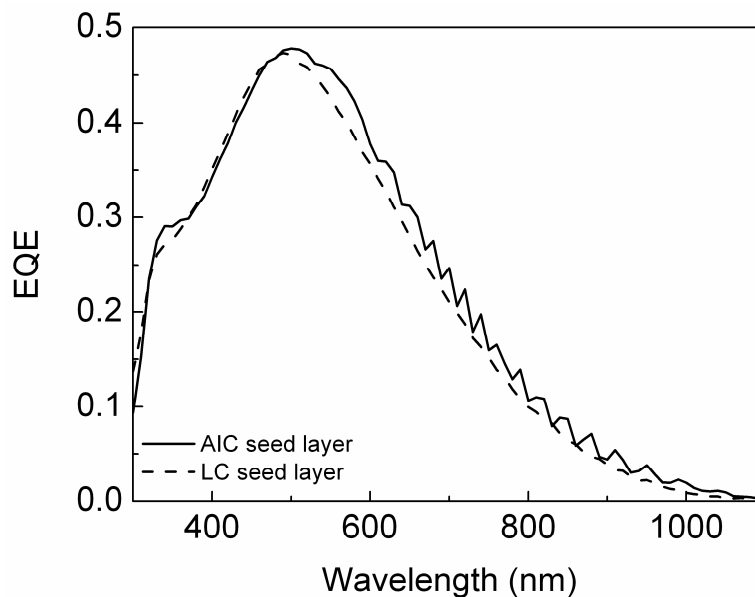


Figure 6.8 External Quantum Efficiency (EQE) versus wavelength of glass-based solar cells on poly-Si seed layers prepared by AIC (solid line) and LC (dashed line) with poly-Si absorber layers grown at 600 °C. The measurement was carried out with bias light.

decrease of EQE at longer wavelengths. The fluctuations of the EQE spectra of glass-based solar cells on an AIC seed layer at longer wavelengths correspond to the interference fringes. These fringes are not observed for glass-based solar cells on a LC seed layers. This is due to the roughness of absorber layer on LC seed layer which disturbs the coherence of the transmitted and reflected long wavelength light.

In the literature, layered laser crystallization of absorber layers on LC seed layers on glass was investigated [18]. In this process, an excimer laser was used during the growth of the poly-Si film to melt and recrystallize the layers of the poly-Si absorber film. Using this method, solar cell efficiencies of above 5 % [94] and V_{oc} up to 510 mV [89] were illustrated.

6.3.2 Glass-Based Solar Cells (without a seed layer)

Finally, glass-based solar cells (without a seed layer) were prepared by depositing Si layer stack ($n^+/p/p^+$) directly on glass at about 300 °C and by subsequent SPC at about 600 °C for several hours. The schematic sketch of the two solar cell structures that were used in this study are shown in Figure 6.9.a and 6.9.b. As glass substrates planar Borofloat with a thickness of 3.33 mm were used. Two types of emitter layers (a) n-type Si and (b) n-type SiN were deposited by PECVD. Prior to deposition of Si absorber layers, Si emitter layers were treated by HF 1% for 30 s and SiN emitter layers only with nitrogen blow. Using e-beam evaporation, p-type (about $1.5 \times 10^{16} \text{ cm}^{-3}$) absorber layers with a thickness of 1.5 μm and p^+ -type (about 10^{19} cm^{-3}) BSF layers with a thickness of 0.07 μm were deposited. The substrate temperature was held at about 300 °C. Si deposition rate of about 0.3 $\mu\text{m}/\text{min}$ was used. For comparison, one sample of each type was crystallized at the Helmholtz-Zentrum Berlin (HZB) at about 600 °C for several hours and one sample was crystallized at CSG Solar. All samples were treated by the same rapid thermal annealing and hydrogen-passivation at CSG Solar. After coating the top of the Si layers with resin, the contacts to the n^+ and p^+ layers were prepared by the innovative contacting scheme of CSG Solar [16, 95]. As these solar cells are illuminated in the superstrate configuration, the resin layer (with white color) acts as a back reflector. Finally, mini-modules of about 20 cm^2 were prepared by series connection of 8 solar cells. The mini-modules were characterized by I-V measurements under illumination.

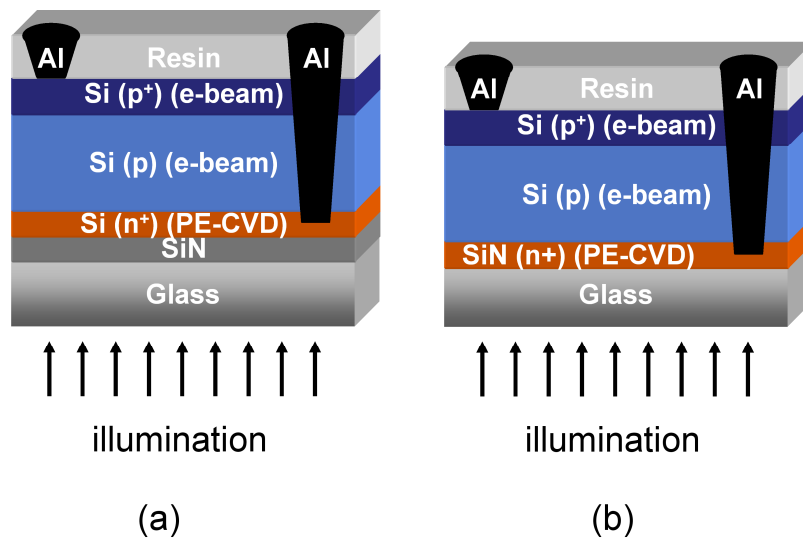


Figure 6.9 Schemes of glass-based solar cells (without a seed layer) with (a) n-type Si emitter layer and (b) n-type SiN emitter layer grown by PECVD. P-type Si absorber layers of about $1.5 \mu\text{m}$ and p⁺-type Si BSF layers of about $0.07 \mu\text{m}$ were deposited by e-beam evaporation. Device processing was performed by CSG Solar.

Figure 6.10 illustrates current-voltage characteristics of mini-modules prepared by combination of (a) n-type Si emitter layer, (b) doped SiN emitter layer deposited by PECVD and Si absorber layer grown by high-rate e-beam evaporation. Solid symbols represent the mini-module crystallized at HZB and open symbols represent that crystallized at CSG Solar for comparison. The mini-module prepared on Si emitter layer on planar glass (Figure 6.10.a) reach an efficiency of 5.7 % with a V_{oc} of 3.61 V, I_{sc} of 46.7 mA and FF of 68 %. The corresponding cell V_{oc} yields 452 mV and a current density J_{sc} of 18.5 mA/cm^2 . Recently, together with CSG Solar we have demonstrated even a higher mini-module efficiency of 6.7 % ($V_{oc}=475 \text{ mV}$, $J_{sc}= 20 \text{ mA/cm}^2$, FF=70 %) achieved by high-rate e-beam grown absorber layers ($0.6 \mu\text{m/min}$) [96]. The higher efficiency is obtained as a result of absorber layer thickness and doping level optimization. These results were achieved by using absorber layers grown by e-beam evaporation and is comparable to PECVD grown absorber layers on planar glass substrates [97]. Moreover, the incorporation of an optimized light trapping is shown to strongly increase the short-circuit current density and thereby enhance the solar cell efficiency by 20-30 % [97].

Both samples crystallized at HZB and CSG Solar reveal the same I-V characteristics (Figure 6.10.a). This result shows that efficiency is robust against

different crystallization tools and delays between deposition and crystallization. The results also demonstrate the compatibility of an e-beam grown absorber layer with PECVD grown emitter layer. On the other hand, it was found that a surface treatment of the emitter layer is of crucial importance for the cell performance. Using less

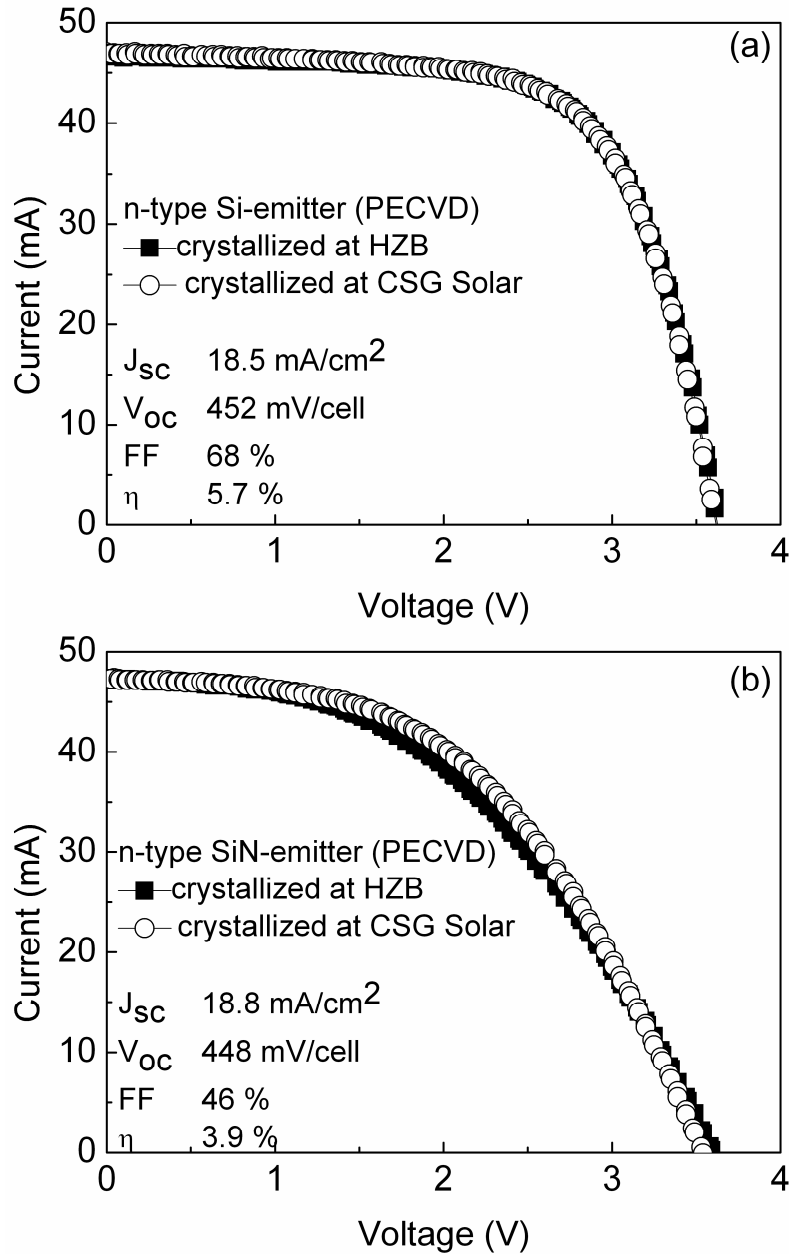


Figure 6.10 Illuminated I-V characteristics of mini-modules consisting of 8 cells each having an area of 2.523 cm² prepared by combination of (a) n-type Si emitter, (b) n-type SiN emitter grown by PECVD and absorber layer and BSF grown by high-rate e-beam evaporation.

concentrated HF solutions (1 %) and removing the solution from the surface as soon as it is hydrophobic was found to result in a higher device performance.

Furthermore, using PECVD grown n-type SiN emitter layers the mini-module had an efficiency of 3.9 % with a V_{oc} of 3.58 V, I_{sc} of 47.4 mA and FF of 46 % (Figure 6.10.b). The corresponding cell V_{oc} yields 448 mV and a current density J_{sc} of 18.8 mA/cm². When compared to the mini-module on PECVD grown Si emitter layer, V_{oc} and I_{sc} show that absorber layers grown by e-beam evaporation on both substrates have a similar material quality. The lower mini-module efficiency obtained on n-type SiN emitter layer is ascribed to a low FF which is caused by poor conductivity and corresponding high R_s introduced by the n-type SiN.

The EQE spectra measured on glass-based solar cells prepared with absorber layers grown by high-rate e-beam evaporation and subsequently solid phase crystallized on PECVD grown Si emitter (dashed line) and doped SiN emitter (solid line) are shown in Figure 6.11. Both samples reveal a typical EQE spectra shape. The fringes at the long wavelengths are attributed to the reflections on planar glass substrates. The maximum EQE of 0.82 (at 500 nm) and 0.77 (at 490 nm) were reached for the solar cells on a doped SiN emitter layer and that on a Si emitter layer, respectively. Strikingly, solar

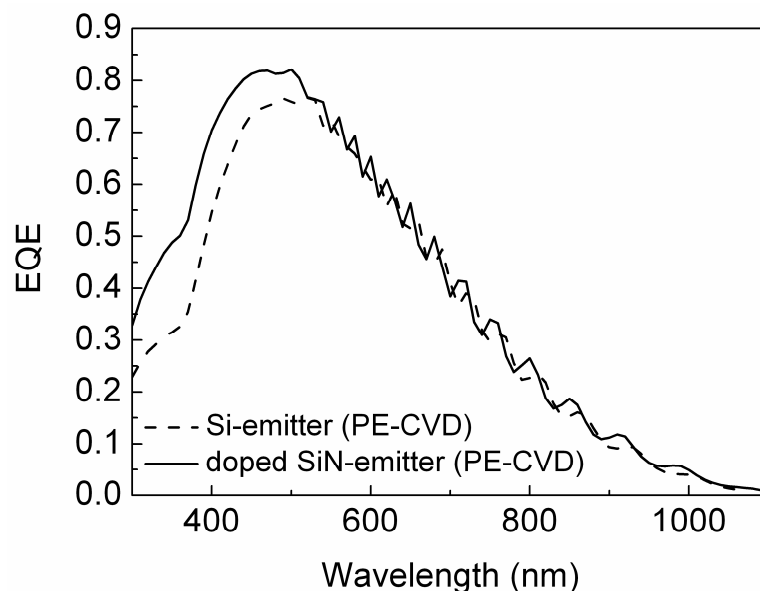


Figure 6.11 External Quantum Efficiency (EQE) versus wavelength of glass-based solar cells prepared with absorber layers grown by e-beam evaporation and subsequently solid phase crystallized on PECVD grown Si emitter (dashed line) and doped SiN emitter (solid line). The measurement was carried out with bias light.

cells prepared on PECVD grown doped SiN emitter reveal a higher collection in the blue wavelength range compared to the solar cells prepared on PECVD grown a-Si emitters. This is caused by the fact that an additional n^+ -Si layer (dead layer) is missing (see Figure 6.9). Applying an optimized light trapping scheme by for example texturing the glass substrate the spectral response can be further increased at longer wavelengths for the solar cells with Si absorber layers prepared by e-beam evaporation. Finally, the results show that e-beam evaporation can be used as an alternative low-temperature deposition technique for the growth of glass-based solar cells.

6.4 Evolution of Wafer-Based and Glass-Based Solar Cells (with a seed layer)

The current-voltage characteristic of the best wafer-based and glass-based (with a seed layer) solar cells are shown in Figure 6.12. The current density was calculated using the active area of the solar cell which is 7.44 mm^2 for the interdigitated contacting scheme used for the glass-based solar cell and 10.65 mm^2 for the mesa contacting scheme of the wafer-based solar cell. The active area was calculated by subtracting the emitter contact area from the emitter area. The absorber layers were grown at $600 \text{ }^\circ\text{C}$

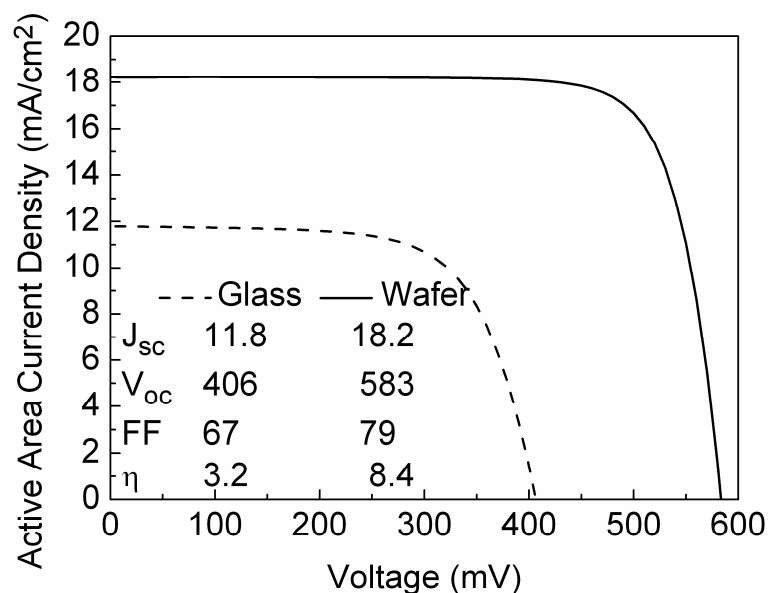


Figure 6.12 Illuminated I-V curves of best wafer-based (solid line) and best glass-based (with an AIC seed layer) (dashed line) solar cells with absorber layers grown at $600 \text{ }^\circ\text{C}$ (active area J_{sc} and η).

with a thickness of about 2.2 μm for glass-based and about 2 μm for the wafer-based solar cell. The deposition rate was about 140-160 nm/min and a substrate bias of -10 V was applied for both cells. Considering the glass-based solar cell, an active area J_{sc} of 11.8 mA/cm^2 was reached. Together with V_{oc} of 406 mV and FF of 67 % this has led to an active area efficiency of 3.2 %. The highest V_{oc} achieved on the same substrate yields 415 mV. The efficiency of 3.2 % is the highest published efficiency so far concerning glass-based solar cells with epitaxially grown low-temperature absorber layer on poly-Si seed layer prepared by AIC [98]. This result was achieved by the optimized growth conditions of e-beam evaporation together with the influence of hydrogen passivation. Prior to this work, the highest efficiency published was 2.2 % with a V_{oc} of 420 mV achieved by epitaxial growth of Si absorber layer by IAD [63]. Despite the encouraging wafer-based solar cell results that the earliest groups obtained (an efficiency of 13.1% (2 cm^2) with a 20 μm thick epitaxial layer), they could not succeed to demonstrate a glass-based solar cell exceeding an efficiency of 1 % [54].

The best wafer-based solar cell of this study reveals an active area efficiency of 8.4 % ($V_{\text{oc}} = 583 \text{ mV}$, J_{sc} of 18.2 mA/cm^2 , FF = 79 %) achieved with a 2 μm thick epitaxially grown absorber layer (Figure 6.12). The highest V_{oc} achieved on the same substrate yields 585 mV. In the literature, the theoretical limit of J_{sc} that can be reached for a 2 μm thick Si film (without light trapping) is given as 17 mA/cm^2 [3]. The short circuit current density that is reached on wafer-based solar cell is slightly higher than this theoretical limit. This is caused by a small contribution of the wafer substrate to carrier generation despite the choice of a highly-doped Si wafer substrate. The V_{oc} of 585 mV achieved by e-beam evaporation is still lower than the highest V_{oc} of 622 mV recorded with a wafer-based solar cell prepared by IAD [92]. Possible reasons for this difference can be counted as a better surface protection and an ultra-high vacuum environment of IAD and in addition higher doping level of the absorber layer (about 10^{17} cm^{-3}). In general, the best wafer-based solar cell prepared by e-beam evaporation illustrates the efficiency potential of a thin-film solar cell if an “ideal seed layer” is used and a high quality epitaxially grown absorber layer was prepared.

Figure 6.13 represents the external quantum efficiency measurements of the wafer-based and poly-Si seed layer coated glass-based solar cells of Figure 6.12. The wafer-based solar cell exhibits a high collection over the whole wavelength range investigated due to the high quality of epitaxial Si layers on (100) crystal orientation. In comparison, glass-based solar cell exhibits a lower collection of charge carriers. The shape of the

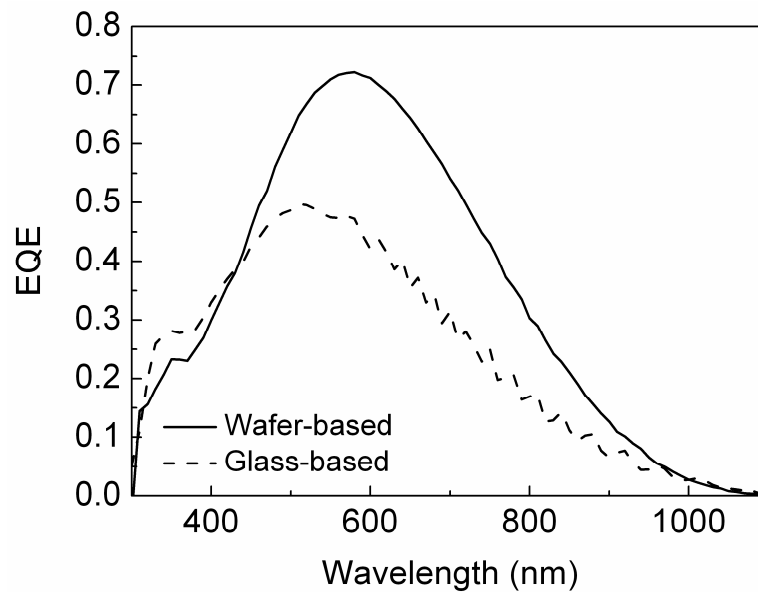


Figure 6.13 External Quantum Efficiency (EQE) versus wavelength of best wafer-based (solid line) and best glass-based (with a seed layer) (dashed line) solar cells with absorber layers grown at 600 °C. The measurement was carried out with bias light.

EQE and the poor response at infrared is typical for thin-film Si solar cells without light trapping. So far no real light trapping structures are implemented (except for the white reflector which was placed below the glass substrate for the measurement only). An efficient light trapping structure at the surface is very important. The implementation of a surface texture by for example plasma etching seems to be a suitable way to improve the light trapping of our glass-based solar cells. For the wafer-based solar cell, the maximum EQE of 0.72 was reached at 580 nm. In comparison, the glass-based solar cell on glass exhibits a maximum EQE of 0.50 at 510 nm. The peak wavelength clearly indicates that the solar cells are most sensitive to the blue-green light which is almost fully absorbed on the first pass through a 2 μm thick Si film.

The evolution of the V_{oc} of the glass-based solar cells (with a seed layer) prepared during this study is plotted in Figure 6.14. For selected data points emitter area efficiency of the solar cells are also indicated in the graph. The first data point represents an as-grown glass-based solar cell with a V_{oc} of 220 mV and an efficiency of 0.5 %. Applying first hydrogen plasma passivation experiments, V_{oc} of the glass-based solar cells could be improved to 270 mV. Later, optimization of e-beam evaporation parameters like an increased Si deposition rate initially from 100 nm/min up to 200 nm/min, an applied substrate bias of -10 V together with optimized hydrogen

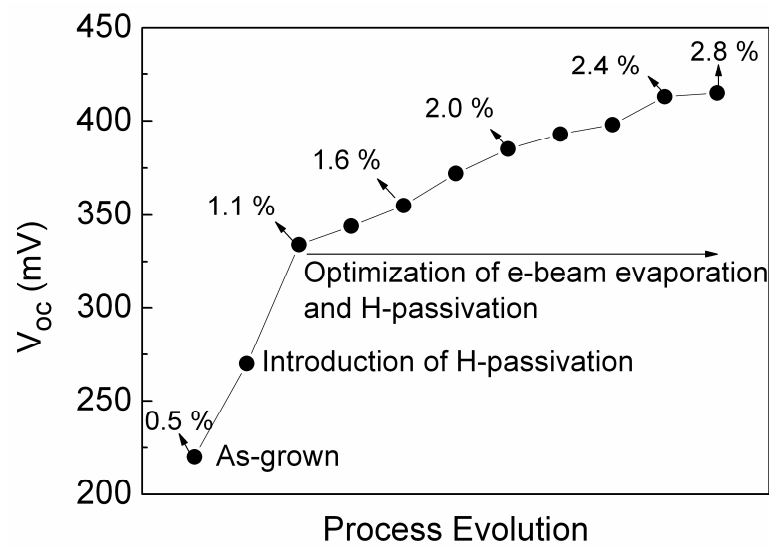


Figure 6.14 Evolution of V_{oc} of glass-based solar cells (with an AIC seed layer) prepared during this study with absorber layer deposited at 600 °C using e-beam evaporation. (corresponding emitter area efficiencies are given)

passivation conditions serve for improving the V_{oc} up to 406 mV which results in an emitter area efficiency of 2.8 % (3.2 % active area efficiency).

For further improvement of the glass-based solar cell efficiency, implementation of an intermediate layer between the glass and poly-Si seed layer to control out-diffusion of impurities is necessary. The first attempts of having an intermediate layer in the solar cell structure were performed by using SiN or ZnO. Especially after the successful demonstration of the temperature stability of ZnO layers when capped with a thin Si film [99], ZnO layers have gained a great interest for the production of polycrystalline Si thin film solar cells with transparent front contacts. Therefore, we have investigated the influence of the intermediate layers on the solar cell characteristics. However, very first solar cells exhibit a V_{oc} of 310 mV (efficiency 1.7 %) with SiN and 385 mV (efficiency 2 %) with ZnO intermediate layers. This shows no clear improvement of the glass-based solar cells when an intermediate layer was used. The main reason at the moment is probably the additional impurity segregation towards the absorber layer in case SiN or ZnO was used as an intermediate layer. This is caused by either not optimized deposition conditions of these layers or by not optimized heating profile of the glass-substrates in combination with these intermediate layers. By adaptation of the whole process sequence for an optimized intermediate layer, we are convinced that glass-based solar cell efficiencies can be further improved. In addition, decreasing the

defect density and implementation of an efficient light trapping are other important issues to reach better solar cell efficiencies.

6.5 Summary and Conclusions

In this chapter, solar cell characteristics of wafer-based and glass-based solar cells (with and without a seed layer) were explored. Influences of deposition parameters such as substrate temperature, deposition rate, base pressure and substrate bias on the solar cell efficiencies were investigated. Increasing T_s resulted in an improved V_{oc} of both wafer-based and glass-based solar cells. From wafer-based solar cell results, $T_s \geq 600$ °C and (100) oriented crystal surface were found to be optimum conditions for preparing high quality thin-film solar cells. Lower T_s results in a higher density of defects during epitaxial growth of the absorber layer. For the glass substrates, stress between the glass substrate and poly-Si film at higher T_s limits the substrate temperature at 600 °C. A major improvement of both types of solar cells were introduced by hydrogen-plasma passivation. This process improves all the solar cell parameters by passivating the defects. The highest V_{oc} reached on a wafer-based solar cell yields 585 mV and on a glass-based solar cell (with a seed layer) is 415 mV with an absorber layer grown at $T_s = 600$ °C. In case of SPC the highest V_{oc} yields 452 mV.

Comparing the structural and electrical analyses of the absorber layers on wafer substrates (Chapter 4) and the solar cell characteristics (this chapter), it was found that in most of the cases solar cell characteristics are more sensitive to the changes caused by the variations of the deposition parameters. Considering (100)-epitaxial layers, no extended defects could be detected (Figure 4.7) and no broadening of the Raman spectra FWHM have been observed for the whole temperature range investigated (Figure 4.10.a). However, solar cell results on Si(100) wafers show that there is a strong impact of T_s on the device efficiency. For (111)-epitaxial layers the results show a better agreement. Increasing T_s , extended defect density of (111)-epitaxial layers decreases (Figure 4.8), FWHM of the Raman spectra decreases (Figure 4.10.b) and the collection efficiency of the layers increases (Figure 4.14). All these results lead to the improvement of solar cell efficiency on Si(111) substrates towards higher T_s .

Considering the industrial application of an e-beam evaporation system for poly-Si thin-film production, deposition rate of Si and the base pressure requirements are the

two main parameters. It was found that the wafer-based solar cell efficiency increases slightly by increasing deposition rate of Si. This is caused by the incorporation of less impurity atoms at higher rates. Within the time frame of this work the deposition rate could be investigated up to 475 nm/min. Recently, we have also successfully demonstrated that Si absorber layers grown with 600 nm/min deposition rate of e-beam evaporation (after optimization of absorber layer thickness and doping layer) revealed comparable results obtained by PECVD growth. This result exhibits the potential of e-beam evaporation for industrial applications. This is mainly due to its advantages over PCVD, such as no-toxic gases, high growth rate and thereby lower production costs.

Another interesting point is the base pressure requirements of such a system. This work shows that the efficiency of the wafer-based solar cells remains unaffected until a base pressure of 1×10^{-6} mbar by introducing air to the deposition chamber. In Chapter 4, a critical base pressure was addressed at 1×10^{-5} mbar (for 100-140 nm/min), as the conductivity type of the absorber layer changes from p to n due to the high level of residual O_2 .

Considering glass-based solar cells, encouraging results were obtained. The homogeneity of the poly-Si absorber layers and the improvement of V_{oc} achieved by hydrogen-plasma passivation are the highlights of the glass-based solar cells. The quality of the glass-based solar cells is mainly controlled by the poly-Si seed layer imperfections, crystal orientation of the crystal grains and out-diffusion of impurities.

The main conclusions of the solar cell investigations can be summarized as follows:

- With increasing substrate temperature, the solar cell efficiency increases for both solar cells on Si(100) and Si(111) wafers. However, the efficiency of solar cells with (100) epitaxial layers is always higher compared to solar cells with (111) epitaxial layers (for each temperature). For the best solar cell performance substrate temperature should be at least 600 °C.
- Solar cell performance was improved by a hydrogen plasma treatment of the absorber layer.
- The base pressure of the e-beam evaporation system should be kept below 1×10^{-6} mbar for a deposition rate of 100-140 nm/min to maintain the solar cell performance.

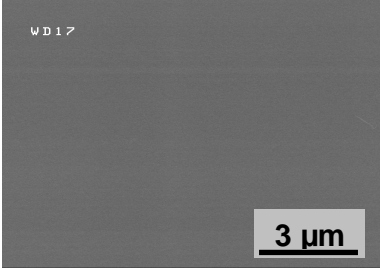
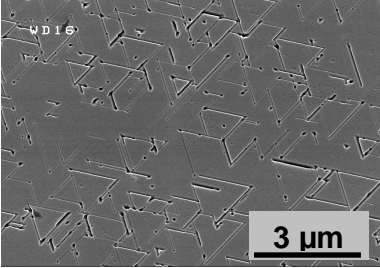
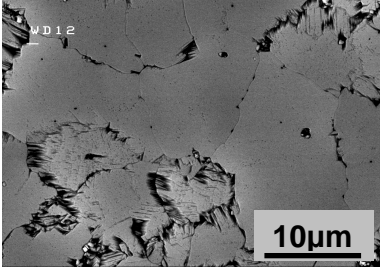
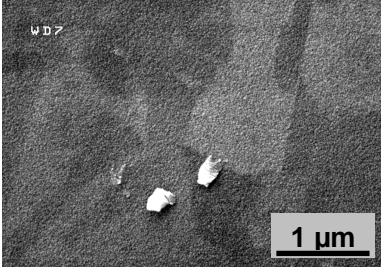
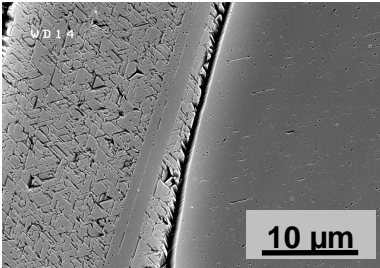
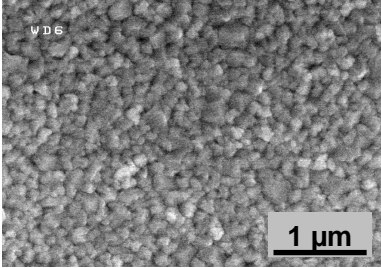
- Despite a large-grain size of glass-based solar cells prepared on seed layers, higher efficiency of the solar cells were obtained by small-grained absorber layers prepared by solid phase crystallization of a-Si deposited using e-beam evaporation.
- The best open circuit voltages achieved for different substrates are as follows:
 - 585 mV (on Si(100) wafer)
 - 415 mV (on AIC seed layer)
 - 418 mV (on LC seed layer)
 - 452 mV (SPC)

CHAPTER 7

Discussion

The subject of this thesis is the investigation of the structural and electrical properties of Si films epitaxially grown by e-beam evaporation on different substrates for the application in thin-film solar cells. Table 7.1 summarizes the results obtained in this study. The deposition of Si on mono-Si wafers with (100) and (111) orientations, poly-Si seed layer coated glass substrates and bare glass substrates allows the comparison of different film morphologies achieved by e-beam evaporation. Grain orientation has a great impact on the defect density on different substrates. Epitaxial growth of Si on Si(100) wafers gives the best structural and electrical properties. Using e-beam evaporation, V_{oc} of 585 mV could be reached using (100) epitaxial layers. However, considering a larger FWHM of Raman spectra and a lower mobility of holes in (100) epitaxial layers compared to bulk c-Si reveals that even (100) epitaxial films contain defects. Structural analysis like extended defect etching and Raman measurements on (100) epitaxial films are not sensitive enough to reflect the differences in the material. In comparison, (111) epitaxial layers reveal a higher extended defect density and a lower solar cell performance which shows that the quality of the epitaxial growth is strongly depended on the underlying crystallographic orientation. This influence is also clearly seen on poly-Si films prepared on glass substrates (with a seed layer) where non-(100)-oriented grains reveal a higher extended defect density compared to (100)-oriented grains. In addition to the crystallographic orientation also the substrate temperature (T_s) influences the solar cell performance. Higher T_s leads to higher solar cell efficiencies.

Hydrogen plasma treatment of the absorber layers increases the V_{oc} of the solar cells by passivating the defects. It was found that H-passivation is more effective for the Si films grown at lower substrate temperatures and on Si(111) wafers. Therefore, the highest V_{oc} achieved for H-passivated (100) epitaxial layers should not be considered only as an influence of H-passivation but also as an optimized deposition on these substrates. In general, the improvement of V_{oc} is about 20 mV for the wafer-based solar cells after H-passivation. In comparison, V_{oc} of glass-based solar cells could be improved by more than 200 mV after H-passivation. This is due to effective passivation of the grain boundaries in the poly-Si films.

		Wafer		Poly-Si on glass (with seed layer)	Poly-Si on glass (without seed layer)
		(100) epi layer	(111) epi layer		
Structural Properties		 <p>No extended defects ($T_s = 600\text{ }^\circ\text{C}$)</p>	 <p>Etch pit density $1 \times 10^8\text{ cm}^{-2}$ ($T_s = 600\text{ }^\circ\text{C}$)</p>	 <p>($T_s = 600\text{ }^\circ\text{C}$) (AIC) Grain size $\sim 5\text{-}10\text{ }\mu\text{m}$</p> <ul style="list-style-type: none"> Etch pit density $3.5 \times 10^8\text{ cm}^{-2}$ (near (100) grains) Etch pit density $\gg 10^8\text{ cm}^{-2}$ (near (111) grains) [5.3.3] 	 <p>($T_s = 300\text{ }^\circ\text{C} + \text{SPC @ } 600\text{ }^\circ\text{C}$)* Grain size $\sim 1\text{ }\mu\text{m}$</p>
		 <p>($T_s = 600\text{ }^\circ\text{C}$) (LC) Grain size $\sim 100\text{ }\mu\text{m}$</p> <ul style="list-style-type: none"> Etch pit density $\sim 10^8\text{ cm}^{-2}$ (near (100) grains) Etch pit density $\gg 10^8\text{ cm}^{-2}$ (near (111) grains) [5.4] 	 <p>($T_s = 600\text{ }^\circ\text{C} + \text{SPC @ } 600\text{ }^\circ\text{C}$)*</p> <p>* not defect etched</p>		
	[4.2]	[4.2]	[5.4]	[5.5]	

	Crystallinity	Fully crystalline ($T_s = 450-700\text{ }^\circ\text{C}$) [4.3]	Fully crystalline ($T_s = 450-700\text{ }^\circ\text{C}$) [4.3]	Fully crystalline ($T_s = 450-700\text{ }^\circ\text{C}$) [5.3.1]	Fully amorphous => Fully crystalline ($T_s = 300\text{ }^\circ\text{C}$) SPC @ $600\text{ }^\circ\text{C}$ Fully crystalline => Fully crystalline ($T_s = 600\text{ }^\circ\text{C}$) SPC @ $600\text{ }^\circ\text{C}$ [5.5]
	Contamination	[O] = $5 \times 10^{16}\text{ cm}^{-3}$ [N] = $1.5 \times 10^{16}\text{ cm}^{-3}$ [Al] < 10^{14} cm^{-3} [5.3.4]	-	[O] = $5 \times 10^{17}\text{ cm}^{-3}$ [N] = $3 \times 10^{16}\text{ cm}^{-3}$ [Al] = $9 \times 10^{17}\text{ cm}^{-3}$ [5.3.4]	[O] = $5 \times 10^{17}\text{ cm}^{-3}$ [N] = $2 \times 10^{16}\text{ cm}^{-3}$ [Al] = $4 \times 10^{15}\text{ cm}^{-3}$ (E-beam) [5.3.4] [O] ~ 10^{18} cm^{-3} [N] ~ $2-3 \times 10^{17}\text{ cm}^{-3}$ [Al] not published (PE-CVD) [100]
	EBIC collection efficiency	93 % (max. @ $1.3\text{ }\mu\text{m}$) [5.3.3]	82 % (max. @ $0.65\text{ }\mu\text{m}$) [5.3.3]	71 % (max. @ $0.65\text{ }\mu\text{m}$) [5.3.3]	-
Solar Cells	w/o HP	547 mV (5.8 %) [6.2.1]	440 mV (2.9 %) [6.2.1]	230 mV (0.5 %) [6.3.1]	220 mV (with RTP) (E-beam) 233 mV (1.75 %) (with RTP) (PE-CVD) [100]
	w HP	585 mV (7.5 %) [6.4]	460 mV (3.4 %) [6.2.1]	415 mV (2.8 %) (AIC) [6.4] 418 mV (2.3%) (LC) [6.3]	452 mV (5.7 %) (with RTP) (planar glass) (E-beam) [6.3.2] 492 mV (10.4%) (with RTP) (textured glass) (PE-CVD) [16]

Table 7.1 Summary of the investigations performed on (100) epitaxial layers, (111) epitaxial layers, poly-Si films grown on glass with and without seed layers. Numbers inside the brackets correspond to the related section of this thesis or the related reference.

With respect to the poly-Si growth on glass this work explores three different regimes: large grained material $\sim 10 \mu\text{m}$ grain size (epitaxy on AIC seed layers), larger grained material $\sim 100 \mu\text{m}$ (epitaxy on LC seed layers) and small grained material $\sim 1 \mu\text{m}$ (solid phase crystallization on glass). Experimental findings of this study show that so far the highest V_{oc} of 452 mV for a poly-Si thin-film solar cell was achieved by the small grained material where Si has been deposited on glass by e-beam evaporation at $T_s = 300 \text{ }^\circ\text{C}$ and subsequently crystallized at $600 \text{ }^\circ\text{C}$. In comparison, large grained materials prepared by epitaxial growth of Si on AIC and LC seed layers reveal a lower V_{oc} of about 415 and 418 mV, respectively. Principally, larger grained material has the potential to deliver higher V_{oc} due to a suppressed recombination of minority carriers at the grain boundaries. In the literature, it was shown experimentally that for a grain size $> 1 \mu\text{m}$, increasing grain size results in a higher V_{oc} and efficiency of the solar cells [101].

Figure 7.1 summarizes the experimental results of this work and the results of other groups about V_{oc} of thin-film solar cells as a function of grain size. Both experimental results of this work and literature data show a valley of V_{oc} with a minimum at about $7 \mu\text{m}$ grain size. Towards lower and higher grain sizes V_{oc} increases. In this study, the lower V_{oc} achieved so far on the large-grained material compared to small grained material can be explained by the existence of intra-grain defects. Additionally, a high level of Al observed in the absorber layers can be responsible for the lower solar cell performance in case AIC seed layers were used. Intra-grain defects lead to recombination of carriers in addition to the grain boundary recombination. Therefore they have a great impact on the cell performance. It was found that the formation of the intra-grain defects in the epitaxial films strongly depends on the seed layer imperfections and the grain orientation. About 60 % preferential (100) orientation of the AIC seed layer grains is beneficial for preparing high quality epitaxial films. However, smaller grains towards (111) orientation reveal a very high intra-grain defect density after epitaxy. In a similar way, despite the larger grain size of LC seed layers, the high fraction of (111) grain orientation leads to a high intra-grain defect density of the epitaxial Si films grown on such seed layers. Therefore, currently one can not benefit from the larger grain size of these seed layers unless the grain orientation or the intra-grain defect density is controlled. Also, (100) grains reveal extended defects caused by the imperfections of the seed layer. In the literature, V_{oc} of about 533 mV was achieved using AIC seed layers on alumina substrates and with a high-temperature epitaxy at

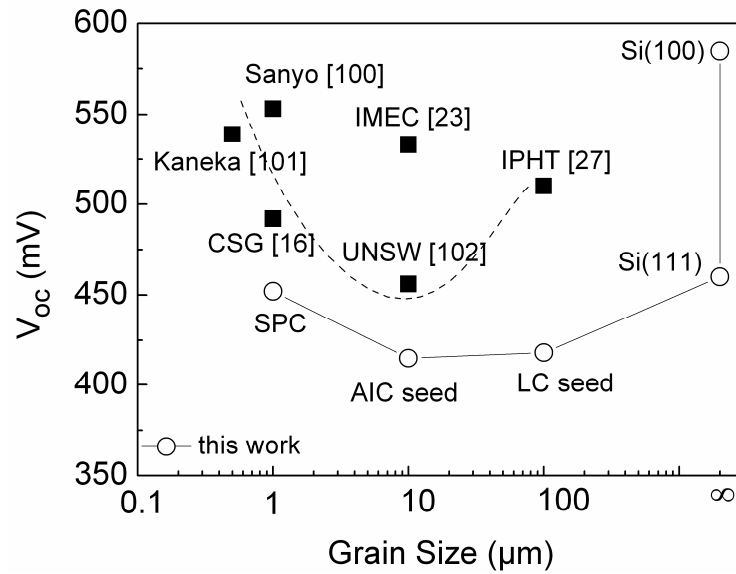


Figure 7.1 Open circuit voltage (V_{oc}) versus grain size of Si thin-film solar cells as obtained by different groups (solid symbols) and of this work (open symbols)

about 1100 °C by CVD [24]. Despite the encouraging solar cell results achieved, these samples also reveal a high density of intra-grain defects which show a high recombination activity [22]. Therefore, the improvement of the epitaxial growth quality on non-(100) grains as well as decreasing the intra-grain defect density of (100) grains should lead to improved solar cell results on large-grained poly-Si films.

CHAPTER 8

Conclusions and Outlook

In this work, the epitaxial growth of Si on mono-Si, poly-Si seed layers and directly on glass were investigated. Different material systems allow for comparison of grain size and orientation. It was found that both parameters are of great importance for the epitaxial growth of Si. Using (100)-wafers, it was shown that e-beam evaporation is a suitable method for preparing high-quality epitaxial layers even at low substrate temperatures once the substrate quality has been defined accordingly. High deposition rates of this method prevents the contamination of the epitaxial films and make the use of less stringent vacuum conditions possible. It also decreases the deposition time drastically. Depositing at high rates, however, preparation of thin doped layers becomes more critical. Principally, this can be solved by preparing low-doped absorber layers at high-rate and high-doped BSF layers at lower deposition rates.

Another critical parameter is the substrate temperature. It was found that higher substrate temperatures lead to higher solar cell efficiency of the wafer-based solar cells. However, using glass substrates temperatures above 600 °C are not applicable. Also, heating a large mass of glass at 600 °C seems to be an important issue for the production of poly-Si thin-film solar cells. Applying a more careful heating profile and a lower initial substrate temperature have the potential of controlling the impurity out-diffusion and depositing high-quality poly-Si films on glass.

The vacuum requirements of such an e-beam evaporation system were investigated in detail in this work. It was found that a base pressure of up to 1×10^{-6} mbar can be tolerated without degrading the solar cell performance. For an industrial application of such a system, the base pressure requirements are quite critical.

Concerning the application of low temperature epitaxy to solar cell mass production using the concept of epitaxial thickening of poly-Si seed layers, the results suggest that a high fraction of (100) crystal orientation, large grains size and defect-free seed layers are prerequisites. For preventing contamination of the growing films, implementation of a diffusion barrier between the glass and Si films is also necessary. Finally, appropriate light trapping is needed in order to increase the short circuit current density of the poly-Si thin-film solar cells.

ANNEX I

Role of Contamination for E-Beam Evaporation

Introduction

Today's most relevant deposition technique for Si thin-film photovoltaics is PECVD. This well established technique is widely used for the production of thin film solar cells based on a-Si:H and μ c-Si:H as well as for poly-Si. Some of the main drawbacks of this method include low deposition rates (0.5-2 nm/s) and the use of toxic and explosive gases. The low deposition rate directly controls the deposition time of the Si layers. In the literature, where PECVD is used for the Si deposition of poly-Si solar cells, absorber layer deposition time is plotted in a pie chart as one of the most time consuming process step of the total deposition cycle [95]. It was reported that the PECVD deposition tools represent fully half of the total capital cost of the factory. Consequently, the limitations of the PECVD method leads to a strong interest in finding alternative deposition techniques for further cost reduction of thin-film Si solar cell production.

E-beam evaporation of Si could be such an alternative as it provides several advantages over the conventional PECVD method. It allows for high deposition rates up to 1 μ m/min or even higher, that could reduce the deposition time dramatically. This high deposition rate also tolerates the non-ultra high vacuum conditions of the deposition system. Principally, the large area deposition of thin-films is possible by this method. Since this method is a physical vapour deposition, it includes no toxic gases and no plasma. For all these reasons, utilization of high rate e-beam evaporation method instead of PECVD has the potential for substantial cost reduction in industrial production of thin film silicon photovoltaics.

In the previous chapters, influence of the deposition parameters like substrate temperature, deposition rate, base pressure and substrate bias on the wafer-based and glass-based solar cells were examined. The influence of the base pressure on the wafer-based thin-film solar cells was investigated by introducing air to the deposition chamber and the results were presented in section 6.2.4. It was found that a base pressure of

1×10^{-6} mbar (for 100-140 nm/min) starts to worsen the solar cell characteristics. In this study, the influence of H₂O, O₂, and N₂ partial pressures on the wafer-based solar cell characteristics is investigated in detail.

Influence of H₂O, O₂ and N₂ Partial Pressures on Wafer-Based Solar Cells

Figure A.1 depicts the partial pressures of different elements which control the base pressure of the e-beam evaporation system. The spectra consist of different phases, namely stand-by partial pressures, sample transfer from load lock to the deposition chamber, and the final stage of pumping down in the growth chamber. During sample transfer, a sudden increase of partial pressures was observed which is followed by a fast pumping. The base pressure of the e-beam system was mainly controlled by H₂O, N₂ and H₂ partial pressures. During previous investigations, after introducing air to the main chamber the increase of the base pressure was mainly caused by N₂ and O₂ partial pressures. H₂O on the other hand, is the highest partial pressure controlling the base

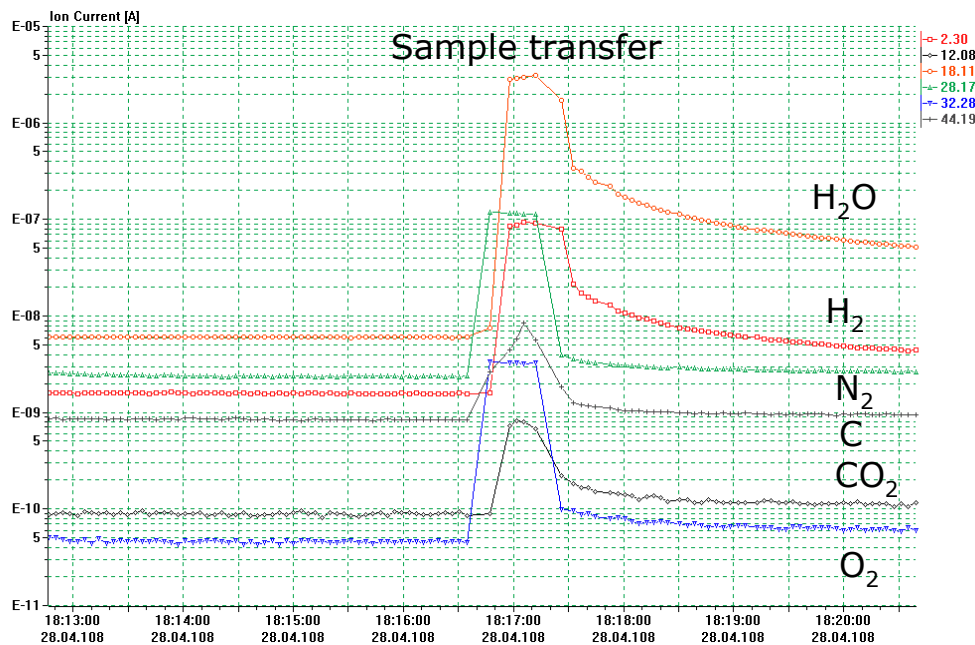


Figure A.1 Mass spectra showing the partial pressures of different elements controlling the base pressure of the e-beam system before and after sample holder transfer from load lock to the deposition chamber. The base pressure of the system is mainly controlled by H₂O, N₂ and H₂ partial pressures.

pressure in standard depositions (without any gas inlet). The high partial pressure of H₂O is expected to be introduced by the sample holder and the substrates.

In this section, the influence of partial pressures of H₂O, N₂ and O₂ on the device performance of solar cells prepared with epitaxial growth of Si absorbers on Si(100) wafer substrates at T_s = 600 °C is presented and discussed. All of the solar cells were treated by hydrogen-plasma passivation. Standard Si deposition rate of a 200 nm/min and a higher rate of 500 nm/min were used. The base pressure of the e-beam evaporation system was varied by means of gas inlet into the deposition system. As gases, nitrogen, oxygen and water vapour were used. The gases were introduced to the system through an UHV needle valve. The sources of nitrogen and oxygen were the gas bottles with 5N quality and the source for the water was frozen pure water. For the experiments, the gases were introduced into the deposition chamber just before beginning of the deposition and the level was adjusted using a total pressure measurement sensor and the mass spectra. The partial pressures of the gases were varied in the range of 1x10⁻⁶ mbar to 1x10⁻⁵ mbar.

Figure A.2 shows the plots of the solar cell efficiency as a function of base pressure for wafer-based solar cells prepared by H₂O, O₂ and N₂ inlet using a deposition rate of 500 nm/min (Figure A.2.a, open symbols) and 200 nm/min (Figure A.2.b, solid symbols). For comparison, a reference solar cell was prepared at 500 nm/min without gas inlet yields an average efficiency of about 6.7 % with a V_{oc} of 560 mV (marked as reference in Figure A.2).

Considering H₂O inlet at 1x10⁻⁶ mbar, the solar cell efficiency decreases to 6.4 % with a V_{oc} of 540 mV (for 500 nm/min) and to 5 % with a V_{oc} of 500 mV (for 200 nm/min). Although this level of base pressure is already far away from ultra-high vacuum conditions, results reveal that especially when a high deposition rate of 500 nm/min has been used the solar cell efficiency has only decreased by 4 % compared to the reference cell. When the partial pressure of H₂O was increased to 5x10⁻⁶ mbar the solar cell efficiency further decreases to 3.5 % (for 500 nm/min) and to 2.3 % (for 200 nm/min). At 1x10⁻⁵ mbar, the solar cell efficiency further decreases. The slight increase of the efficiency for 200 nm/min is expected to be caused by a thicker absorber layer of 2.2 μm and therefore a higher J_{sc}. Despite the fact that H₂O partial pressure determines the base pressure of the e-beam system, solar cell efficiency is only effected if p ≥ 1x10⁻⁶ mbar.

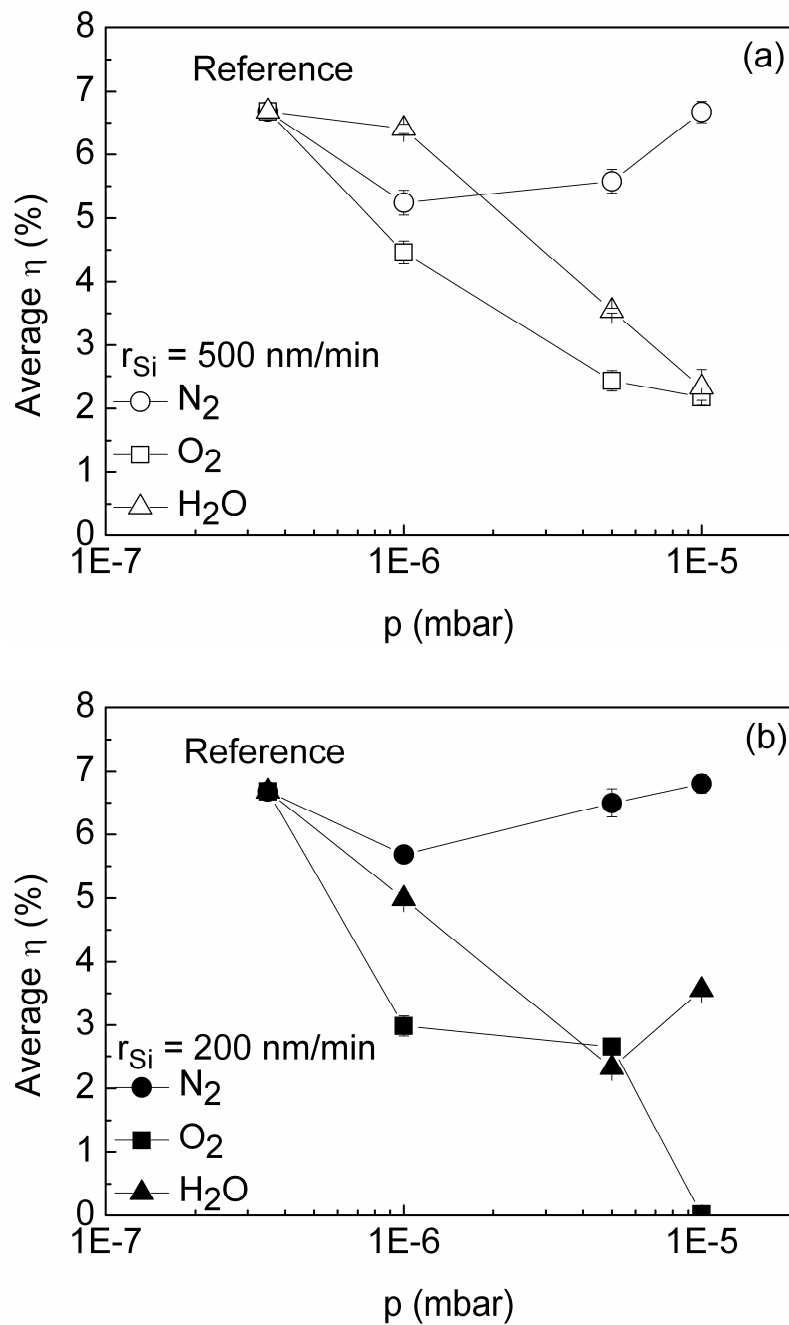


Figure A.2 The efficiency of solar cells on Si(100) wafers prepared by H₂O (Δ, \blacktriangle), O₂ (\square, \blacksquare) and N₂ (\circ, \bullet) inlet for a pressure range of 1×10^{-6} mbar to 1×10^{-5} mbar with Si deposition rates of 500 nm/min (a) and 200 nm/min (b).

Now we consider the case when O₂ was introduced to the deposition chamber. At 1×10^{-6} mbar solar cell efficiencies decreases to 4.5 % with a V_{oc} of 453 mV (for 500 nm/min) and to 3 % with a V_{oc} of 386 mV (for 200 nm/min) compared to 6.7 % efficiency of the reference cell. Higher Si deposition rate prevents incorporation of

impurities inside the growing Si film and therefore results in a higher solar cell efficiency compared to the lower rate. Despite the high deposition rate of 500 nm/min, solar cell efficiency decreases by about 33 % in comparison to the reference cell. This shows oxygen as an impurity degrades the device efficiency significantly. At higher base pressures the efficiency decreases even further. The concentration of incorporated oxygen atoms has been measured by SIMS. In Figure A.3 normalized efficiency of the solar cells prepared at 200 nm/min versus the concentration of oxygen is plotted. The reference solar cell prepared without a gas inlet reveals an oxygen concentration of $6 \times 10^{16} \text{ cm}^{-3}$. This level of oxygen has almost no influence on the device performance and reveals the quality of Si films grown by e-beam evaporation. In the literature, using Cz Si wafer solar cells, it has been established that oxygen can be present at concentration levels up to several 10^{18} cm^{-3} [105]. If the partial pressure of oxygen was increased to $1 \times 10^{-6} \text{ mbar}$, the concentration of incorporated oxygen yields $2 \times 10^{19} \text{ cm}^{-3}$ which causes to a decrease of 53 % in the efficiency. Towards higher pressure levels, concentration of incorporated oxygen increases up to $4 \times 10^{21} \text{ cm}^{-3}$. Oxygen is known to create complexes with boron and also acts as a donor. Therefore oxygen leads to a compensation of the absorber layer doping. As a conclusion, incorporation of oxygen in the epitaxially growing Si films is hazardous and should be prevented.

Finally, we consider N_2 inlet experiments. At $1 \times 10^{-6} \text{ mbar}$, solar cell efficiencies

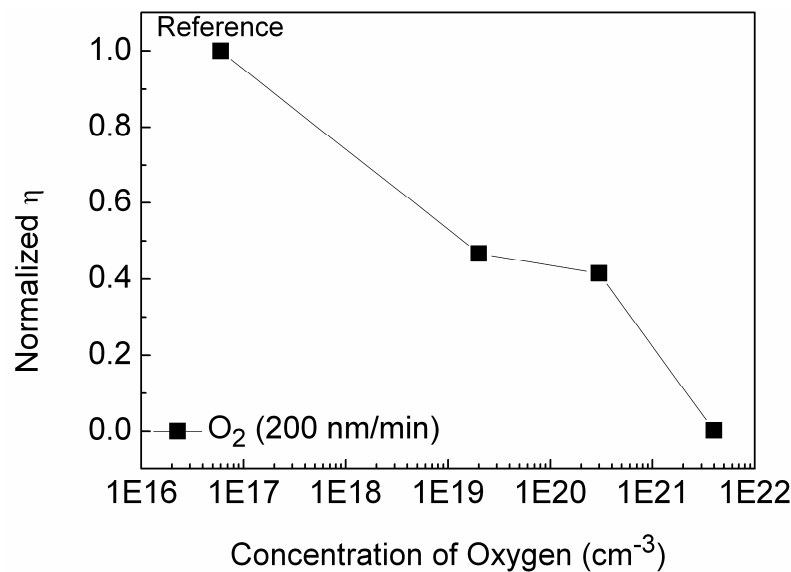


Figure A.3 Normalized efficiency of solar cells on Si(100) wafers prepared by O_2 inlet in a pressure range of $1 \times 10^{-6} \text{ mbar}$ to $1 \times 10^{-5} \text{ mbar}$ with Si deposition rate of 200 nm/min versus the concentration of oxygen measured by SIMS.

of 5.7 % (for 200 nm/min) and 5.2 % (for 500 nm/min) are recorded. This level is lower compared to the reference solar cell efficiency of 6.7 %. However, towards higher base pressures determined by N_2 the solar cell efficiency increases. The increase of efficiency towards higher base pressures is determined by a higher J_{sc} obtained although the film thickness has been kept constant. Unlike the other results, lower Si deposition rate results in a higher solar cell efficiency. This is expected due to a higher level of incorporated nitrogen in the epitaxially growing Si film. In the literature positive influence of nitrogen incorporation during crystal growth was discussed. In microelectronics, nitridation of the Si wafer surface were used to decrease the interface trap state density and thereby increase the quality of metal-oxide-semiconductor devices. In order to reveal the role of nitrogen during Si thin-film growth further investigations are necessary (see author patent).

The base pressure investigation results reveal that relatively high levels of base pressures can be tolerated during the epitaxial growth of the Si absorber layers by e-beam evaporation. Possibility of using high deposition rates serve for controlling the incorporation of the impurities inside the growing film as well it dramatically lowers the deposition time. Considering a deposition rate of 500 nm/min it would take only 4 minutes to deposit 2 μm thick Si absorber layers. These results illustrate well the industrial compatibility of the e-beam evaporation system.

Summary

These results reveal that O_2 is the most dangerous impurity which degrades the solar cell efficiency if present at high base pressures. H_2O on the other hand can be still tolerated until 1×10^{-6} mbar by using a high rate deposition (e.g. 500 nm/min). The influence of N_2 is rather more complicated and needs further investigations in order to reveal the mechanism behind the increasing solar cell efficiency towards higher N_2 partial pressures.

List of Abbreviations

AIC	Aluminum-Induced-Crystallization
a-Si	amorphous-Si
a-Si:H	hydrogenated amorphous-Si
BSF	Back Surface Field
CMP	Chemical Mechanical Polishing
CSG	Crystalline Silicon on Glass
C-V	Capacitance-Voltage
CVD	Chemical Vapor Deposition
CZ	Czochralski
E-beam	Electron-beam
EBIC	Electron Beam Induced Current
EBSD	Electron Back Scatter Diffraction
ECR-CVD	Electron-Cyclotron-Resonance CVD
EQE	External Quantum Efficiency
FIB	Focused Ion Beam
FF	Fill Factor
FWHM	Full Width at Half Maximum
FZ	Floatzone
HW-CVD	Hot-wire CVD
I_{em}	Emission current
IAD	Ion Assisted Deposition
IMEC	Interuniversity Microelectronics Centre
I-V	Current-Voltage
J_{sc}	Short circuit current density
LBIC	Laser Beam Induced Current
LC	Laser Crystallization
LLC	Layered Laser Crystallization
MBE	Molecular-Beam-Epitaxy
mono-Si	monocrystalline-Silicon
multi-Si	multicrystalline-Silicon

$\mu\text{c-Si}$	microcrystalline-Si
η	Solar cell conversion efficiency
PE-CVD	Plasma Enhanced Chemical Vapor Deposition
poly-Si	polycrystalline-Silicon
QE	Quantum Efficiency
R_p	parallel resistance
R_s	series resistance
r_{Si}	Si deposition rate
RTA	Rapid Thermal Annealing
SEM	Scanning Electron Microscopy
Si	Silicon
SIMS	Secondary Ion Mass Spectroscopy
SPC	Solid Phase Crystallization
SR	Spectral Response
TEM	Transmission Electron Microscopy
TCO	Transparent Conductive Oxide
V_{oc}	Open circuit voltage

References

- 1 Renewables 2010 Global Status Report (http://www.ren21.net / Portals / 97 /documents/GSR/REN21_GSR_2010_full_revised%20Sept2010.pdf).
- 2 M. A. Green, K. Emery, Y. Hishikawa, W. Warta, E. D. Dunlop, “Solar cell efficiency tables (version 38)”, *Progress in Photovoltaics: Research and Applications*, **19**, 565-572 (2011).
- 3 R. Brendel, “Thin-film crystalline silicon solar cells physics and technology”, Wiley-Vch GmbH and Co. KGaA, 20 (2003).
- 4 J. Zhao, A. Wang, S. R. Wenham, M. A. Green, “21.5 % efficient 47 μm thin layer silicon cells ”, *Proceedings of the 13th European Photovoltaic Solar Energy Conference*, Nice, France, 1566-1569 (1995).
- 5 C. Berge, R. Bergmann, T. J. Rinke, J. H. Werner, “Monocrystalline silicon thin-film solar cells by layer transfer”, *Proceedings of 17th European Photovoltaic Solar Energy Conference*, Munich, Germany, 1277-1281 (2001).
- 6 K. Feldrap, R. Horbelt, R. Auer, R. Brendel, “Thin-film (25.5 μm) solar cells from layer transfer using porous silicon with 32.7 mA/cm² short-circuit current density”, *Progress in Photovoltaics*, **11**, 105-112 (2003).
- 7 R. Brendel, “Thin-film crystalline silicon mini-modules using porous Si for layer transfer”, *Solar Energy*, **77**, 6, 969-982 (2004).
- 8 R.B. Bergmann, T.J. Rinke, C. Berge, J. Schmidt, J.H. Werner, “Advances in monocrystalline Si thin-film solar cells by layer transfer”, *Technical Digest PVSEC-12*, Korea, 11–15 (2001).
- 9 M. Kerr, M. Stocks, D. Gordeev, N. Tohill, P. Mackey, “Latest production developments in Sliver Technology”, *Proceedings of 21st European Photovoltaic Solar Energy Conference*, Dresden, 664-667 (2006).
- 10 D. L. Staebler, C. R. Wronski, “Reversible conductivity changes in discharge-produced amorphous Si”, *Applied Physics Letters*, **31**, 292 (1977).
- 11 L. L. Kazmerski, “Solar photovoltaics R&D at the tipping point: A 2005 technology overview”, *Journal of Electron Spectroscopy and Related Phenomena*, **150**, 105-135 (2006).

- 12 S. Benagli, D. Borrelo, E. Vallat-Sauvain, J. Meier, U. Kroll, J. Hoetzel, J. Spitznagel, J. Steinhauser, L. Castens, Y. Djeridane, "High-efficiency amorphous silicon devices on LPCVD-ZNO TCO prepared in industrial KAI-M R&D reactor", *Proceedings of the 24th European Photovoltaic Solar Energy Conference*, Hamburg, Germany 2293-2298 (2009).
- 13 H. Keppner, J. Meier, P. Torres, D. Fischer, A. Slah, "Microcrystalline silicon and micromorph tandem solar cells", *Applied Physics A*, **69**, 169 (1999).
- 14 B. Rech, T. Roschek, J. Mueller, S. Wieder, H. Wagner, "Amorphous and microcrystalline silicon solar cells prepared at high deposition rates using RF (13.56 MHz) plasma excitation frequencies", *Solar Energy Materials and Solar Cells*, **66**, 267 (2001).
- 15 J. Mueller, B. Rech, J. Springer, M. Vanecek, "TCO and light trapping in silicon thin film solar cells", *Solar Energy*, **77**, 917 (2004).
- 16 M.J. Keevers, T.L. Young, U. Schubert, M.A. Green, "10 % efficient CSG minimodules", *Proceedings of 22nd European Photovoltaic Solar Energy Conference*, Milan, 1783-1790 (2007).
- 17 O. Nast, T. Puzzer, L.M. Koschier, A.B. Sproul, S.R. Wenham, "Aluminum-induced crystallization of amorphous silicon on glass substrates above and below the eutectic temperature", *Applied Physics Letters*, **73**, 3214 (1998).
- 18 G. Andrae, J. Bergmann, F. Falk, E. Ose, N.D. Sinh, "A new technology for crystalline silicon thin film solar cells on glass based on laser crystallization", *Proceeding of 28th IEEE Photovoltaic Specialists Conference*, 217-220 (2000).
- 19 P.C. van der Wilt, A.M. Chitu, U.J. Chung, A.B. Limanov, James S. Im, "Surface-orientation-controlled and defect-free single-crystal Si regions on glass substrates for TFTs", *Proceedings of International Display Manufacturing Conference 2007*, 18-20 (2007).
- 20 M. Weizman, C. Klimm, M. Nittel, M. Kastner, C. Hernandez, N. H. Nickel, T. Sontheimer, B. Rech, "Formation of a laser-crystallized silicon seed layer for polycrystalline thin film solar cells", *Proceedings of 25th European Photovoltaic Solar Energy Conference/5th World Conference on Photovoltaic Energy Conversion*, Valencia, 2828-2831 (2010).

- 21 I. Gordon, D. Van Gestel, K. Van Nieuwenhuysen, L. Carnel, G. Beaucarne, J. Poortmans, “Thin-film polycrystalline silicon solar cells on ceramic substrates by aluminium-induced crystallization”, *Thin Solid Films*, **487**, 1-2, 113-117 (2005).
- 22 D. Van Gestel, M.J. Romero, I. Gordon, L. Carnel, J. D.Haen, G. Beaucarne, M. Al-Jassim, and J. Poortmans, “Electrical activity of intragrain defects in polycrystalline silicon layers obtained by aluminum-induced crystallization and epitaxy”, *Applied Physics Letters*, **90**, 092103 (2007).
- 23 L. Carnel, I. Gordon, D. Van Gestel, K. Van Nieuwenhuysen, G. Agostinelli, G. Beaucarne, J. Poortmans, “Thin-film polycrystalline silicon solar cells on ceramic substrates with a V_{oc} above 500 mV”, *Thin Solid Films*, **21-25**, 511-512 (2006).
- 24 Y. Qiu, O. Kunz, S. Venkatachalam, D. Van Gestel, R. Egan, I. Gordon, J. Poortmans, “8.5% Efficiency for Thin-Film Polycrystalline Silicon Solar Cells: A Study of Hydrogen Plasma Passivation”, *Proceedings of 25th European Photovoltaic Solar Energy Conference*, Valencia, Spain, 3633-3637 (2010).
- 25 Website of Schott AG, Germany, “thermalexp.pdf”, http://www.schott.com/hometech/english/download/thermal_exp.pdf.
- 26 B. Rau, I. Sieber, J. Schneider, M. Muske, M. Stöger-Pollach, P. Schattschneider, S. Gall, W. Fuhs, “Low-temperature Si epitaxy on large-grained polycrystalline seed layers by electron-cyclotron resonance chemical vapor deposition”, *Journal of Crystalline Growth*, **270**, 396-401 (2004).
- 27 C. W. Teplin, H. M. Branz, K. M. Jones, M. J. Romero, P. Stradins, S. Gall, “Hot-wire chemical vapor deposition epitaxy on polycrystalline silicon seeds on glass” *Proceedings of Materials Research Society*, **989**, A06-16 (2007).
- 28 G. Andrae, J. Bergmann, F. Falk, E. Ose, “Multicrystalline silicon thin film solar cells”, *Proceedings of 19th European Photovoltaic Solar Energy Conference*, Paris, France, 872-875 (2004).

- 29 A. G. Aberle, N. P. Harder, S. Oelting, "Formation of large-grained uniform poly-Si films on glass at low temperature", *Journal of Crystal Growth*, **226**, 209-214 (2001).
- 30 S. Gall, J. Schneider, J. Klein, K. Hubener, M. Muske, B. Rau, E. Conrad, I. Sieber, K. Petter, K. Lips, M. Stoger-Pollach, P. Schattschneider, W. Fuhs, "Large-grained polycrystalline silicon on glass for thin-film solar cells", *Thin Solid Films*, **511**, 7 (2006).
- 31 G. Ekanayake, T. Quinn, H.S. Reehal, B. Rau, S. Gall, "Large-grained polycrystalline silicon films on glass by epitaxial thickening of seed layers by aluminum induced crystallization", *Proceedings of 21st European Photovoltaic Solar Energy Conference*, Dresden, Germany, 945-948, (2006).
- 32 G. Andrae, J. Bergmann, A. Bochmann, F. Falk, E. Ose, S. Dauwe, T. Kieliba, "Characterization and simulation of multicrystalline LLC-Si thin film solar cells", *Proceedings of 20th European Photovoltaic Solar Energy Conference*, Barcelona, Spain, 1171-1174 (2005).
- 33 A. Straub, D. Inns, M.L. Terry, Y. Huang, P.I. Widenborg, A.G. Aberle, "Optimisation of low-temperature silicon epitaxy on seeded glass substrates by ion-assisted deposition", *Journal of Crystal Growth*, **280**, 385-400 (2005).
- 34 Y. Ota, "Silicon molecular beam epitaxy", *Thin Solid Films*, **106**, 3-136 (1983).
- 35 Y. Shiraki, "Silicon molecular beam epitaxy", *Progress in Crystal Growth and Characterization*, **12**, 45-66 (1986).
- 36 J. C. Bean, "Silicon molecular beam epitaxy.1984-1986", *Journal of Crystal Growth*, **81**, 411-420 (1987).
- 37 E. Kasper and F. Schaeffler, "Low temperature molecular beam epitaxy of silicon (Si-MBE)", *Physica Scripta*, **T29**, 147-151 (1989).
- 38 D. J. Eaglesham, "Semiconductor molecular-beam epitaxy at low temperatures", *Journal of Applied Physics*, **77**, 3597-3617 (1995).
- 39 C. T. Foxon, "Three decades of molecular beam epitaxy", *Journal of Crystal Growth*, **251**, 1-8 (2003).

- 40 H.-J. Gossmann, E. F. Schubert, D. J. Eaglesham, M. Cerullo, "Low-temperature Si molecular beam epitaxy: Solution to the doping problem", *Applied Physics Letters*, **57**, 2440-2442 (1990).
- 41 R. A. A. Kubiak, W. Y. Leong, E. H. C. Parker, "Potential enhanced Sb and As doping in Si molecular beam epitaxy", *Applied Physics Letters*, **46**, 565-567 (1985).
- 42 H. Jorke, H.-J. Herzog, H. Kibbel, "Secondary implantation of Sb into Si molecular beam epitaxy layers", *Applied Physics Letters*, **47**, 511-513 (1985).
- 43 T. Itoh, T. Nakamura, M. Muromachi, T. Sugiyama, "Antimony concentration in silicon epitaxial layer formed by partially ionized vapour deposition", *Japanese Journal of Applied Physics*, **15**, 1145-1146 (1976).
- 44 B. A. Unvala, "Epitaxial Growth of Silicon by Vacuum Evaporation", *Nature (London)*, **194**, 966-967 (1962).
- 45 B. A. Unvala, *Le Vide*, **104**, 109 (1963).
- 46 S. Oelting, D. Martini, and D. Bonnet, "Ion assisted deposition of Si films for solar cells", *Proceedings of 11th European Photovoltaic Solar Energy Conference*, Chur, Switzerland, 491-494 (1992).
- 47 S. Oelting, D. Martini, and D. Bonnet, "Crystalline thin film silicon solar cells by ion-assisted deposition", *Proceedings of 12th European Photovoltaic Solar Energy Conference*, Amsterdam, Netherlands, 1815-1818 (1994).
- 48 H. Sugiura, M. Yamaguchi, "Crystal defects of silicon films formed by molecular beam epitaxy", *Japanese Journal of Applied Physics*, **19**, 583-589 (1980).
- 49 J. Krinke, G. Kuchler, R. Brendel, H. Artman, W. Frey, S. Oelting, M. Schulz, H. P. Strunk, "Microstructure of epitaxial layers deposited on silicon by ion assisted deposition", *Solar Energy Materials and Solar Cells*, **65**, 503-508 (2001).
- 50 D. H. Neuhaus, N. P. Harder, S. Oelting, R. Bardos, A. B. Sproul, P. Widenborg, A. G. Aberle, "Dependence of the recombination in thin-film Si solar cells grown by ion-assisted deposition on the crystallographic orientation of the substrate", *Solar Energy Materials and Solar Cells*, **74**, 225-232 (2002).

- 51 T. A. Wagner, L. Oberbeck, R. B. Bergmann, J. H. Werner, "Intra-grain defects- Limiting factor for low temperature polycrystalline silicon films ?", *Solid State Phenomena*, **80-81**, 95-100, (2001).
- 52 T. Wagner, "Low temperature silicon epitaxy: Defects and electronic properties", PhD thesis, University of Stuttgart, Fakultät Informatik, Elektrotechnik und Informationstechnik, (2003).
- 53 B. Gorka, P. Dogan, I. Sieber, F. Fenske, S. Gall, "Low-temperature epitaxy of silicon by electron beam evaporation", *Thin Solid Films*, **515**, 7643–7646 (2007).
- 54 L. Oberbeck, "Ionen Assistierte Abscheidung von Siliciumschichten", PhD thesis, University of Stuttgart, Institut fuer Physikalische Elektronik, (2001).
- 55 N. P. Harder, T. Puzzer, P. I. Widenborg, S. Oelting, A. G. Aberle, "Ion-assisted low-temperature silicon epitaxy on randomly textured seed layers on glass", *Crystal Growth and Design*, **3**, 5, 767-771 (2003).
- 56 N. P. Harder, "Experimental and theoretical investigations into second- and third-generation photovoltaic devices", PhD thesis, University of Leipzig, Fakultät fuer Physik und Geowissenschaften, (2004).
- 57 B. Gorka, "Silizium-Niedertemperaturepitaxie mit Hilfe von ionassistierter Deposition", Diplomarbeit, University of Bielefeld, Fakultät fuer Physik, (2006).
- 58 L. Oberbeck, R. B. Bergmann, "Electronic properties of silicon epitaxial layers deposited by ion-assisted deposition at low temperatures", *Journal of Applied Physics*, **88**, 5, 3015-3021 (2000).
- 59 R. B. Bergmann, C. Zaczek, N. Jensen, "Low-temperature Si epitaxy with high deposition rate using ion-assisted deposition", *Applied Physics Letters*, **72**, 23, 2996-2998 (1998).
- 60 L. Oberbeck, R. B. Bergmann, N. Jensen, S. Oelting, J. H. Werner, "Low-temperature silicon epitaxy by ion-assisted deposition", *Solid State Phenom.*, **67-68**, 459 (1999).
- 61 A. Straub, N. P. Harder, Y. Huang, A. G. Aberle, "High-quality homo-epitaxial silicon growth in a non-ultra-high vacuum environment by ion-assisted deposition", *Journal of Crystal Growth*, **268**, 41-51 (2004).
- 62 A. Straub, D. Inns, M. L. Terry, Y. Huang, P. I. Widenborg, A. G. Aberle, "Optimization of low-temperature silicon epitaxy on seeded glass substrates

- by ion-assisted deposition”, *Journal of Crystal Growth*, **280**, 385-400 (2005).
- 63 A. Straub, “Polycrystalline Silicon Thin-Film Solar Cells on Glass by Ion-Assisted Deposition”, PhD thesis, University of New South Wales, Centre of Excellence for Advanced Silicon Photovoltaics and Photonics, (2005).
- 64 R. B. Bergmann, L. Oberbeck, T. A. Wagner, “High-quality and low-temperature epitaxial Si films deposited at very high deposition rate”, *Journal of Crystal Growth*, **225**, 335-339 (2001).
- 65 J. Schneider, “Nucleation and growth during the formation of polycrystalline silicon thin films”, PhD thesis, Technical University of Berlin, Fakultät IV- Elektrotechnik und Informatik, (2005).
- 66 J. Schneider, J. Klein, M. Muske, S. Gall, W. Fuhs, “Depletion regions in the aluminium-induced layer exchange process crystallizing amorphous Si”, *Applied Physics Letters*, **87**, 031905-1 (2005).
- 67 J. Schneider, J. Klein, A. Sarikov, M. Muske, S. Gall, W. Fuhs, “Suppression of nucleation during the aluminum-induced layer exchange process” *Materials Research Society Symposium Proceedings*, **862**, A2.2.1-A.2.2.6 (2005).
- 68 J. Schneider, A. Schneider, A. Sarikov, J. Klein, M. Muske, S. Gall, W. Fuhs, “Aluminum-induced crystallization: Nucleation and growth process”, *Journal of Non-Crystalline Solids*, **352**, 972-975 (2006).
- 69 W. Kern, and D. Puotinen, “Cleaning solutions based on hydrogen for use in silicon semiconductor technology”, *R.C.A. Review*, **31**, 2, 187-206 (1970).
- 70 O. Nast, T. Puzzer, L. M. Koschier, A. B. Sproul, S. R. Wenham, “Aluminum-induced crystallization of amorphous silicon on glass substrates above and below the eutectic temperature”, *Applied Physics Letters*, **73**, 3214-3216 (1998).
- 71 B. Gorka, B. Rau, K.Y. Lee, P. Dogan, F. Fenske, E. Conrad, S. Gall, B. Rech, “Hydrogen Passivation Of Polycrystalline Si Thin Films By Plasma Treatment”, *Proceedings of the 22nd European Photovoltaic Solar Energy Conference*, Milan, Italy 2024-2027 (2007).
- 72 B. Gorka, B. Rau, P. Dogan, C. Becker, F. Ruske, S. Gall, and B. Rech, “Influence of Hydrogen Plasma on the Defect Passivation of Polycrystalline Si Thin Film Solar Cells”, *Plasma Processes and Polymers*, **6**, S36 (2009).

- 73 B. Gorka “Hydrogen Passivation of Polycrystalline Si Thin Film Solar Cells”, PhD thesis, Technical University of Berlin, Faculty of Electrotechnik and Informatik (2010).
- 74 E. Conrad, L. Korte, K. v. Maydell, H. Angermann, C. Schubert, R. Stangl, M. Schmidt, “Development and Optimization of a-Si:H/c-Si heterojunction Solar Cells Completely Processed at Low Temperatures”, *Proceedings of the 21st European Photovoltaic Solar Energy Conference, Dresden, Germany*, 784-787 (2006).
- 75 F. Secco d’Argona, “Dislocation etch for (100) planes in Silicon”, *Journal of Electrochem. Society*, **119**, 948-951 (1972).
- 76 C. J. Wu, and D. B. Wittry, “Investigation of minority carrier diffusion lengths by electron bombardment of Schottky barriers”, *Journal of Applied Physics*, **49**, 2827-2836 (1978).
- 77 H. Richter, Z. P. Wang, and L. Ley, “The one phonon Raman Spectrum in microcrystalline Silicon” *Solid State Communications*, **39**, 5, 625-629 (1981).
- 78 L. J. van der Pauw, “A method of measuring specific resistivity and Hall effect of discs of arbitrary shape”, *Philips Research Reports*, **13**, 1-9 (1958).
- 79 P. Ozdag, “Capacitance-Voltage Spectroscopy in Metal-Ta₂O₅-Si MOS Capacitors”, Master of Science Thesis, Izmir Institute of Technology, Department of Physics (2005).
- 80 M. Green, “Solar Cells: Operating Principles, Technology, and System Applications”, Longman Higher Education, ISBN: 978-0138222703 (1981).
- 81 G. J. Pietsch, “Hydrogen on si: ubiquitous surface termination after wet-chemical processing”, *Applied Physics A: Materials Science and Processing*, **60**, 4, 347-363 (1995).
- 82 H. Craig Casey, “Devices for Integrated Circuits- Silicon and III-V Compound Semiconductors” John Wiley and Sons, Inc. ISBN 0-471-17134-4, 74 (1999).
- 83 K.Y. Lee, M. Muske, I. Gordon, M. Berginski, J. D’Haen, J. Hüpkes, S. Gall, B. Rech, “Large-grained Poly-Si Films on ZnO:Al Coated Glass Substrates”, *Thin Solid Films*, **516**, 6869-6872 (2008).
- 84 K.Y. Lee, C. Becker, M. Muske, S. Gall, B. Rech, I. Gordon, J. D’Haen, M. Berginski, J. Hüpkes, “Poly-Si films grown on ZnO:Al coated glass by

- aluminum-induced layer exchange process”, *Proceedings of 22nd European Photovoltaic Solar Energy Conference*, Milan, Italy, 2028-2031 (2007).
- 85 I. Gordon, D. Van Gestel, L. Carnel, G. Beaucarne, J. Porrtmans, K.Y. Lee, P. Dogan, B. Gorka, C. Becker, F. Fenske, B. Rau, S. Gall, B. Rech, J. Plentz, F. Falk, D. Le Bellac, “Advanced Concepts for Thin-Film Polycrystalline-Silicon Solar Cells”, *Proceedings of 22nd European Photovoltaic Solar Energy Conference*, Milan, Italy, 1890-1894 (2007).
- 86 S. Gall, J. Schneider, J. Klein, K. Huebener, M. Muske, B. Rau, E. Conrad, I. Sieber, K. Petter, K. Lips, M. Stoeger-Pollach, P. Schattschneider, W. Fuhs, “Large-grained polycrystalline silicon on glass for thin-film solar cells”, *Thin Solid Films* **511-512**, 7-14 (2006).
- 87 J.Y.W. Seto, “The electrical properties of polycrystalline silicon films”, *Journal of Applied Physics*, **46**, 5247-5254 (1975).
- 88 P. Dogan, B. Gorka, L. Scheller, I. Sieber, F. Fenske, S. Gall, “Low-temperature epitaxy of silicon by using electron beam evaporation”, *Proceedings of the 21st European Photovoltaic Solar Energy Conference*, Dresden, Germany, 1060-1063 (2006).
- 89 G. Andrae, A. Bochmann, F. Falk, A. Gawlik, E. Ose, J. Plentz, “Diode Laser Crystallized Multicrystalline Silicon Thin Film Solar Cells on Glass”, *Proceedings of the 21st European Photovoltaic Solar Energy Conference*, Dresden, Germany, 972-975 (2006).
- 90 C. Becker, P. Dogan, B. Gorka, F. Ruske, T. Haenel, J. Behrends, F. Fenske, K. Lips, S. Gall, B. Rech, “Polycrystalline Silicon Thin-film Solar Cells on ZnO:Al Coated Glass”, *Materials Research Society Symposium Proceedings*, **1066**, A06.01 (2008).
- 91 C. Becker, P. Dogan, F. Ruske, B. Gorka, A. Sánchez-Vicens, E. Conrad, S. Gall and B. Rech, “Solid Phase Crystallized Silicon Thin-Film Solar Cells on Temperature-Stable ZnO:Al Contact Layers”, *Proceedings of the 23rd European Photovoltaic Solar Energy Conference*, Valencia, Spain 2045-2048 (2008).
- 92 L. Oberbeck, J. Schmidt, T. A. Wagner, R. B. Bergmann, “High-rate Deposition of Epitaxial Layers for Efficient Low-temperature Thin Film Epitaxial Solar Cells”, *Progress in Photovoltaics: Research and Applications*, **9**, 333-340 (2001).

- 93 R. B. Bergmann, L. Oberbeck, T. A. Wagner, "High-quality and Low-temperature Epitaxial Si Films Deposited at Very High Deposition Rate", *Journal of Crystal Growth*, **225**, 335-339 (2001).
- 94 G. Andrae, J. Plentz, A. Gawlik, E. Ose, F. Falk, K. Lauer, "Advances in Multicrystalline LLC-Si Thin Film Solar Cells", *Proceedings of the 22nd European Photovoltaic Solar Energy Conference*, Milan, Italy 1967-1970 (2007).
- 95 R. J. Egan, P. A. Basore, R. Evans, "Silicon Deposition Optimization for Manufacturability of CSG Modules", *Proceedings of the 22nd European Photovoltaic Solar Energy Conference*, Milan, Italy, 1895-1897 (2007).
- 96 T. Sontheimer, P. Dogan, C. Becker, S. Gall, B. Rech, U. Schubert, T. Young, S. Partlin, M. Keevers, R.J. Egan, "6.7% Efficient Poly-Si Thin Film Mini-Modules by High-Rate Electron-Beam Evaporation", *Proceedings of the 24th European Photovoltaic Solar Energy Conference*, Hamburg, Germany 2478-2481 (2009).
- 97 R. Egan, M. Keevers, U. Schubert, T. Young, R. Evans, S. Partlin, M. Wolf, J. Schneider, D. Hogg, B. Eggleston, M. Green, F. Falk, A. Gawlik, G. Andrä, M. Werner, C. Hagendorf, P. Dogan, T. Sontheimer, S. Gall, "CSG Minimodules Using Electron-Beam Evaporated Silicon", *Proceedings of the 24th European Photovoltaic Solar Energy Conference*, Hamburg, Germany 2279-2285 (2009).
- 98 S. Gall, C. Becker, E. Conrad, P. Dogan, F. Fenske, B. Gorka, K.Y. Lee, B. Rau, F. Ruske, B. Rech, "Polycrystalline silicon thin-film solar cells on glass", *Solar Energy Materials and Solar Cells*, **93**, 1004 (2009).
- 99 K. Y. Lee, C. Becker, M. Muske, F. Ruske, S. Gall, B. Rech, "Temperature stability of ZnO:Al film properties for poly-Si thin film devices", *Applied Physics Letters*, **91**, 241911 (2007).
- 100 M. J. Keevers, A. Turner, U. Schubert, P. A. Basore, M. A. Green, "Remarkable effective hydrogenation of crystalline silicon on glass modules", *Proceedings of the 20th European Photovoltaic Solar Energy Conference*, Barcelona, Spain 1305-1308 (2005).
- 101 R. B. Bergmann, J. H. Werner, "The future of crystalline silicon films on foreign substrates", *Thin Solid Films*, **403-404**, 162-169 (2002).

- 102 T. Baba et al., "9.2% efficiency thin-film polycrystalline Si solar cell by a novel solid phase crystallization method", *Proceedings of 13th European Photovoltaic Solar Energy Conference*, 1708 (1995).
- 103 K. Yamamoto et al., "Below 5 μm thin film poly-Si solar cell on glass substrate fabricated at low temperature", *Proceedings of 2nd World Conference on Photovoltaic Energy Conversion*, 1284 (1998).
- 104 A. Aberle et al., "Recent advances in polycrystalline silicon thin-film solar cells on glass at UNSW", *Proceedings of 31st IEEE Photovoltaic Specialists Conference*, 877 – 882 (2005).
- 105 J. Zhao, A. Wang, M. A. Green, "24.5 % efficiency PERL silicon solar cells on SEH MCZ substrates and cell performance on other SEH CZ and FZ substrates", *Solar Energy Materials and Solar Cells*, **66**, 27-36 (2001).

List of Author Publications

- T. Sontheimer, P. Dogan, C. Becker, S. Gall, B. Rech, U. Schubert, T. Young, S. Partlin, M. Keevers, R.J. Egan, “**6.7% Efficient Poly-Si Thin Film Mini-Modules by High-Rate Electron-Beam Evaporation**”, *Proceedings of the 24th European Photovoltaic Solar Energy Conference*, Hamburg, Germany 2478-2481 (2009).
- R. Egan, M. Keevers, U. Schubert, T. Young, R. Evans, S. Partlin, M. Wolf, J. Schneider, D. Hogg, B. Eggleston, M. Green, F. Falk, A. Gawlik, G. Andrä, M. Werner, C. Hagendorf, P. Dogan, T. Sontheimer, S. Gall, “**CSG Minimodules Using Electron-Beam Evaporated Silicon**”, *Proceedings of the 24th European Photovoltaic Solar Energy Conference*, Hamburg, Germany 2279-2285 (2009).
- B. Gorka, B. Rau, P. Dogan, C. Becker, F. Ruske, S. Gall, and B. Rech, “**Influence of hydrogen plasma on the defect passivation of polycrystalline Si thin film solar cells**”, *Plasma Processes and Polymers*, **6**, S36 (2009).
- D. Van Gestel, P. Dogan, I. Gordon, H. Bender, K. Y. Lee, G. Beaucarne, S. Gall, and J. Poortmans, “**Investigation of intragrain defects in pc-Si layers obtained by aluminum-induced crystallization: comparison of layers made by low and high temperature epitaxy**”, *Materials Science and Engineering B-Advanced Functional Solid-State Materials*, **159-60**, 134 (2009).
- B. Rau, T. Weber, B. Gorka, P. Dogan, F. Fenske, K.Y. Lee, S. Gall, B. Rech, “**Development of a rapid thermal annealing process for polycrystalline silicon thin-film solar cells on glass**”, *Materials Science and Engineering B-Advanced Functional Solid-State Materials*, **159-60**, 329 (2009).
- C. Becker, E. Conrad, P. Dogan, F. Fenske, B. Gorka, T. Hänel, K. Y. Lee, B. Rau, F. Ruske, T. Weber, M. Berginski, J. Hüpkes, S. Gall and B. Rech, “**Solid phase crystallization of amorphous silicon on ZnO:Al for thin film solar cells**”, *Solar Energy Materials and Solar Cells*, **93**, 855 (2009).

- S. Gall, C. Becker, E. Conrad, P. Dogan, F. Fenske, B. Gorka, K.Y. Lee, B. Rau, F. Ruske, B. Rech, “**Polycrystalline silicon thin-film solar cells on glass**”, *Solar Energy Materials and Solar Cells*, **93**, 1004 (2009).
- P. Dogan, E. Rudigier, F. Fenske, K.Y. Lee, B. Gorka, B. Rau, E. Conrad, S. Gall, “**Structural and electrical properties of epitaxial Si layers prepared by E-beam evaporation**”, *Thin Solid Films*, **516**, 6989 (2008).
- C. Becker, P. Dogan, B. Gorka, F. Ruske, T. Haenel, J. Behrends, F. Fenske, K. Lips, S. Gall, B. Rech, “**Polycrystalline silicon thin-film solar cells on ZnO:Al coated glass**”, *Materials Research Society Symposium Proceedings*, **1066**, A06.01 (2008).
- P. Dogan, F. Fenske, K.Y. Lee, B. Gorka, S. Gall, B. Rech, “**Low Temperature Epitaxy of Si by E-Beam Evaporation for Polycrystalline Si Thin Film Solar Cells**”, *Abstract book of NANOMAT 2008*, METU, Ankara, Turkey, 25 (2008).
- C. Becker, P. Dogan, F. Ruske, B. Gorka, A. Sánchez-Vicens, E. Conrad, S. Gall and B. Rech, “**Solid phase crystallized silicon thin-film solar cells on temperature-stable ZnO:Al contact layers**”, *Proceedings of the 23rd European Photovoltaic Solar Energy Conference*, Valencia, Spain, 2045-2048 (2008).
- K. Y. Lee, P. Dogan, F. Ruske, B. Gorka, S. Gall, and B. Rech, “**The properties of Poly-Si films grown on ZnO:Al coated borofloat glass by aluminum-induced layer exchange (ALILE) process**”, *Proceedings of the 23rd European Photovoltaic Solar Energy Conference*, Valencia, Spain, 2261-2264 (2008).
- B. Gorka, P. Dogan, I. Sieber, F. Fenske, S. Gall, “**Low-temperature epitaxy of silicon by electron beam evaporation**”, *Thin Solid Films*, **515**, 7643–7646 (2007).
- P. Dogan, F. Fenske, L.-P. Scheller, K. Y. Lee, B. Gorka, B. Rau, E. Conrad, S. Gall, B. Rech, “**Structural and electrical properties of epitaxial Si layers**

prepared by E-beam evaporation”, *Proceedings of the 22nd European Photovoltaic Solar Energy Conference*, Milan, Italy, 2019-2023 (2007).

- S. Gall, K.Y. Lee, P. Dogan, B. Gorka, C. Becker, F. Fenske, B. Rau, E. Conrad, B. Rech, “**Large-grained polycrystalline silicon thin-film solar cells on glass**”, *Proceedings of the 22nd European Photovoltaic Solar Energy Conference*, Milan, Italy, 2005-2009 (2007).
- B. Rau, K.Y. Lee, P. Dogan, F. Fenske, E. Conrad, S. Gall, “**Improvement of epitaxially grown poly-Si thin-film solar cells on glass by rapid thermal annealing**”, *Proceedings of the 22nd European Photovoltaic Solar Energy Conference*, Milan, Italy, 2010-2014 (2007).
- B. Gorka, B. Rau, K.Y. Lee, P. Dogan, F. Fenske, E. Conrad, S. Gall, B. Rech, “**Hydrogen passivation of polycrystalline si thin films by plasma treatment**” *Proceedings of the 22nd European Photovoltaic Solar Energy Conference*, Milan, Italy, 2024-2027 (2007).
- I. Gordon, D. Van Gestel, L. Carnel, G. Beaucarne, J. Poortmans, K.Y. Lee, P. Dogan, B. Gorka, C. Becker, F. Fenske, B. Rau, S. Gall, B. Rech, J. Plentz, F. Falk, D. Le Bellac, “**Advanced concepts for thin-film polycrystalline-silicon solar cells**”, *Proceedings of the 22nd European Photovoltaic Solar Energy Conference*, Milan, Italy, 1890-1894 (2007).
- P. Dogan, B. Gorka, L. Scheller, I. Sieber, F. Fenske, S. Gall, “**Low-temperature epitaxy of silicon by using electron beam evaporation**”, *Proceedings of the 21st European Photovoltaic Solar Energy Conference*, Dresden, Germany, 1060-1063 (2006).
- S. Gall, J. Berghold, E. Conrad, P. Dogan, F. Fenske, B. Gorka, K. Lips, M. Muske, K. Petter, B. Rau, J. Schneider, I. Sieber, “**Large-grained polycrystalline silicon on glass for thin-film solar cells**”, *Proceedings of the 21st European Photovoltaic Solar Energy Conference*, Dresden, Germany, 1091-1094 (2006).

List of Author Presentations

- “Low-Temperature Epitaxy of Silicon by E-Beam Evaporation for Polycrystalline Silicon Thin Film Solar Cells”, International Workshop on Advanced Materials and Devices for Photovoltaic Applications, METU, 24-28 April 2008, Ankara, Turkey (Oral).
- “Structural and Electrical Properties of Epitaxial Si Layers Prepared by E-beam Evaporation”, European Materials Research Symposium 2007-Spring Meeting, 28 May-01 June 2007, Strasbourg, France (Oral).
- “Structural and Electrical Properties of Epitaxial Si Layers Prepared by E-beam Evaporation”, HZB Department Seminar, Silicon Photovoltaics (SE1), 12 July 2007, Berlin, Germany (Oral).
- “Structural and electrical properties of epitaxial Si layers prepared by E-beam evaporation”, 22nd European Photovoltaic Solar Energy Conference, 2007, Milan, Italy, (Poster).
- “Low-temperature epitaxy of silicon by using electron beam evaporation”, 21st European Photovoltaic Solar Energy Conference, 2006, Dresden, Germany (Poster).

List of Author Patents

- F. Fenske, P. Dogan, S. Gall, B. Rech, “ **Influence of nitrogen for the improvement of thin-film solar cells**”, *German Patent (HZB 0910)*, (2009).

Selbständigkeitserklärung

Ich erkläre, dass ich die vorliegende Arbeit selbständig und nur unter Verwendung der angegebenen Literatur und Hilfsmittel angefertigt habe.

Berlin, den 23.12.2011

Pinar Dogan